Investigation into Melt Overflow of Alloys

Thesis

Investigations into Melt Overflow of Alloys

Thesis submitted by

Ali Kalkanli

for the degree of

Doctor of Philosophy

December 1991

Materials Department
Faculty of Technology
The Open University
Milton Keynes
England

Date of submission: 6 December 1991
Date of award: 27 February 1992

ProQuest LLC.
789 East Eisenhower Parkway
P.O. Box 1346
Ann Arbor, MI 48106 – 1346

Abstract

The possibility of direct strip casting onto a single rotary chiller has been investigated. A number of alloys including Fe-Cr-Ni, Fe-Ni and Fe-Cr-Al were tested and strips were produced. Strip formation has been modelled theoretically studying two basic consideration: a) Liquid film formation prior to recalescence due to momentum transfer. b) Strip formation in a melt puddle by one dimensional heat transfer across the wheel/strip interface. Experimental modelling of the melt overflow process has been undertaken, to: a) investigate casting instabilities and associated limitations of direct strip casting and, b) reveal the effects of process parameters such as surface tension, viscosity and liquid metal depth on the final characteristics of the strip.

The melt overflow process has been employed for the production of strips, ribbons and fibres with thicknesses ranging between 150-700 μm. A special crucible(2.5 kg capacity) and plunger mechanism was designed and developed for producing up to 30 mm wide directly cast strip from a mini induction furnace. The most efficient pouring channel geometry was determined to minimize the heat losses within the channel and maintain sufficient hot liquid metal flow steadily during the melt overflow. The test material was based on 304 stainless Steel. The critical casting speeds and alloy compositions necessary to produce uniform strips without serrations were determined. Surface tension was modified by the addition of deoxidizing agents and sulphur. Surface tension values were measured by a modified oscillation droplet technique. The lowest value of surface tension in stainless steel was found to be 1.43 N.m^{-1} at a casting temperature of 1600 °C for sulphur at per cent 0.073. This alloy yielded strip with edge serrations and poor strip quality in contrast to an alloy with a surface tension of 1.98 N.m^{-1} at a casting temperature of 1580 °C with sulphur content 0.023. Uniform strips were obtained for this case.

The capillary number which is a ratio of viscous forces to surface tension forces in a liquid film were calculated for 304 stainless steel strips as 0.006-0.009 for corresponding thickness values 175-190 μm. High speed photography, video and specialised photographic techniques were utilised to examine

Kelvin-Helmholtz instability and the temperature distribution during the residence time of the strip on the wheel.

As cast strip microstructures were found to consist of dendritic and cellular solidification structures consistent with a cooling rate of 10^4 K.s^{-1}.

Acknowledgements

I would like to express my sincere gratitude to Prof J.V.Wood and Dr.N.St.Braithwaite, for their valuable guidance, unending and constant encouragement throughout the course of this thesis.

Special thanks are due to Ken Boulby for arranging financial support and to Andy Horlock for providing materials and technical support through Fibre Technology.

The author wishes to acknowledge the help provided, in various aspects, by the staff of the Materials Discipline of The Open University. I am grateful to Colin Gagg for his interest, encouragement and technical help with the experiments,to Dr David Grant for surface tension measurements and technical support, to Naomi Williams for her help with electron microscopy, to Richard Black for colour photography, to Ian Norman for computer aided sketches and to Gordon Imlach for the preparation of materials.

I am forever indebted to my wife, family and colleagues for the help and encouragements that I have received. I would particulary like to thank Keith and Naomi Williams for their friendly attitude and specially Tamer Ozdemir for valuable discussions and help, Monday Igharo, Yu Chen and Guy Hitchcock for being such generous friends.

Contents

List of Figures

List of Tables

Chapter 1

Introduction

In recent years, the direct casting of thin strip or slabs has received much attention. The benefits of direct continuous casting nearer to final thickness include savings in labour, energy and capital investment with increased yield, Nauman and Love(1987). Also, the rapid solidification of a thin section and the elimination of hot rolling, may lead to significant improvements in quality and allow the development of new alloys and phases. The design and operation of the casting machine and the shape and structural control of the products are essentially interrelated. This thesis is concerned with one type of casting technique 'Melt overflow'. In this method the melt is displaced from a furnace or tundish over a lip onto a rotating wheel. This process which is a single roller, melt casting technique was originally developed for making very fine filament, and it was observed that at slow wheel speeds and high melt delivery rates that strip could be produced, (Gaspar, Hackman, Sahai, Clark and Wood(1986)). The process is of interest since it has the potential for producing tonnage quantities of strip in a wide range of alloys, (Figure 1.1).

In the melt overflow technique, the melt is not constrained as it is in the case with the alternative orifice methods such as planar flow casting and 'melt drag', Maringer(1988). Although they are very good for alloys with melting points up to 1500°C. These techniques do not readily lend themselves to the production of large tonnages of high melting point alloy strip since it is difficult to overcome the problem of erosion of the orifice and to

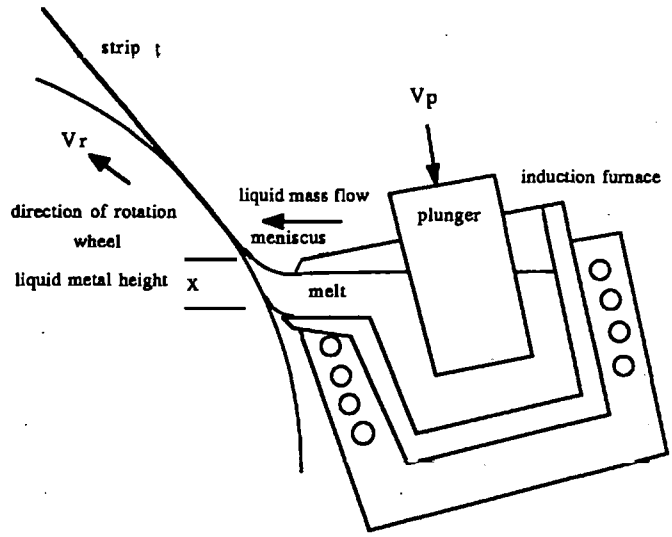

Figure 1.1 Schematic presentation of melt overflow process

prevent blockages as a result of slag or inclusion entrapment. Double roller casting techniques can be adopted for large scale production. Miyazawa and Szekely(1981). For virtually continuous production, displacement of the melt can be achieved either by continuously adding fresh melt or by using an inert plunger. Both approaches have industrial interest and the largest plant has a capacity of 1.5 tonnes. A small pilot plant was developed for Ti strip casting by Ribbon Technology Corporation Ohio, USA which employs a similar melt displacement technique under inert atmosphere, Brasmer(1979). The strip casting technique developed by the Ribbon Technology Corporation consists of a copper hearth, (i.e a cylindrical bowl machined from a solid block of copper) with an angled pouring lip also machined into the solid block. Alloys are melted using a plasma torch. The torch is centered over the hearth and made to traverse across the top surface of the melt. Once the metal is melted, the hearth is tipped toward an adjacent, wheel, allowing the metal to come into contact with the rotating surface, where it quickly solidifies into a thin continuous strip.

By contrast, the conventional melt overflow process developed and undertaken in this work consists of an induction furnace with a spout and lip in the side of a furnace. An inert, alumina brick plunger is used to displace the melt in this method. The strip casting process developed and performed is shown in Figure 1.2.

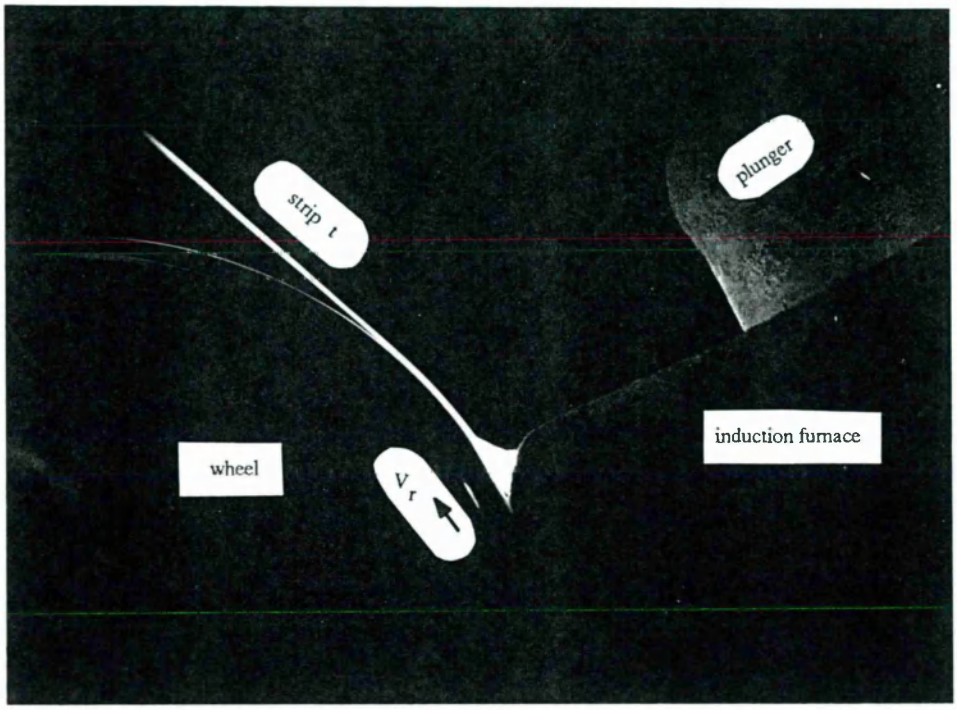

Figure 1.2 The strip casting of 304 stainless steel by melt overflow studied and performed in this thesis

Since fluid flow is not constrained in the melt overflow process, the stabilization of pool oscillations is a critical aspect which is governed by the alloy properties such as the temperature dependent surface tension and viscosity of the melt, and also by process variables such as the plunger velocity (casting rate) and wheel speed.

1.1 Research Strategy and Objectives of the presented study

Since the melt overflow of the commercial alloys investigated is impossible to perform for high alloy surface tension and viscosity values, the primary objective was to verify the strip casting process, to understand the strip formation and limitations of the process. The study was carried out in the order of steps due to the following reasons:

1) Liquid metal delivery in a horizontal pouring channel is difficult, even impossible if the heating efficiency of the induction furnace is low and heat losses through channel refractory are high. There is a requirement of storing heat in pouring channel to keep liquid metal at superheated state. Since a refractory plunger has to be used to displace the charge, possibility of overheating of liquid between plunger and furnace lining arises because of high heat losses through refractory of pouring channel compared to heat losses through furnace lining. As high superheat in the furnace should be maintained to transfer sufficient heat to the metal in pouring channel refractory erosion is a consequent problem. Therefore a strong refractory with a good thermal shock resistance should be chosen.

2) There is a temperature difference between furnace and pouring channel because liquid metal loses heat in pouring channel. This is related to the free surface area of the flow in the channel. Therefore channel geometry and dimensions govern the heat losses. Channel length and free surface area of flow should be kept as minimum to reduce the amount of heat losses.

3) The process can not be performed unless the temperature in the lip is above the alloy liquidus. The surface tension of liquid front which is a function of both surface active element concentration on the surface of flow and temperature should be reduced to a lower value. Unless this requirement is satisfied liquid metal flow can not be terminated on the rotary chiller as thin strip. The alloy surface tension has to be lowered by adding surface active elements to the melt. It is essential to create a stable uniform meniscus by the lip on the rotary chiller to produce uniform strip. So alloy design

and strip casting operation experience is required.

4) The melt overflow strip casting process does not always yield uniform strips if the critical casting conditions haven't been met. At some cases the casting may lead to serrated edge strips due to melt instabilities formed in the meniscus.

5) The temperature distribution and strip formation mechanism have to be studied. Strip formation is controlled by both momentum and heat transfer, but the proportion of these is not clearly revealed for melt overflow.

In order to perform the strip casting processing and modelling the strip formation the following strategy of research was adopted;

1) Horizontal pouring channel geometry was determined after a series of preliminary experiments. The volume to surface area ratio of pouring channel was determined as maximum possible value.

2) Sillimanite refractory was chosen as crucible material for its good thermal shock resistance. This crucible was fitted in a clay bonded graphite crucible. A phosphate bonded alumina patching material was used for backing material between sillimanite and graphite crucibles. The benefit of using a clay bonded graphite crucible originates from its division ability of magnetic field strength in the furnace. This also helps to store heat uniformly and gradually in furnace without leading to overheating of the furnace charge.

3) The alloy chosen for modelling purposes was 304 stainless steel because of its high temperature coefficient of surface tension. So the effect of increasing or decreasing surface tension on the process and strip characteristics could have been investigated.

4) The strip formation on the chiller was photographed from both side and top to reveal the effect of alloy properties on meniscus and subsequent strip dimensions. Temperature calibrated colour photography was employed to determine free surface temperature distribution. Heat transfer coefficient and cooling rate prediction were carried out to understand solidification characteristics.

Initially, the transferred wheel momentum has to be sufficient to overcome the overflowing stream. Instability which arises from the liquid pool

oscillations can be washed away by using enough stream velocity over the lip. For each different alloy composition a different critical stream velocity is necessary. In the present work temperature dependent surface tension was reduced by designing and manufacturing a special spout crucible in an induction furnace. Since there is a conflict between good thermal shock resistance and low heat loss over the spout of the furnace, a compromise was sought.

Chapter 2

Modelling of The Melt Overflow Process

2.1 Introduction

The modelling of casting processes can be undertaken theoretically or by means of a scaled experiment. A theoretical approach is concerned with physical parameters such as temperature dependent viscosity, surface tension and thermal diffusivity. An experimentally based model for direct strip casting of a specific alloy system, will vary basic parameters such as wheel speed, casting rate, contact angle and surface tension. In this chapter, the fundamental physical and empirical parameters are described. The aim is to reveal the important process and material parameters which have a direct effect on the final strip thickness and edge quality. Experimental data is analysed in the following chapters using the assumptions and formulations of this chapter.

2.2 Melt Overflow Process Parameters

Strip formation has been studied by continuous casting processes such as chill-block melt spinning, Lieberman(1976), melt drag, Narasimhan(1979), planar flow casting, King(1970), Twin-roll casting, Miyazava(1981) and melt overflow, Maringer(1988). The two major operating parameters that control the final cross-sectional dimensions of the ribbon, (thickness t and width w), are the volumetric flow rate Q and the wheel speed V_R.

The overall mass balance gives $Q = t.w.V_R$. The melt puddle spreads to a size such that t.w satisfies this balance: w equals the pool width while the thickness, t, is related to the puddle length or residence distance of liquid pool on the wheel(l). The residence time of liquid on the wheel can be defined as θ=l/V_R, Davies(1985). In melt overflow the residence distance of strip on the wheel is not equal to l. Strip stays on the wheel after it reaches the limiting thickness $d_{res} \geq l$. In melt spinning, the round section liquid jet is free and the puddle spreads laterally as well as in the direction of casting. Thus situation occurs in the melt overflow process as long as the eliptic stream cross section is kept constant. Since the flow is not constrained on the upper surface the spreading of the puddle is controlled only by the surface tension of the liquid stream. For planar flow casting and melt drag processes, a small nozzle/wheel gap which is about 0.1-0.4 mm, prevents significant lateral spread and w is equal or similar to the slot length whereas it is equal to the lip width in melt overflow. The lip/wheel gap in the melt overflow process is not more than 0.15 mm and this gap is such a critical dimension that liquid metal generally fails to be entrained by the wheel at gap distances bigger than 0.15 mm. The importance of gap distance, particularly the initiation of instabilities within the melt pool will be presented in chapter 3. Uniform strips are obtained when the melt puddle which forms on top the moving is stable. It has been suggested that such a stable melt puddle also maximizes the quenching rate, Kavesh(1978) and Anthony(1978).

2.3 Momentum Transfer in Melt Overflow

2.3.1 Lifting force created by rotating wheel in a liquid pool

The unconstrained open channel flow, terminated by contact with the surface of the rotating wheel where it is forced upward, can be analysed considering a balance of viscous and buoyancy forces(Gaspar, Sahai and Hackman(1986)). This can be seen in Figure 2.1. In this section the area shaded on the figure is going to be analyzed.

The liquid metal is dragged up to a height, H, and the affected distance

from the roll is b. The force acting on this liquid is in an upward direction by a vortex coupling mechanisms, F_a can be written as

$$F_a = Hw\mu\frac{dV}{dx} \tag{2.1}$$

where w is the width of stream, μ is the viscosity of liquid alloy and $\frac{dV}{dx}$ is the velocity gradient in the stream at any position of x which is the coordinate perpendicular to the wheel surface. In equation 2.1 the velocity gradient can be approximated by $\frac{V_R - V_{liq}}{b}$ where V_R is wheel speed and V_{liq} is the stream velocity. Assuming this cross section is eliptical and therefore the area can be written as $A_e = \frac{xw\pi}{4}$, where x is the true liquid metal depth in the lip. So equation 2.1 may be simplified to

$$F_a = Hw\mu\frac{V_R - V_{liq}}{b} \tag{2.2}$$

In the steady state, this force will be balanced by the weight of the liquid metal which in a linear approximation is

$$F_g = \frac{Hbwg\rho}{2} \tag{2.3}$$

where ρ is the density of the metal and g is acceleration due to gravity. Equating equations 2.2 and 2.3 yields b as

$$b = \sqrt{\left(\frac{2\mu\left(V_R - V_{liq}\right)}{g\rho}\right)} \tag{2.4}$$

The extent of the lip region affected by the presence of the spinning wheel is very small and it is supposed that H is nearly equal to b so that equation 2.4 results in

$$H = \sqrt{\left(\frac{2\mu\left(V_R - V_{liq}\right)}{g\rho}\right)} \tag{2.5}$$

Equation 2.5 can be used to calculate the increase of metal depth H at the "lip" for any casting speed V_R,(Gaspar, Sahai and Hackman(1986)). Values for increased melt depth H can then added to the depth of liquid at the casting lip to estimate the contact time of the liquid metal against the wheel. The true liquid metal depth $x = x_{lip} + H$. Where x_{lip} is the liquid metal depth measured near the edge of the lip. Moreover, an estimate of

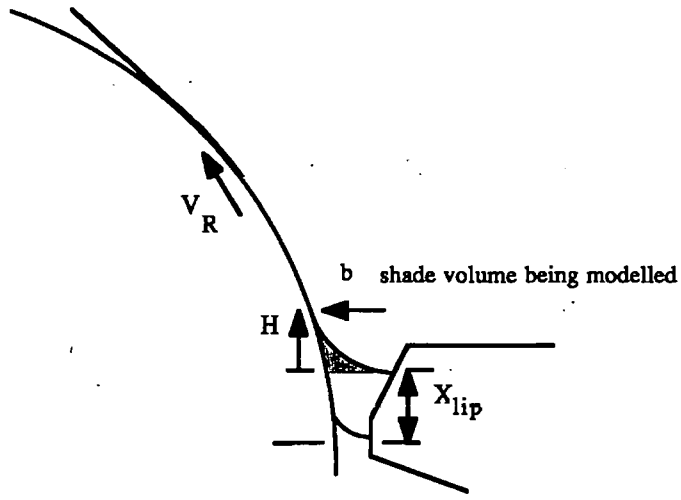

Figure 2.1 The geometry of dragged out liquid metal by a rotary chiller used in melt overflow

the stream velocity in the lip, V_{liq} can be made by equating solid mass flow as strip with liquid mass flow to the wheel:

$$Q = V_R \mu = V_{liq} A_e \rho \tag{2.6}$$

where μ is mass/unit length of strip and A_e is the eliptic cross section area of mass flow in the lip.

2.3.2 Liquid Film Flow at Small Capillary Number

In general, flow in films at small capillary numbers is strongly two dimensional and simple relationships between the parameters of the flow field are not readily obtainable. However, Landau and Levich(1942) have derived a simple relationship for film formation at small capillary numbers. The liquid metal flowing onto a rotating cooled wheel is assumed to have reached a steady-state and the system is defined to be effectively the same as that by a solid withdrawing from a liquid pool, (Landau and Levich(1942)). The

coordinate system in film developing is shown in Figure 2.2. The thickness of the liquid film remaining on the surface of the solid body depends on withdrawal rate, viscous stresses developed in the film and capillary forces. If the curvature of the solid surface is sufficiently small compared to the thickness of the film remaining on the surface, the body can be can be considered as an infinite plane and the film as a closely adhering parallel liquid layer. The analysis by Landau and Levich(1942) of the withdrawal of a plate vertically upwards is limited to a constant velocity V_R. Figure 2.2 defines the axes for the analysis. The y axis is in a direction perpendicular to the plate and the x axis along the plate. The surface is horizontal at large y. In

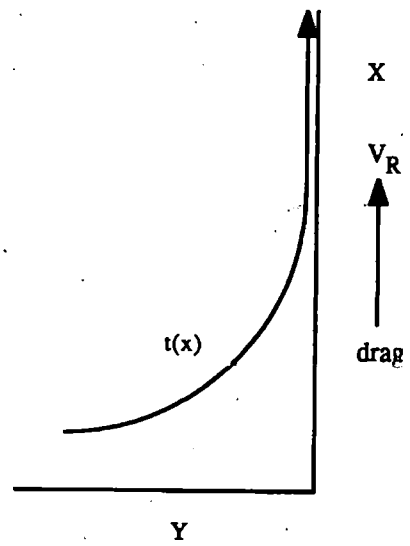

Figure 2.2 The coordinate system in film developing out of meniscus at a vertical plate

the vicinity of the moving plate the liquid is entrained and set into motion. The motion of this film is caused by the following :

1) transfer of momentum from the plate to the viscous liquid (the liquid particles on the surface of the plate are fully entrained by the latter) :

2) the effect of gravity, which causes the liquid to flow down the plate.

In addition, capillary pressure acts at the surface of the liquid, producing a meniscus near the plate. It is evident that the thickness t of the liquid layer that remains on the plate must be a function of the velocity of withdrawal V_R, of the liquid viscosity μ, of the product ρg and of the surface tension of the liquid σ. It varies with the height along the plate, and t=t(x). At a sufficient height above the liquid surface, the thickness of the entrained film is small and the motion of the liquid is almost rectilinear. On the other hand, far from the plate, the shape of the meniscus remains virtually undistorted by the motion of the plate. Thus, the liquid surface may be subdivided into two regions, one in which the liquid is directly entrained by the motion of the plate, and another region where the meniscus is static. The liquid in the first region moves almost parallel to the surface of the plate. In the second region, the liquid is assumed quiescent. A separate solution of the hydrodynamic equations can be obtained for each region and then a smooth matching of the two solutions. The equation derived by Levich(1942) for the shape of a liquid surface with a static meniscus can be written for a plate as;

$$\frac{\frac{d^2t}{dx^2}}{\left[1+\left(\frac{dt}{dx}\right)^2\right]^{\frac{3}{2}}} = \frac{\rho g x}{\sigma} \tag{2.7}$$

The integral form of equation 2.7 that satisfies the condition requiring the liquid surface far from the plate to be a horizontal surface is

$$\frac{\frac{dt}{dx}}{\left[1+\left(\frac{dt}{dx}\right)^2\right]^{\frac{1}{2}}} = \frac{\rho g x^2}{2\sigma} - 1 \tag{2.8}$$

For a moving plate equation 2.8 is valid only far from the plate, where the thickness of the liquid layer is large and its height x is small.

At large x and small t, entrainment of the liquid cannot be disregarded. A low value of the film thickness in equation 2.8 corresponds to a transition from the static to entrainment region. In this case, the liquid film is almost vertical and parallel to the plane (y=0). When the derivative $\frac{dt}{dx} = 0$, the film is in a vertical position. Therefore, the transition to the entrainment region occurs as $\frac{dt}{dx}$ approaches zero. Equation 2.8 shows that $\frac{dt}{dx} \rightarrow 0$

as $x \rightarrow \sqrt{2}\left(\frac{\sigma}{\rho g}\right)^{\frac{1}{2}}$ Also equation 2.7 shows that $\frac{d^2t}{dx^2} \rightarrow \sqrt{2}\left(\frac{\rho g}{\sigma}\right)^{\frac{1}{2}}$ Thus, the solution of the equation for the entrainment region when the following conditions are fulfilled simultaneously

$$t \rightarrow 0 \tag{2.9}$$

$$\frac{dt}{dx} \rightarrow 0 \tag{2.10}$$

$$x \rightarrow \sqrt{2}\left(\frac{\sigma}{\rho g}\right)^{\frac{1}{2}} \tag{2.11}$$

$$\frac{d^2t}{dx^2} \rightarrow \sqrt{2}\left(\frac{\rho g}{\sigma}\right)^{\frac{1}{2}} \tag{2.12}$$

Conditions (2.9) to (2.12) are suitable limit for the matching of static to moving regions. The function t(x) over the entire region can be obtained from a solution for the entrainment region that can be matched with the solution of the static surface equation at the boundary between the two regions. These matching conditions are given by (2.9) to (2.12). Landau and Levich have solved the problem as follows; A solution to the Navier-Stokes equation close to the plate is matched to the static meniscus far from the plate. The limiting thickness of the liquid layer dragged out by the plate is given by Landau and Levich(1942)

$$t_o = \frac{Q}{V_R} = 0.93\frac{(V_R\mu)^{\frac{2}{3}}}{\sigma^{\frac{1}{6}}(g\rho)^{\frac{1}{2}}} \tag{2.13}$$

Equation 2.13 shows that the limiting thickness of the entrained film is proportional to the withdrawal velocity of the solid and to the liquid viscosity to the two thirds power. The thickness is a weak function however, of the liquid density and surface tension. For high velocities of withdrawal an expression for h_o may be derived by dimensional analysis. The thickness of the liquid film remaining on the solid at high withdrawal velocities cannot depend on the nature of the static liquid meniscus. In other words, t_o is no longer a function of surface tension and is determined exclusively by the quantities g, ρ, μ and V_o. At $V_R >> \frac{\sigma}{\mu}$ This gives

$$t_o = A\left(\frac{\mu V_R}{g\rho}\right)^{\frac{1}{2}} \tag{2.14}$$

The constant A was evaluated by Deryagin(1945) found to be equal to unity. In the general case of an arbitrary withdrawal velocity of the plate we get:

$$t_o = \left(\frac{\mu V_R}{g\rho}\right)^{\frac{1}{2}} f\left(\frac{\mu V_R}{\sigma}\right) \tag{2.15}$$

where the function f($\frac{\mu V_R}{\sigma}$)=f(the capillary number)and it takes the form

$$f\left(\frac{\mu V_R}{\sigma}\right) = 0.93\left(\frac{\mu V_R}{\sigma}\right)^{\frac{1}{6}} \quad for \quad \frac{\mu V_R}{\sigma} << 1 \tag{2.16}$$

$$f\left(\frac{\mu V_R}{\sigma}\right) = 1 \quad for \quad \frac{\mu V_R}{\sigma} >> 1 \tag{2.17}$$

Equation 2.13 and 2.16 has been verified in the experiments of Deryagin and co-workers(1945) and this equation may be used to estimate the thickness of the liquid film formed on the rotating wheel during the melt overflow, provided its radius of curvature is extremely large in comparison to the capillary constant $\sqrt{\left(\frac{\sigma}{g\rho}\right)}$.

2.3.3 Meniscus Characteristics

Ruschak (1976) calculated a relationship between the final film thickness and the radius of curvature of the static meniscus at its apparent point of tangency with the substrate for aqua solutions. The result is

$$\frac{t_o}{R} = 1.34\,(Ca)^{\frac{2}{3}} \tag{2.18}$$

where t_o is the final film thickness and Ca is the capillary number The gross shape of the meniscus is controlled by surface tension and a hydrostatic pressure field on it. More general geometries have been analyzed by Higgins and Scriven(1980). Two static menisci that must be considered are meniscus(R) which forms the film and the wetting meniscus(ξ) which displaces air from the substrate. (Figure 2.3). In practice a pressure difference ΔP is maintained across the liquid in the gap between the lip and the wheel, where ΔP is the amount by which the ambient pressure downstream of coating meniscus exceeds that upstream of the wetting meniscus. The fluid flow in melt overflow process can be simulated as a self-metering coating flow or

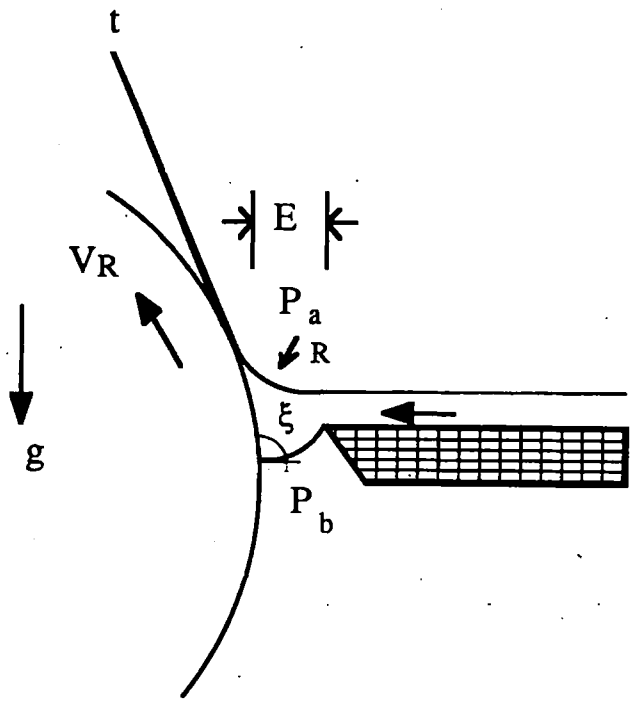

Figure 2.3 Schematic side view of meniscus and developing region.

free withdrawal in which the substrate is withdrawn from a large liquid pool. This type of flow has been reviewed by Tallmadge and Gutfinger(1976). In equation 2.18, R, the radius of curvature of the static meniscus at the film developing point is uniquely determined by the hydrostatic pressure field to be $\sigma/2\rho g\,(1+\sin\alpha)^{\frac{1}{2}}$. where α is the angle between vertical and withdrawal direction. Ruschak(1976) suggested that, simple geometric arguments establish that the uniform pressure in the liquid between the upper and lower menisci must satisfy the following condition;

$$B+(1+\cos\xi)/e \geq -p^0 \geq B-(1-\cos\xi)/e \qquad (2.19)$$

or else a lower static meniscus can not be constructed. Where e=E/C, E is the gap distance and C is the capillary length which is equal to $\sqrt{\frac{\sigma}{\rho g}}$, Pa is the ambient pressure above the developing region, P_b is the below the melt pool/wheel contact area. B=(P_a-P_b)/ρ g C, P_0 is the pressure in the liquid between the static menisci is related to the Levich number, which depends on the properties of the liquid.

Ruschak(1976) also reported that the pressure in the liquid is $-P^0 = C_0 L^{\frac{2}{3}}$, where $L = (\frac{\mu V_R}{\sigma})(\frac{t_0}{C})^{\frac{2}{3}}$, is Levich number, t_0 is limiting film thickness and C_0 is a constant which was determined by Esmail and Hummel(1975). The experimental ξ angles measured by optical photography were almost 180^0 for melt overflow experiments. Therefore equation 2.19 reduces to

$$B \geq C_0 L^{\frac{2}{3}} \geq B - \frac{2}{e} \tag{2.20}$$

This equation appears as a mathematical definition of the physical condition for stable melt pool in melt overflow strip casting process. Further detailed quantitative description of the equation needs more accurate experimental data of meniscus.

2.3.4 Transport Phenomena in the Stationary Melt Pool

The melt overflow process involves the impinging of a molten metal stream onto a rotating chiller of high thermal conductivity (K_{Cu}=363 W.m^{-1}.K^{-1}). A mathematical description of fluid flow and heat flow enables the sheet thickness can be predicted. In order to quantify solute microsegregation and solidification morphology the mathematical model has to be extended to take account of solute mass flow. To describe the transport phenomena in the stationary melt pool where a continuous strip is formed by solidification and extraction of liquid metal from the pool of molten metal at the stagnation point(dwell time of pool) on the wheel (Figure 2.4) the following assumptions are made by Katgerman(1983):

-the pool is semi-infinite in the y-direction which is perpendicular to wheel

-thermal and physical properties are independent of temperature

-the fluid flow is laminar

-normal forces are negligible as compared with shear forces

-there is no slip between metal and substrate

-heat flow is basically in one dimension (y-direction) and can be characterised by a convective heat transfer coefficient h_c

-there is negligible heat transfer to the surroundings

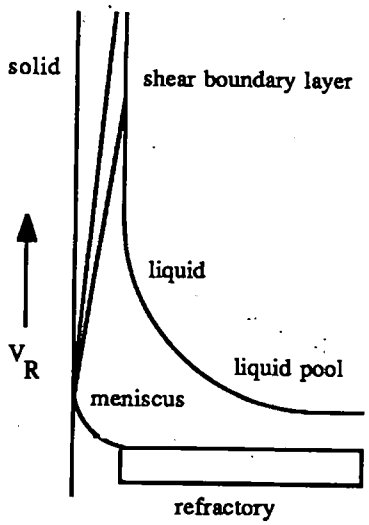

Figure 2.4 Schematic representation of strip formation in melt pool.

-the position of the solid-liquid interface is given by $y = \delta_T(x)$

In this case the governing equations proposed by Katgerman(1983) take the following form for a liquid metal;

$$Continuity \quad \frac{\partial V_x}{\partial x} + \frac{\partial V_y}{\partial y} = 0 \tag{2.21}$$

$$Motion \quad V_x\frac{\partial V_x}{\partial x} + V_y\frac{\partial V_y}{\partial y} = \nu\frac{\partial^2 T}{\partial y^2} \tag{2.22}$$

$$Heatflow \quad V_x\frac{\partial T}{\partial x} + V_y\frac{\partial T}{\partial y} = \alpha\frac{\partial^2 T}{\partial y^2} \tag{2.23}$$

$$Solute \quad V_x\frac{\partial c}{\partial x} + V_y\frac{\partial c}{\partial y} = D_L\frac{\partial^2 c}{\partial y^2} \tag{2.24}$$

where V_x is the velocity component in x direction, V_y is the velocity component in y direction, ν is dynamic viscosity, c is solute concentration, α is thermal diffusivity, D_L is diffusion constant of liquid alloy, T is temperature.

For solid metal

$$Heat \quad V_R\frac{\partial T}{\partial \theta} = \alpha_s\frac{\partial^2 T}{\partial y^2} \tag{2.25}$$

where V_R is wheel speed, α_s is thermal diffusivity of solid, θ is time.

The boundary conditions are:

for the strip-wheel interface;

$$y = 0 \quad K_s \frac{\partial T}{\partial y} = h_c (T - T_w); \quad V_x = V_R; \quad V_y = 0 \tag{2.26}$$

where T_w is wheel temperature, K is thermal conductivity of the solid.

for solid-liquid interface;

$$y = \delta_T(x) \quad V_x = V_R; \quad V_y = 0; \quad T = T_L; \quad c = c_L \tag{2.27}$$

$$y = \infty, \quad V_x = 0; \quad T = T_p; \quad c = c_o \tag{2.28}$$

$$x = 0, \quad \frac{\partial V_y}{\partial x} = 0; \quad \frac{\partial T}{\partial x} = 0 \tag{2.29}$$

where T_l is the liquidus temperature, T_p is the casting temperature, δ_T is the boundary layer thickness.

Conservation of heat and mass of each element at the solid-liquid interface proposed by Katgerman(1983) appears as the following additional equations:

$$Heat \quad K_s \frac{\partial T}{\partial y} - K_l \frac{\partial T}{\partial y} = \rho_s V_R L_f \frac{d\delta_T}{dx} \tag{2.30}$$

$$Solute \quad - D_L \frac{\partial c}{\partial y} = (1 - k)\, c_l V_R \frac{d\delta_T}{dx} \tag{2.31}$$

where K_l is thermal conductivity of liquid, L_f is latent heat, ρ_s is density of solid and k is partition ratio.

The strip thickness, when the metal leaves the pool, consists of a solidified layer and a layer of molten metal on top of it. Hence the calculation of the strip thickness implies solutions of equations (2.21)-(2.24). This requires the known position of the solidification front which is complicated by the fact that the heat flow and fluid flow equations are coupled. As a first approximation the interaction between moving solidification front and flow field has been neglected and consequently the velocity distribution can be calculated independently. Equations 2.21 and 2.24, which are boundary layer type equations can be solved approximately by the Von Karman integral method, (Schlichting (1979)). By solving equation 2.21 for V_y (using the

boundary condition V_y=0 at y=0) and substituting the resulting expression into equation 2.22 we get a non-linear equation for V_x(x,y):

$$V_x \frac{\partial V_x}{\partial x} \left(\int_0^y \frac{\partial V_x}{\partial x} \right) \frac{\partial V_x}{\partial y} = \nu \frac{\partial^2 V_x}{\partial y^2} \tag{2.32}$$

Solution of this non linear equation assuming the velocity profiles remain similar at various values of x, boundary layer thickness was formulated and is given by Katgerman(1983).

$$\delta_m(x) = 6.48 \sqrt{\frac{\nu x}{V_R}} \tag{2.33}$$

and the resulting velocity profiles can be calculated accordingly. An exact numerical solution of equation 2.32 with the same boundary conditions by Shinqu and co-workers (1982) gave $\delta_m(x) = 6.4\sqrt{\frac{\nu x}{V_R}}$. The approximate analytical solutions of V_x and V_y in the boundary layer can be substituted into the heat and solute flow equations 2.23-2.25. These equations with boundary conditions 2.26-2.31 can be solved by numerical techniques as described by Katgerman(1983). The calculated velocity and temperature profiles are related to the strip thickness by $t_s = \delta_m(x) + \delta_T(x)$. The momentum contribution δ_m to the total strip thickness is usually calculated from the boundary layer thickness and is defined as that thickness for which $V_x(x, y)$ has dropped to a value of $0.01V_R$. This is an arbitrary definition and it is more appropriate (as proposed by Vincent et al (1983)) to use the displacement thickness δ_1 defined by Schlichting(1978):

$$V_R \delta_1 = \int_0^\infty V_x(x, y)\, dy \tag{2.34}$$

The displacement thickness was calculated by Katgerman(1983) in the explicit form

$$\delta_1 = 1.62 \sqrt{\frac{\nu x}{V_R}} \tag{2.35}$$

In both definitions the calculated momentum thickness is independent of the substrate velocity and consequently the physical condition that the liquid metal has to be dragged out the melt pool is not satisfied. To include this condition, the boundary layer thickness is defined as that distance for which

the average dynamic pressure of the fluid exceeds the surface tension of the pool. This can be expressed as follows, (Katgerman(1983)):

$$\frac{1}{2}\rho_L < V_x^2(x, \delta_m) > 4\frac{\sigma_{LV}}{d} \tag{2.36}$$

where ρ_L is liquid metal density, d is residence distance of melt pool on the chiller, σ_{LV} is surface tension of liquid- vapour interface. The dynamic pressure which appears as the velocity of mass flow- V_x in above equation is also a critical term at the beginning of strip casting. In order to cast continuous strip the pressure in mass flow has to be sufficient enough to overcome the surface tension of the liquid front.

2.4 The Enthalpy Method for Modelling Heat and Mass Flow

A common feature of the strip casting process is the thinness of the melt on the casting substrate. A small cross section is required in order to produce the desired solidification rates. Additionally, the melt layer is usually elongated in the casting direction with the result that the fluid flow phenomena in the casting substrate, result in the condition known as thin film flow. It is well known that the flow in thin liquid films can often be represented by the theory of lubrication, Gutierrez and Miravate(1988). This theory is based on the following assumptions;

1) Since the liquid film is thin, the pressure can be assumed constant across the thickness.

2) Since the film is long, the component of velocity in the through thickness direction can be neglected in comparison with the component along the length of the film.

3) The inertia forces are negligible in comparison with the viscous forces. The introduction of these assumptions leads to considerable simplification the analysis of fluid flow in thin liquid films. Analytical solutions of the Navier-Stokes equations become possible under these conditions and have been available for a long time. The liquid film formation and limiting

thickness of film flow were investigated and formulated by Levich and Landau(1942). This theoretical approach was given in section 2.3.2 under the topic of "Liquid Film Flow at Small Capillary Number". The theory of lubrication has been combined with a solidification model to produce a mathematical representation of the twin roll rapid solidification process, (Miyazawa and Szekely(1981)).

Since, in the case of strip casting with a single quenching surface the film surface opposite to the melt-chill interface is actually a free unconstrained surface and its motion must be controlled in order to obtain steady conditions. The theory of capillarity was developed by Flinn(1986) to analyze the shapes of free liquid surfaces. The theory of capillarity, the theory of lubrication and a solidification model have been combined to produce a mathematical representation of the casting of thin foils(about 50 μm) by the planar flow casting process by Gutierrez-Miravete(1986) and Gutierrez-Szekely(1986). Calculations carried out by Gutierrez and Miravete(1986) and Yu(1987) neglected the so-called Marangoni effect, However it has been shown that this assumption proposed by Gutierrez and Szekely(1986) is appropriate in many cases. It has been reported by Gutierrez that the predictions of the model are in reasonable agreement with experiments of the casting of 400 μm thick low carbon steel strip by melt overflow process performed by Hackman and Gaspar(1986). The streamline pattern and temperature field in the meniscus were investigated and predicted by Gutierrez(1986). Figure 2.5 shows the computed fluid flow pattern inside the meniscus and melt overflowing from the pouring lip and impinging on the chill which is moving upward direction, (Gutierrez(1986)). The streamline pattern shows two distinct flow regions inside the puddle. Next to the moving chill the streamlines are compressed and more or less uniformly spaced. This is a result of the solidification and the viscous drag exerted on the melt by the partially solidified strip. The flow in this region is along the casting direction. Next to this region of through flow there is a larger slow moving region where the melt recirculates inside the molten pool. Fluid flow patterns like the one shown in Figure 2.5 are a common occurrence in lubrication and thin

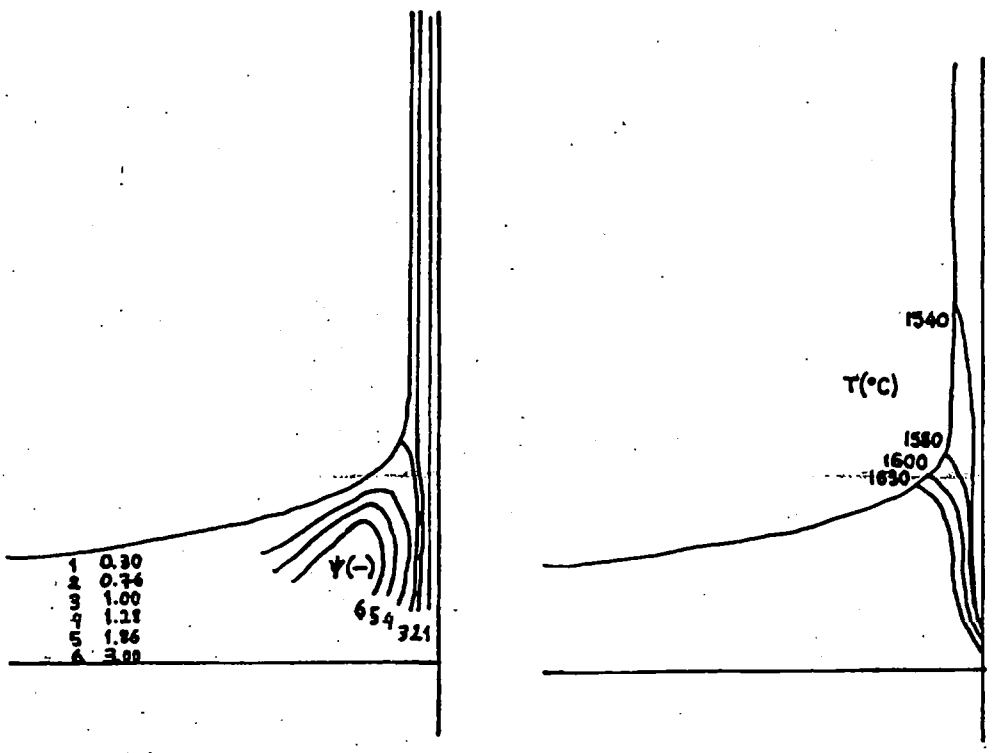

Figure 2.5 Fluid flow map and temperature field in the meniscus of melt overflow proposed by Gutierrez(1986).

film flow, (Schlichting(1979)). The computed temperature field associated with the flow map in Figure 2.5 as expected. The temperature gradients are concentrated in the vicinity of the chill and decrease gradually from the point of impingement. Furthermore, the temperature in the bulk of the puddle is quite uniform and very close to the pouring value. The calculations carried out by Gutierrez(1986) showed that the actual location of the free surface is closely related to the solidification rate which is given in equation 2.39 and 2.44. The temperature field proposed by Gutierrez in Figure 2.5 shows an isotherm $1580 - 1540^0C$ at the region beyond the meniscus zone.

The particular solidification model employed by Gutierrez and Szekely(1988) is called the enthalpy method. The model defines the stream function of liquid flow inside the meniscus formed in the melt overflow process. The authors derived the following mathematical equations for the model; Stream function in terms of mass flow rate-Q, velocity in x direction-V_x

$$\psi = \frac{V_x y}{\frac{Q_v}{w}} \qquad y < y_s \tag{2.37}$$

$$\psi = \frac{\left(V_x y_s + \frac{A_2\left(y^3 - y_s^3\right)}{3} + A_1\left(y^2 - y_s^2\right) + A_o\left(y - y_s\right)\right)}{\frac{Q_v}{w}} \qquad y > y_s \tag{2.38}$$

$$\frac{d^3 t_l}{dx^3} = \left(\left(\frac{Q_v}{w}\right) - V_x\left(t_l + y_s\right) - \gamma T_x\left(\frac{t_l^2}{2\mu}\right)\right)\left(\frac{3\mu}{t_l^3 \sigma}\right) \tag{2.39}$$

$$A_2 = \left(V_x\left(t_l + y_s\right) - \left(\frac{Q_v}{w}\right) + \gamma T_x\left(\frac{t_l^2}{2\mu}\right)\right)\left(\frac{3}{2} t_l^3\right) \tag{2.40}$$

$$A_1 = \frac{\gamma T_x}{\mu} - 2\left(t_l + y_s\right) A_2 \tag{2.41}$$

$$A_0 = V_x - \frac{\gamma T_x y_s}{\mu} - \left(y_s^2 - 2\left(t_l + y_s\right) y_s\right) A_2 \tag{2.42}$$

$$\gamma = \frac{d\sigma}{dT} \tag{2.43}$$

$$T_x = \frac{dT}{dx} \tag{2.44}$$

where

x is the distance along the casting direction

y is the distance along the thickness of the film

ψ is stream function

$\frac{Q_x}{w}$ is the volumetric flow rate per unit width

V_x is the velocity of the moving chill

t_l is the thickness of liquid layer

μ is the viscosity of melt

σ is surface tension of alloy

T is temperature

These equations were used by Gutierrez and Miravette(1988) in combination with an empirical solidification model to simulate planar flow casting of 200 μm thick aluminium foils by Yu(1987) and good agreement was reported.

2.4.1 The Nature of Liquid Flow

In the analysis of the strip casting process the flow in the pool is generally assumed to be laminar at least outside the vicinity of the liquid solid transition layer which is subjected to very high shear, (Yavari and Desre(1981)). The Reynold's number R, which characterizes the liquid flow is given by

$$R = V_{liq} l.\rho/\mu \tag{2.45}$$

where V_{liq} is the flow speed, l is a characteristic length, ρ is liquid density and μ the kinematic viscosity. For the Reynold's number R, between 500 and 1500, turbulent flow can develop, for example in between a stationary and a moving plate, Landau(1959). Assuming the characteristic length is equal to melt puddle length(which is about 15mm measured on the photographs of the melt overflow experiments) a Reynold's number such as 605 can be calculated from equation 2.44 for liquid stainless steel density 7000 kg.m^{-3} and kinematic viscosity 0.006 N.sec.m^{-2} Thus, the question arises

as to whether turbulent flow occur in a melt pool during direct strip casting processes. The Reynold's number R, can be written for melt spinning as (Yu(1987)):

$$R = \frac{V_{liq} . l_a . \rho}{\mu (\tau / l_a)^2} \tag{2.46}$$

where l_a is nozzle length. For large values of the numbers, inertia becomes important so boundary layer theory must be used. Also well developed channel flow exists along the nozzle gap, Yu(1987). By contrast, the existence of channel flow at the free side of the lip is not possible in melt overflow. The planar flow mathematical models developed at MIT and supplied by NASA show recirculatory flow at the nozzle/wheel interface. Dantzig(1988) also predicts a recirculaton zone in the lip at the same interface. This phenomenon was observed on a highspeed camera film of our experiment. Recirculatory flow may be responsible for the free cast surface roughness that can be found on many crystalline or partially amorphous strips. This may originate from the breaking of growing solidified dendrite tips or entire grains by the recirculating liquid. These solid particles then redistribute themselves on the top surface.

2.4.2 Relationship of strip dimensions to casting conditions

The thickness of melt overflow strip has been investigated by several investigators. In the mathematical model developed by Gaspar, et al(1986) based on heat transfer analysis, thickness is controlled by heat transfer coefficient h_c and residence time of pool (for which the melt pool is contact with chill surface) θ_R. The model considered thickness formation by heat transfer associated with conduction through the liquid metal pool in contact with the chiller, heat transfer across the wheel/strip interface and the total heat evolved due to latent and superheat being released from the solidified layer. The heat transfer by conduction + convection was assumed to be equal to the latent and superheat released. Assuming that the temperature of the gas/liquid metal interface is around the solidification temperature, basic heat transfer due to conduction in the solidified layer can be written

as;

$$q = K\frac{T_m - T_s}{t} \tag{2.47}$$

where T_m is solidification temperature, T_s is the absolute interface temperature and t is the thickness of liquid layer dragged out of the melt pool, K is the conductivity of the solid phase.

The heat transfer at the solidifying metal-wheel interface can be defined as:

$$q = h(T_s - T_w) \tag{2.48}$$

where T_s is the interface temperature, T_w is the wheel temperature and h is the heat transfer coefficient across the wheel/strip interface. Combining conduction and convection equations yields

$$q = \frac{T_m - T_w}{\frac{1}{h} + \frac{t}{K}} \tag{2.49}$$

The total heat evolved due to latent and superheat is given by

$$q = \rho\left(H_f + C_{pl}\triangle T_s\right)\frac{dt}{d\theta} \tag{2.50}$$

where H_f is latent heat of fusion, C_{pl} is the heat capacity of the molten metal and $\triangle T_s$ is the superheat of the melt. The densities (ρ) of the solid and liquid phases at the melting temperature were assumed to be equal. Equating equations we get

$$\rho\left(H_f + C_{pl}\triangle T_s\right)\frac{dt}{d\theta} = \frac{T_m - T_o}{\frac{1}{h} + \frac{t}{K}} \tag{2.51}$$

This equation can be integrated for with thickness t=0 at time θ=0 and t=t_o at the end of residence time of the mushy zone $\theta = \theta_R$. θ_R is measured experimentally by photography which is about 0.005 sec for the melt overflow experiments. The above equation was rearranged in the following form;

$$h_c\left(T_m - T_w\right) = \frac{\rho_s H_{ef}}{\theta_R}\left(t^2\frac{h}{2K} + t\right) \tag{2.52}$$

where $H_{ef} = H_f + C_{pl}\triangle T_s$. The thickness values that have been calculated for melt overflow of stainless steel are presented in chapter 9. This model is based on the assumptions that the interface resistance to heat flow dominates

that offered by the freezing metal and heat originates from latent heat, specific heat within the melt. The wheel temperature is constant at T_w and the temperature at the casting side of interface is constant (T_m). The metal freezes as a plane at x=t where the temperature is at the freezing point of the metal, T_m; and the temperature profile within the solidifying metal layer is a linear function. Figure 2.6 presents a schematic diagram of the temperature profile in the solidifying strip, Gaspar(1986).

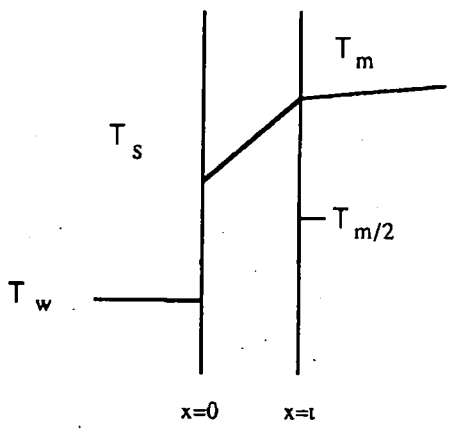

Figure 2.6 Temperature profile at the strip/chiller interface due to interface resistance

Another thickness prediction by Maringer(1987) based on empirical calculations from experimental data yields the following equation

$$t = K\left(\frac{X}{V_R}\right)^n \tag{2.53}$$

where x is the liquid metal depth at the lip, V_R is the wheel speed, and K is a constant. The value of the exponent n varies from 0.5 to 1 for a particular lip/wheel contact angle α. Figure 2.7 presents the process characteristics presented above. Evaluation of this formula and the experimentally deter-

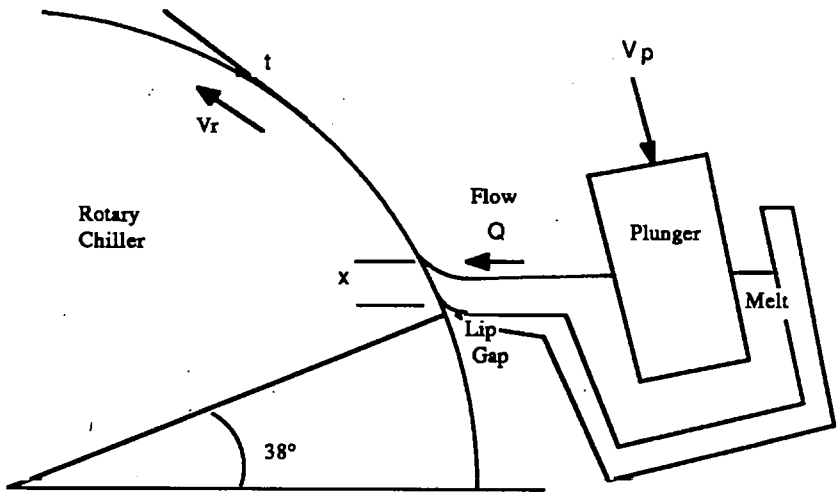

Figure 2.7 Melt overflow process characteristics

mined value of n will be given in chapter 8.

A number of factors influence the formation of the strip. These can be classified into two groups. The first group consists of material properties, such as viscosity, density and surface tension which are inherent properties of the material being cast. The second group is the processing parameters, such as the wheel speed, plunger speed, liquid metal depth. The last two parameters are interrelated by the volumetric flow rate. The effect of varying wheel speed, viscosity and surface tension on the thickness has been simulated by using a finite element computer programme, (Brasmer(1979)). It has been suggested that, the viscosity of the melt had a direct influence on the thickness of the strip. For a constant velocity, a high value for viscosity (10^3 g.mm^{-1}.s^{-1}) resulted in a strip thickness on the order of 200 . As the viscosity was reduced in the model the thickness of the strip increased to about 5000 μm, (Brasmer (1979)). For a constant viscosity, a high velocity value results in a thin strip and decreasing the velocity increases the thickness. These parameters can be combined into a dimensionless number

which was described in section 2.3.2 (equation 2.13). This dimensionless number is the capillary number $Ca = \frac{\mu V_R}{\sigma}$. Increasing the velocity or viscosity increases the capillary number and results in a thinner strip. Similarly decreasing the surface tension increases the capillary number and results in a thinner strip. The depth of the melt also has an effect on the thickness of the strip. If the depth were increased, the thickness of the strip would increase correspondingly.

The question that arises here is whether a liquid film reachs its limiting thickness before solidification is completed. The thickness prediction in equation 2.13 is accurate and consistent with experimentally obtained data. It is of interest to show the consistency of empirical relations between strip dimensions and process variables. Previous empirical relations derived by Liebermann and Graham(1976), Cantor and Cheese(1980), Liebermann(1980), Kavesh(1976) all found a strong inverse relationship between strip thickness and wheel speed, with little effect on width for melt spinning. In contrast the width was found to be strongly dependent on flow rate, with a weak dependence on thickness, Kavesh(1976). The most commonly quoted functional relationships, derived by Kavesh are shown below

$$t = C\frac{Q^{1-n}}{V_R^n} \tag{2.54}$$

$$w = B\frac{Q^n}{V_R^{1-n}} \tag{2.55}$$

where C and B are material constants and, $n = 1/2 - m$, where m is the slope of the liquidus curve. Experimentally determined values of these constants will be presented in Chapter 8. Hillman and Hilzinger(1978) measured the melt pool dimensions of an Fe-40Ni- 14P-6B alloy using still photography. They found that the melt pool was typically 1-2 mm high and 30-50 times thicker than strip produced, but that the strip thickness (t) may be related to the melt pool length(l) and substrate velocity(V_R).

$$t \quad \propto \quad (\theta_R)^{0.53} \tag{2.56}$$

where θ_R(residence time of strip)=melt pool length(l)/V_R The measured

melt pool dimensions of the melt overflow process are given in Figure 8.7 and its effect on product quality will be discussed in chapter 8.

Chapter 3

Melt Instabilities In Rapid Solidification Processes

3.1 Introduction

Direct casting of liquid metal on to a rotating chiller requires special conditions for producing continuous strips. Maintaining and providing laminar liquid flow is one of the important parameters for sound strip production. It is shown that lateral variations in the thickness of the ribbon at any particular strip section are directly related to the pool shape at an instant of time. Longitudinal dimensional variations in the thickness or width of the strip indicate an unstable melt pool whose shape varied with time. These dimensional variations can be minimized by using nozzle or lip geometries, jet velocities, and pool sizes that induce uniformity and steadiness in the fluid flow.

3.2 Waves and hydrodynamic instability within the melt pool

Hydrodynamic instabilities in a melt pool originate from the interaction between the thin gas boundary layer flow and the flowing liquid metal strip just at the beginning of the liquid pool. The Kelvin-Helmholtz instability, the Marangoni instability and capillary waves have to be considered to describe

the effect of process parameters on the quality and uniformity of directly cast strip.

Kelvin-Helmholtz instability arises at the interface between differentially moving fluids, (Kavesh(1976)).

The Marangoni instability is a bulk flow arising from local variations of surface tension, (Brimacombe and Weinberg(1972)).

The term "capillary waves" is used by Levich(1962) to describe wave motion which penetrates only to a depth of the order of one wavelength. Such waves may arise from random perturbations of any source. They may arise from turbulence within the melt puddle or from air boundary layer separation(eddying) on its surface.

The velocity difference between the rotating chilled wheel and liquid metal stream determines the conditions which may promote perturbations in the liquid state and edge serrations after solidification outside the melt pool. Excessive stream velocities may cause the formation of a circular hydraulic jump. The turbulent disturbance around the outer periphery of this hydraulic jump would cause the pool to be irregular both in space and time which, in turn, would cause the resulting strip to be irregular both accross its width and along its length, (Anthony and Cline(1978)). As the liquid metal stream travels from the lip to the moving chilled substrate, standing or travelling capillary waves can form on the liquid stream. These waves are initiated at sources generally at the orifice during melt spinning or at the lip during melt overflow and in the puddle. In addition, capillary waves can be generated along the jet by the interaction between the atmosphere and the stream in a manner analogous to the formation of a capillary wind wave on a lake. The velocity of capillary waves C_λ of wavelength λ is determined from a balance between inertia forces and surface tension, Batchelor(1970) and is given by

$$C_\lambda = \sqrt{\frac{2\pi\sigma_{l_v}}{\rho\lambda}} \tag{3.1}$$

where λ is the wavelength of the capillary wave, and ρ is the density of the liquid metal. (C_λ=12.2×10^2 mm/sec, for λ=10^{-1} cm, ρ=7.87g/cc and σ_{l_v}=1872 dyn/cm). Because the capillary-wave velocity lies in a range at-

tainable by the stream velocity, it is possible to operate at a stream at a high enough velocity V_j to sweep all incipient capillary waves of some critical wavelength downstream and thereby prevent their formation in a manner analogous to the common hydraulic jump, (Rouse(1946)).

$$V_j > C_\lambda^{cr} \tag{3.2}$$

From equations (3.1) and (3.2), it is apparent that it is not possible to eliminate all capillary waves, since $C_\lambda \to \infty$ as $\lambda \to 0$. However, since not all waves will grow on a eliptical stream, it is sufficient to eliminate any waves that will be spontaneously develop, other wavelengths being damped. In a stream of radius R_j capillary waves of wavelength λ less than $2\pi R_j$ are damped and only those wavelengths greater than $2\pi R_j$ are unstable, according to Plateau(1873). Capillary waves will grow only if

$$\lambda_c > 2\pi R_j \tag{3.3}$$

Figure 3.1 shows the stability and unstability conditions for capillary waves travelling on the liquid stream. The combination of equations (3.1), (3.2), (3.3) yields the minimum stream velocity V_j required to wash away these instabilities

$$V_j > \sqrt{\frac{\sigma_{lv}}{R_j \rho}} \tag{3.4}$$

The stream velocity not only must be large enough to wash away any instabilities developing in the stream. Otherwise the impingement of these instabilities on the puddle would cause a time variation in the puddle size and similar variations in the strip dimensions. Rayleigh, has shown that the amplitude K of the fastest growing instability increases with time as, (Liebermann and Graham(1976)).

$$K = K_o \exp(q\theta) \tag{3.5}$$

$$q = 0.34\sqrt{\frac{\sigma_{lv}}{R_j^3 \rho}} \tag{3.6}$$

where K_o is the initial amplitude of the instability, θ is the time since the initiation of the instability. For a stream length L_j moving at a velocity

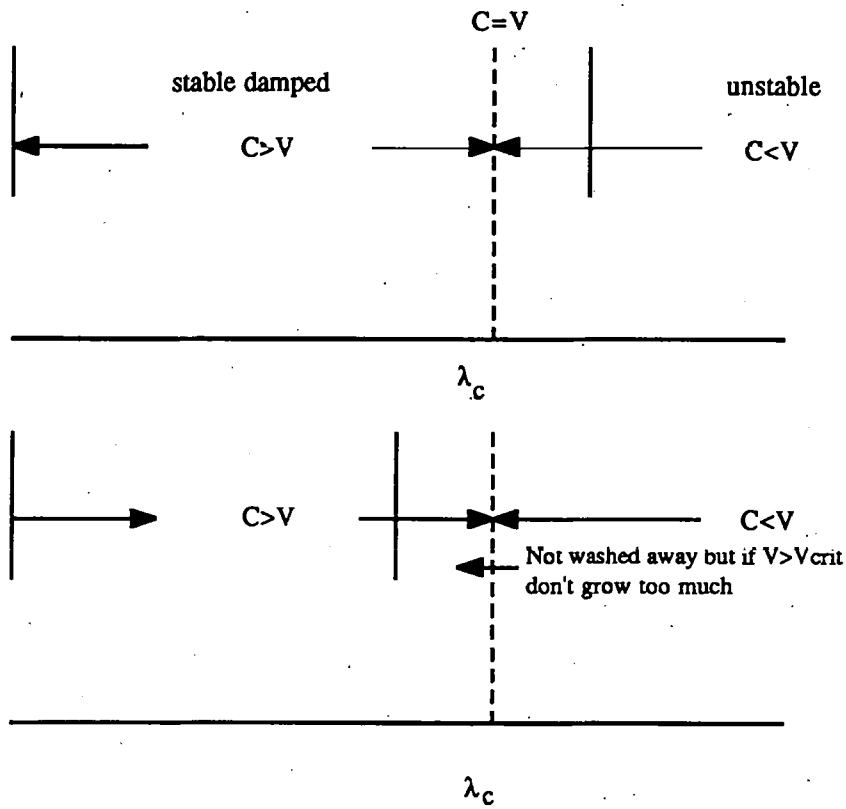

Figure 3.1 The diagram for the stability and unstability conditions on the liquid surface due to capillary waves

V_j, the time available for an instability to grow will be of the order of $\theta = \frac{L_j}{V_j}$ then equation (3.6) and the fact that θ together yield the minimum stream velocity V_j required to suppress growth of remain unwashed capillary instabilities on stream, considering the increase of amplitude of an instability is limited to a factor of 10 from its very small initial value.

$$V_j > \frac{L_j}{\ln 10}\sqrt{\frac{\sigma_{lv}}{R_j^3 \rho}} \tag{3.7}$$

It has been reported by Anthony and Cline(1978), that excessive stream velocities should be avoided to prevent the formation of a circular hydraulic jump on the substrate similar to the circular hydraulic jump that forms on a plate below a kitchen water tap. Therefore the stability of the liquid pool is important because both extreme conditions may exist during casting such as insufficient liquid metal pressure and stream velocity or excessive stream velocities. So it can be suggested that a critical conditions to reach a balance and maintain liquid flow steady are governed by both process parameters such as stream length L_j, stream diameter R_j and alloy characteristics such as surface tension and density described by equation (3.7)

3.3 Kelvin-Helmholtz Instability

The Kelvin-Helmholtz instability arises as a result of the pressure perturbation exerted by the gas which is accelerated by the rotating wheel. This can do work on the liquid strip/gas interface and at a sufficiently large relative or differential velocity the instability can tear apart the molten strip. The agreement is good between experiments and Kelvin-Helmholtz instability predictions for oils with the higher viscosity associated with molten metals, Hull(1989). Chang and Russell(1965) showed that at low Mach numbers the stability conditions between a compressible gas stream and an adjacent liquid layer do not differ significantly from those of incompressible gas flows. They also showed that at sonic and supersonic gas velocities the system is always unstable despite the stabilizing influence of surface tension. Nayfeh and Saric(1971) concluded that at a low liquid Reynold's number and with

subsonic gas flow, stability conditions are independent of viscosity. In linear analysis the nonlinear motion of the gas has no effect and the nonlinear motion of the viscous liquid is stabilizing. The instability condition predicted numerically for two uniform fluid half planes in relative vertical motion separated by a vertical boundary assuming stream velocities V_1 and V_2 plus densities ρ_1 and ρ_2 are constant was analyzed by Chandrasekhar (1961). The stabilizing effect of surface tension has been investigated and formulated by Chandrasekhar(1961). Surface tension can suppress the Kelvin-Helmholtz instability if

$$(V_1 - V_2)^2 < \frac{2}{\alpha_1 \alpha_2} \left[\frac{\sigma_{LV} g (\alpha_1 - \alpha_2)}{\rho_1 + \rho_2} \right]^{\frac{1}{2}} \tag{3.8}$$

where ρ is density, $\alpha_1 - \frac{\rho_1}{\rho_1+\rho_2}$, $\alpha_2 - \frac{\rho_2}{\rho_1+\rho_2}$, σ_{LV} is surface tension and g=9.81 m.sec^{-2}. A velocity difference of 6.5 m.sec^{-1} was reported for the stability condition for air flowing over water by Chandrasekhar(1961). Therefore, when $(V_1 - V_2)$ exceeds 6.5 m.sec^{-1} instability will manifest itself as surface waves with wavelength 17.1 mm. The calculations yield a critical velocity difference $(V_1 - V_2)$=22.9 m.sec^{-1} between liquid stainless steel and air assuming stainless steel density $\rho_2 = 7100 Kg.m^{-3}$ and air density $\rho_2 = 1.293 Kg.m^{-3}$, $g = 9.81 m.sec^{-2}$ surface tension between liquid and air $\sigma_{LV} = 1.4 N.m^{-1}$. If the velocity difference exceeds 22.9 $m.sec^{-1}$ Kelvin-Helmholtz instability may exist but melt overflow experiments were performed difference not more than 2.7 $m.sec^{-1}$ and instabilities were observed even the velocity difference is smaller than 22.9 $m.sec^{-1}$. It has been reported that if the thickness of gas flow is thin wheel enhance the pressure variations of the gas flow and decrease the critical gas velocity, Kordyban(1977).

Chapter 4

Heat Transfer In Melt Overflow

4.1 Introduction

Heat flow and transfer conditions in melt are particularly important before the stream reaches the lip/wheel contact point. It is important for process stability that the thermal conditions in the lip have reached a steady state. It is necessary to prevent thermal shock which can damage the ceramic pouring channel and lip but also to allow transport of liquid metal to the wheel contact point. For a particular direct strip casting process the mass flow rate Q governs the thickness of strip, but in melt overflow it also controls the heat transfer in the pouring channel. Figure 4.1 represents the flow diagram at different stages existing in the melt process modelled in this study.

In stage 1, the system is designed to store heat with minimal loss but at stage 2, the system needs to loose heat rapidly. The function of the water cooled wheel is to create a heat sink and maintain unidirectioned rapid solidification in a time interval θ_R and the transfer wheel momentum to the viscous undercooled liquid layer by dragging it from the liquid pool in front of the lip. In this chapter, first heat transfer analysis of the solidifiying strip will be carried out studying one dimensional heat flow by conduction through thickness of the strip, radiation heat transfer from free surface to the surroundings and heat transfer by convection at the wheel/strip interface, then the contact pattern of a strip on a chiller will be reviewed.

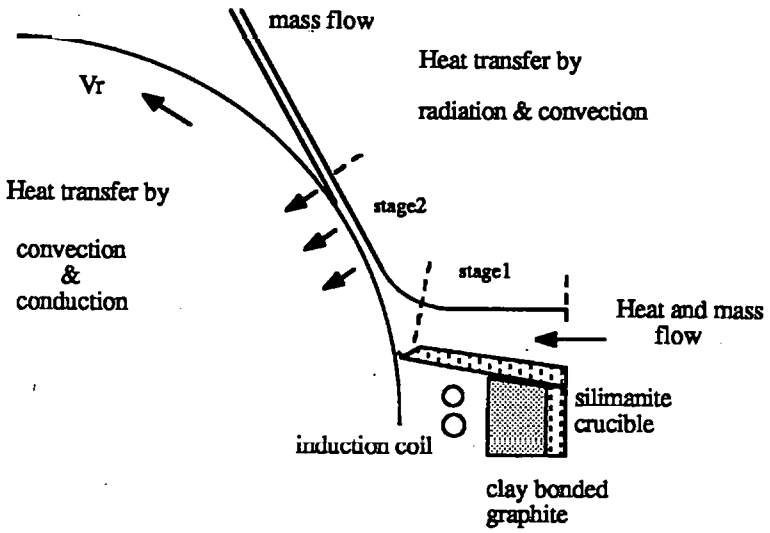

Figure 4.1 Heat and mass transfer diagram of melt overflow.

4.2 One Dimensional Heat Flow

The melt process studied is a rapid solidification process such that the maximum cooling rate that can be achieved is about $10^4 K.s^{-1}$. Higher cooling rates are reported ($10^5 - 10^6 K/s$) for chill block melt spinning, (Flemings(1985) Gillen and Cantor(1985)). When liquid metal bonds to a chilled substrate temporary microwelds form at the solidified strip/wheel interface. Heat is transferred through the thickness and the strip-wheel interface to the wheel while the solid-liquid interface moves in an opposite direction. The heat transfer analysis of stage 2 in Figure 4.1 can be described as:

1) Heat transfer by radiation to the surroundings
2) Heat transfer by conduction through the thickness
3) Heat transfer by convection at strip/wheel interface
4) Convective air at free surfaces.

These will be considered in the following terms:

1) Heat transfer by radiation Q_R is described by Stefan's Law:

$$Q_R = A\sigma_s\epsilon\left(T_{sur}^4 - T_o^4\right) \tag{4.1}$$

where σ_s is the Stefan's constant ($=5.67\times10^{-8}W/m^2K^4$), ϵ is emissivity (0.15-1) and A is the radiating area. T_{sur} is the top surface temperature, T_o is the ambient temperature of the surroundings. Equation 4.1 can be evaluated for stage2 which starts after the strip leaves the melt pool describing a unit element dx and integrating within an area bounded by initial lip/wheel contact point x=0 and the end of residence distance $x = d_{res}$. Figure 4.2 represents a mathematical description of top surface of the overflowing stream. The radiation heat loss within element dx is $\epsilon\sigma_s(T(x)^4 - T_o^4)wdx$ and the

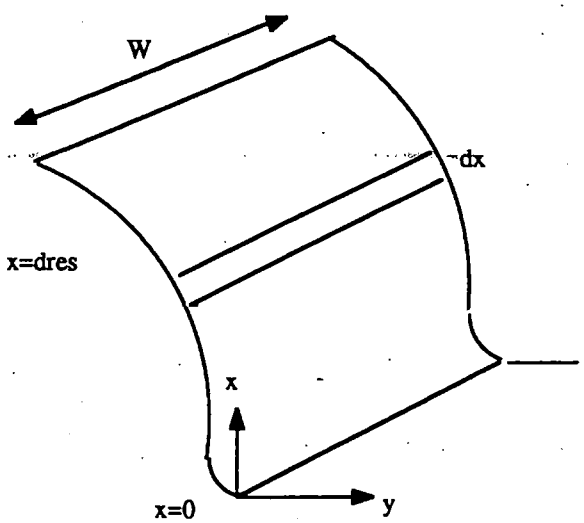

Figure 4.2 Mathematical definition of the free surface where the heat transferred by radiation in melt overflow.

total radiation heat loss along the whole top surface neglecting the relatively small term in T_o^4 can be calculated as

$$Q_R = \int_0^{d_{res}} \epsilon\sigma_s T_{sur}(x)^4 w\, dx \tag{4.2}$$

The top surface temperature $T_{sur}(x)$ can be written assuming a linear variation as:

$$T_{sur}(x) - T_{sur}(o) - \left(\frac{T_{sur}(o) - T_{sur}(d_{res})}{d_{res}}\right), x \tag{4.3}$$

Substituting equation (4.3) into (4.2) yields

$$Q_R = \int_0^{d_{res}} \epsilon\sigma_s w \left(T_{sur}(o) - \left(\frac{T_{sur}(o) - T_{sur}(d_{res})}{d_{res}}\right) x\right)^4 dx \tag{4.4}$$

Assuming a residence area of $9\times10^{-4}m^2$ the radiation heat loss for 304 stainless steel strip was calculated to be 16.35 joule/sec for a typical residence time interval θ_R of 0.03 sec.

2)Heat transfer by conduction through the thickness:

Analytic solution is possible without introducing the releasing of latent heat for the cases:

a) Non-Newtonian no interface

b) Newtonian interface only

Numerical solution is possible introducing the releasing of latent heat for the case of Non-Newtonian with interface.

The basic relation for one dimensional heat flow by conduction within the strip and the substrate (wheel) regions can be written as

$$\frac{\partial T}{\partial \theta} = \alpha \frac{\partial^2 T}{\partial y^2} \tag{4.5}$$

An analytical expression can be obtained for non-Newtonian conditions, allowing for temperature gradients through the strip thickness but neglecting temperature gradients within the wheel. An analytical solution of equation(4.5) has been given by Geiger(1973);

$$T - T_w = (T_i - T_w) \sum_{n=1}^{\infty} \frac{\sin\lambda_n t \quad \exp(\lambda_n \alpha\theta)\cos\lambda_n y}{\lambda_n t + \sin\lambda_n t \cos\lambda_n t} \tag{4.6}$$

where T_w is the wheel temperature, T_i is the initial strip temperature, T is strip temperature as a function of distance (y) through the thickness from the strip/wheel interface; θ is the time variable, K and $\alpha = \frac{K}{\rho C_p}$ are the strip thermal conductivity (26 W/m°K) and diffusivity respectively; t is the strip thickness. Therefore $\lambda_n\left(\frac{n\pi}{t}\right)$ is the n th root of the transcendental

equation obtained from the positive roots of $(\lambda_n t)\tan(\lambda_n t)$=Bi, where Bi is the Biot number which is the ratio of thermal conductance at the surface to the thermal conductivity of the strip, $\left(Bi = \frac{ht}{K}\right)$.

For any condition where the Bi value is less than 0.015, Newtonian cooling is a reasonable approximation. The cooling is essentially ideal when Bi value is greater than about 30 and is intermediate between these values, Ruhl(1967). Under Newtonian cooling conditions, temperature gradients through the thickness of the melt overflow strip and water cooled wheel are negligible, and heat removal from the strip controlled by resistance to heat flow across the strip/wheel interface. The cooling rate $\frac{\partial T}{\partial \theta}$ of strip is then, (Cantor(1982))

$$\frac{\partial T}{\partial \theta} = -\frac{h_i (T - T_w)}{t\rho Cp} \tag{4.7}$$

Where h is the heat transfer coefficient at the strip/wheel interface, ρ is the density and C_p is the specific heat capacity of the strip. Integration of equation 4.7 shows that the average strip temperature decays exponentially with time

$$(T - T_w) = (T_i - T_w) \exp\left(\frac{-h_i \theta}{t\rho Cp}\right) \tag{4.8}$$

where θ time, and T_i is the inital strip temperature at $\theta = 0$, where the strip is fully liquid. Figure 4.3 shows schematic temperature profiles through the strip.

At this point it is necessary to undertake numerical analysis, Finite difference integration of a single non-linear parabolic partial differential equation in one space variable was utilized to analyze temperature profiles through the thickness of the strip. A finite difference form of equation 2.25, (Ruhl (1967)) is;

$$T_i' = \frac{\alpha \Delta \theta}{V_R (\Delta x)^2} \left(T_{i-1} + \left(\frac{(\Delta x)^2 V_R}{\alpha \Delta \theta} - 2 \right) T_i + T_{i+1} \right) \tag{4.9}$$

where T_{i-1}, T_i and T_{i+1} are temperature at three adjacent points spaced Δy apart at time θ. T_i' is the temperature at point i at time $\theta + \Delta\theta$. The above equation with convective heat transfer boundary condition (Equation 2.26) can be integrated directly to produce a temperature matrix of position and time. Time and position increments were studied with care in

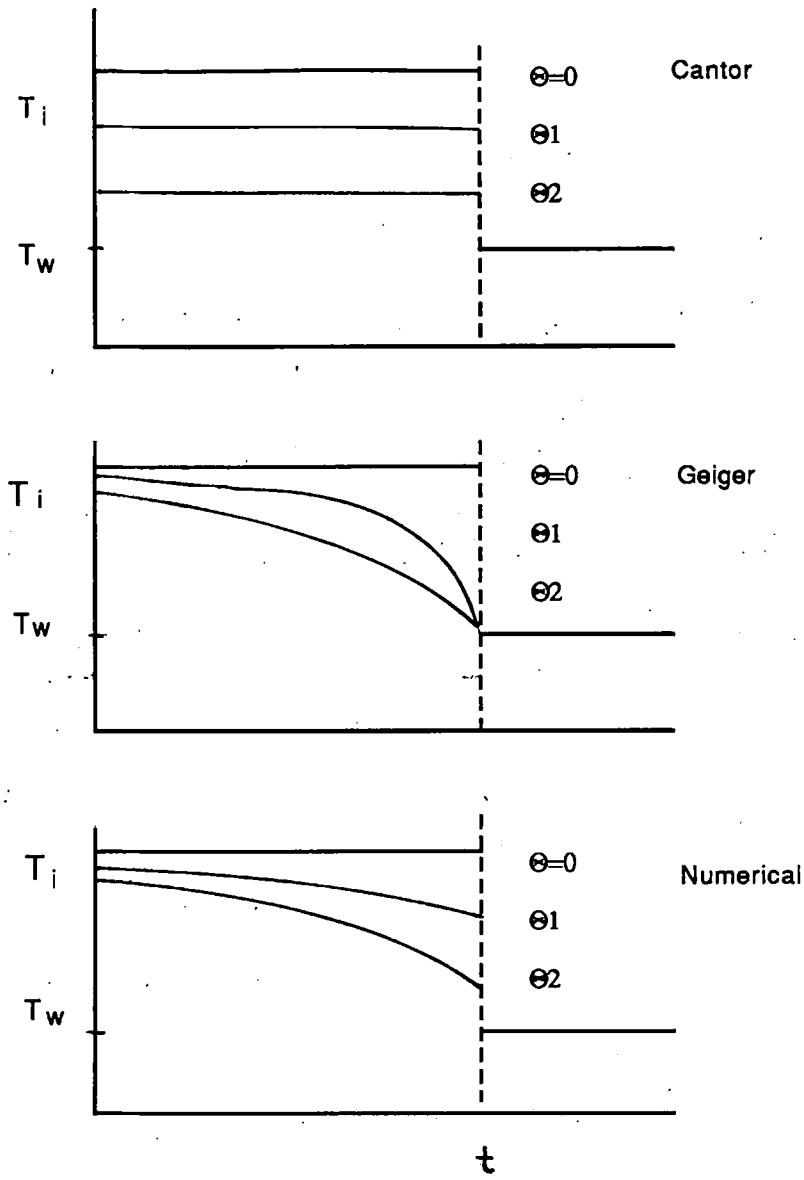

Figure 4.3 Schematic temperature profile through a strip of thickness t and initial temperature T_i, cooling one dimensionally in contact with a perfectly efficient heat sink.

order to achieve accuracy within a reasonable computation time. The mesh points were equally spaced in θ and y. The accuracy of integration time was 0.1×10^{-9} sec.

The latent heat released in solidification can be incorporated in equation 4.9, by replacing the strip specific heat C_p by $C_p + L_f/\triangle T_s$, where L_f is the specific latent heat and $\triangle T_s$ is the solidification temperature range ($\triangle T_s$ for 304 stainless steel is $1508°C - 1425°C$). Unfortunately the solidification temperature range can only be estimated very approximately since many rapidly solidified strips and alloys frequently undercool by several hundred degrees, (Hayzelden, Rayment and Cantor(1983)).

Previous finite difference computer heat flow calculations by Ruhl(1967) and by Hayzelden(1984), indicate relatively little effect of an imperfect heat sink for piston quenching or melt spinning, as long as the heat sink thermal conductivity is greater than the strip conductivity. A series of cooling curves were plotted for Newtonian and non- Newtonian cooling conditions by Bewlay and Cantor(1986). It has been suggested the negative slope of cooling curves became more negative as the wheel speed increases. A non-Newtonian heat flow analysis by Clyne(1983) shows that as the Biot number decreases to less than 0.1 the difference between top and wheel side temperatures is not considerable, (Figure 4.4). The Biot numbers mentioned in Bewlay and Cantor's study are in the range 0.10 and 0.22 for heat transfer coefficients 6 to $21 \times 10^4 Wm^{-2}K^{-1}$ respectively, for wheel speeds in the range 4 to 32 m.s^{-1}. This means the factors which determine the Newtonian or non-Newtonian cooling condition is the Bi number and the heat transfer coefficient. An estimation of possible heat transfer coefficient needed for Cantor's Newtonian and non-Newtonian solutions and numerical models is given in the following text.

3) Heat transfer by convection at strip/wheel interface:

The performance of single and double roller quenching processes on an industrial or laboratory scale often depends on the ability to control the heat transfer at the liquid metal-solid boundaries i.e heat transfer from the liquid strip formed on the wheel to the air or gas boundary layer between

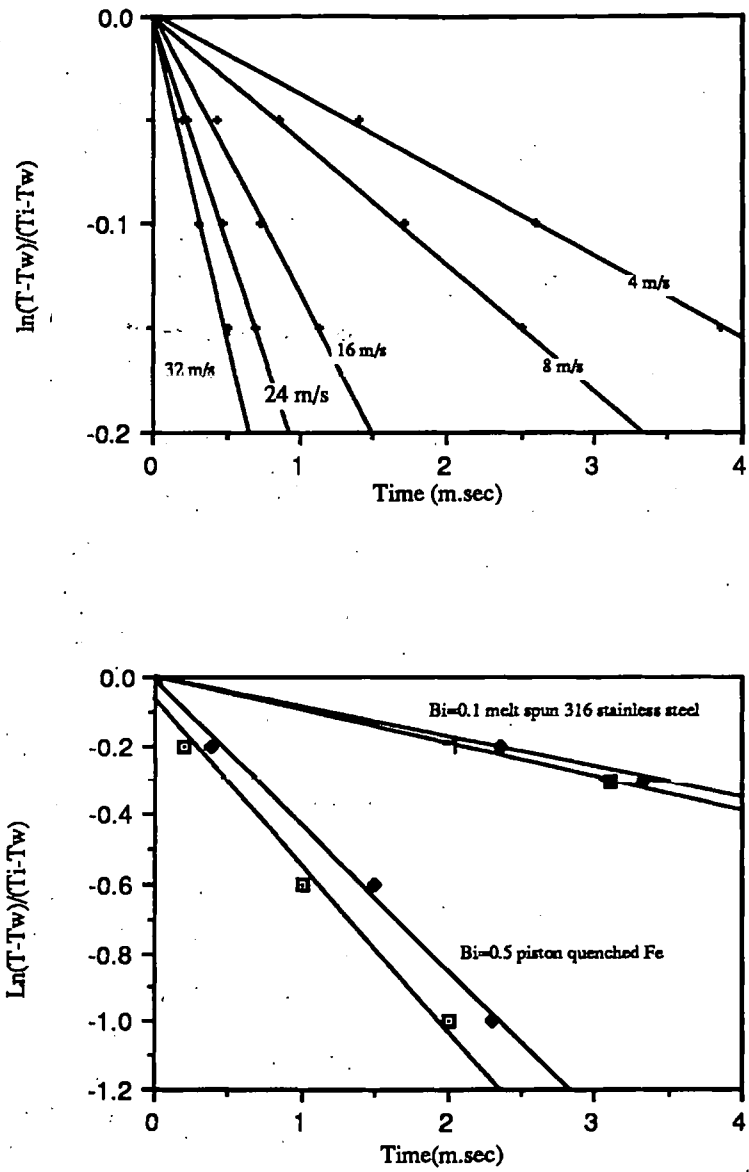

Figure 4.4 Newtonian and non-Newtonian cooling curves for melt spun 316 stainless steel, Bewlay and Cantor(1986).

wheel and strip by convection and heat transfer from this boundary to the chiller(wheel). The thermal contact resistance of these boundaries is determined by the area of true contact between the liquid and the massive solid (wheel). It is generally assumed that any difference between the areas of true and nominal contact arises solely from the presence of gas layers trapped at the interface, Sun(1970).

Contact area analysis of strip:

On a fine scale, high surface tension of the liquid acts to restrict the area of true contact through the formation of micromenisci, Timsit(1982). The experimental results produced by Timsit indicated that the true area of contact may indeed depend on the surface microtopology of the solid and that the liquid conforms faithfully to the solid only when a critical wetting condition is satisfied. The solid is assumed to carry a square array of spherical asperities as illustrated at Figure 4.5(b); The interasperity distance is denoted by d. If the contact pressure is sufficiently low, the liquid makes contact with the solid only at the tip of the asperities and the ratio $f = \frac{\pi\beta^2 \sin\theta}{d}$ of the true (projected) area to the nominal area of contact reduces to

$$f = \left(\frac{\pi}{2}\right) U^2 \beta t \sqrt{\frac{\rho g}{\sigma}} \tag{4.10}$$

where U is a constant, σ and ρ are respectively the surface tension and liquid density, α is capillary length $(=\sqrt{\frac{\rho g}{\sigma}})$. (for mercury α=1.9 mm), $\theta = \sqrt{(2h_{as}/\beta V)}$, where $V = 1 + 2\ln\left(\sqrt{\frac{\sigma}{\rho g 2\beta t}}\right)$, t is the height of liquid metal, h_{as} is asperity height (d is the interasperity distance) and β is the radius of curvature. When the menisci contact the interasperity valleys, each asperity is isolated and f can be written as

$$f = 1 - \frac{2\pi}{tV}\frac{h_{as}}{d^2}\left(2\frac{\sigma}{g\rho} - \beta\right) \tag{4.11}$$

The dependence of f on liquid thickness as evaluated from the last two expressions is illustrated by curves 1 and 2 in Figure 4.5 for values of h_{as}, β and d typical of asperities found on many real surfaces, Greenwood and Williamson(1966) The graph represents the dependence on contact pressure of f at the interface shown in (B).

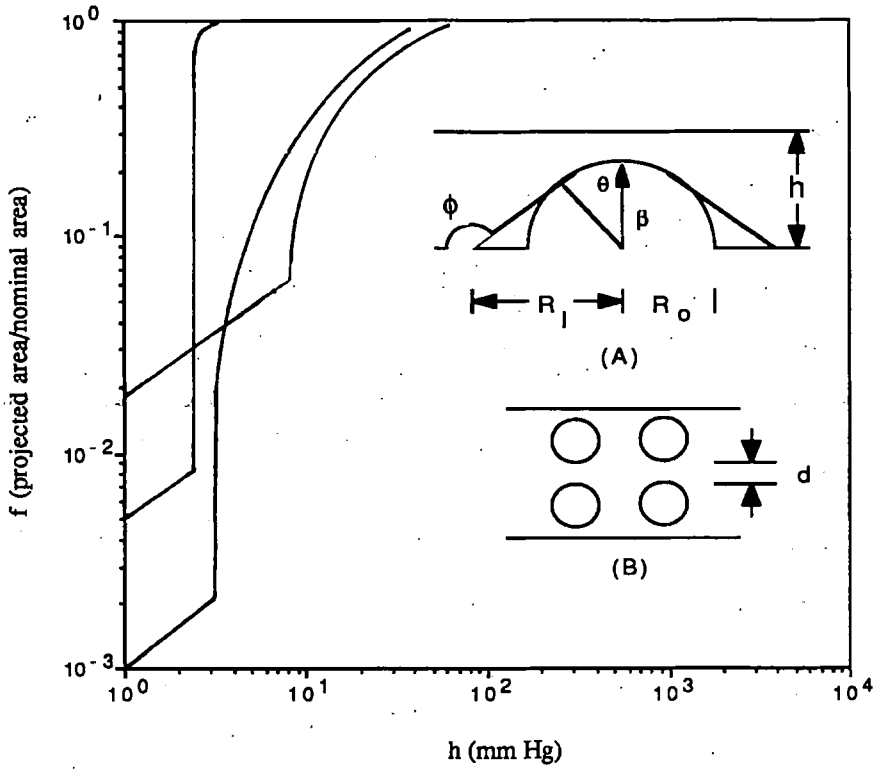

Figure 4.5 The dependence on contact pressure of f at the interface for different h_{as}, β and ϕ 1)h_{as}=1μm, β=10μm, ϕ=180°,2)h_{as}=1μm, β=100μm, ϕ=180° 3)h_{as}=1μm, β=10μm, ϕ=170°,(A) Geometry of a contact meniscus formed with an isolated asperity (B) Multiple asperity contact, Timsit(1981).

1)h_{as}=1μm, β=10μm, ϕ=180°,

2)h_{as}=1μm, β=100μm, ϕ=180°,

3)h_{as}=1μm, β=10μm, ϕ=170°, Timsit(1981).

The effectiveness of adhesion in increasing the area of true contact suggests the existence of a critical contact angle ϕ_c at which the formation of a micromenisci around an isolated asperity is no longer energetically possible and at which the liquid conforms intimately to the solid. Such a contact angle was indeed identified, Timsit(1982);

$$\phi_c = \pi - \arcsin\sqrt{\left(\frac{h_{as}}{2\beta}\right)} \tag{4.12}$$

The contact pattern of a strip cast on the wheel varies markedly with the wheel speed. The size of air pockets or asperities in corporated during casting increases with decreasing wheel speed, Takeshita and Shingu(1986). The mechanical contact between strip and wheel surface can be estimated by calculating the contact area, defined as a percentage of the area f subtracted by an air pocket occupied area to the total area, (Figure 4.6).

Heat transfer coefficient:

It is generally suggested that the heat transfer coefficient increases with increasing wheel speed. The periodic arrangement of air pockets is attributable to fluctuation of the liquid metal puddle residing on the casting wheel surface, Anthony and Cline(1979). The average heat transfer coefficient, h_i, at the metal/wheel interface can be estimated by measuring the relationship between strip thickness t and the time of quenching, θ_R(or residence time), The ordinate intercept t_i of the empirical curve of t versus $\theta_R^{1/2}$ yields the average interfacial heat transfer coefficient h_i according to the relation, Adams(1958).

$$h_i = \frac{-K_s}{1 + (K_s\rho_s Cp_s / K_m\rho_m Cp_m)^{1/2} t_i} \tag{4.13}$$

where K is the thermal conductivity. The subscript s refers to solidified phase and the subscript m refers to wheel material. This definition does not show the effect of wheel speed clearly but obviously t_i will have a smaller

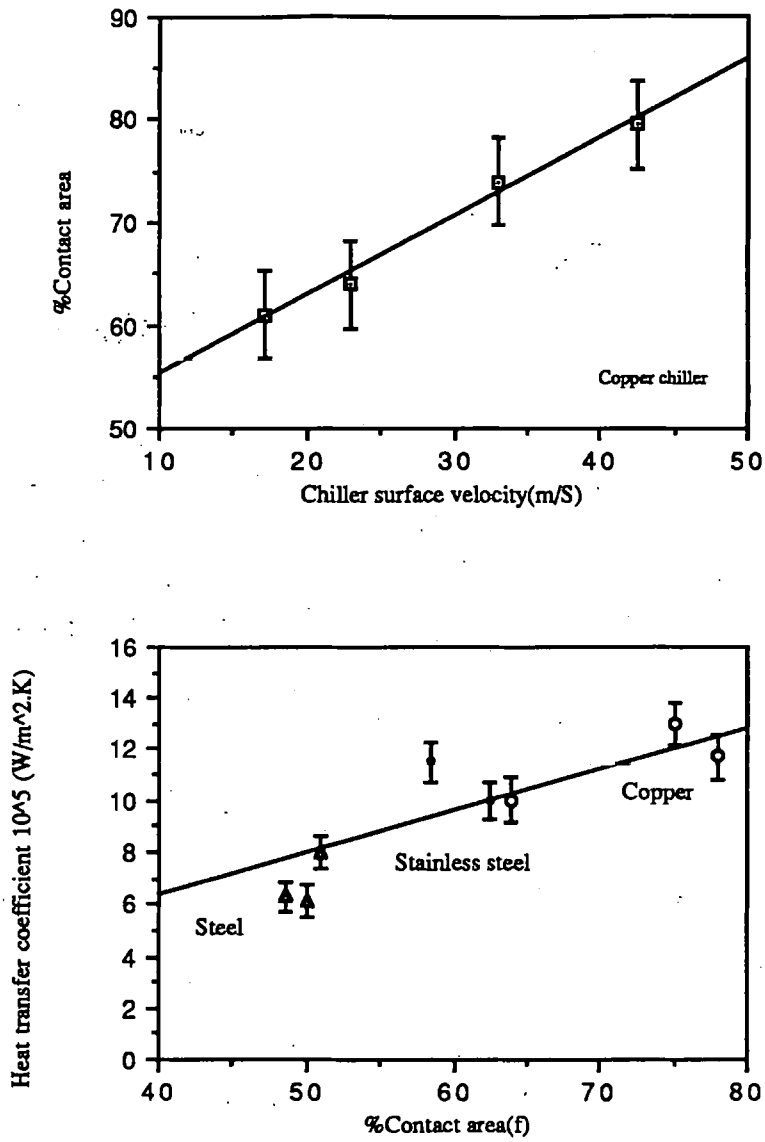

Figure 4.6 Relation between the estimated values of heat transfer coefficient and contact area by Takeshita and Shingu(1986).

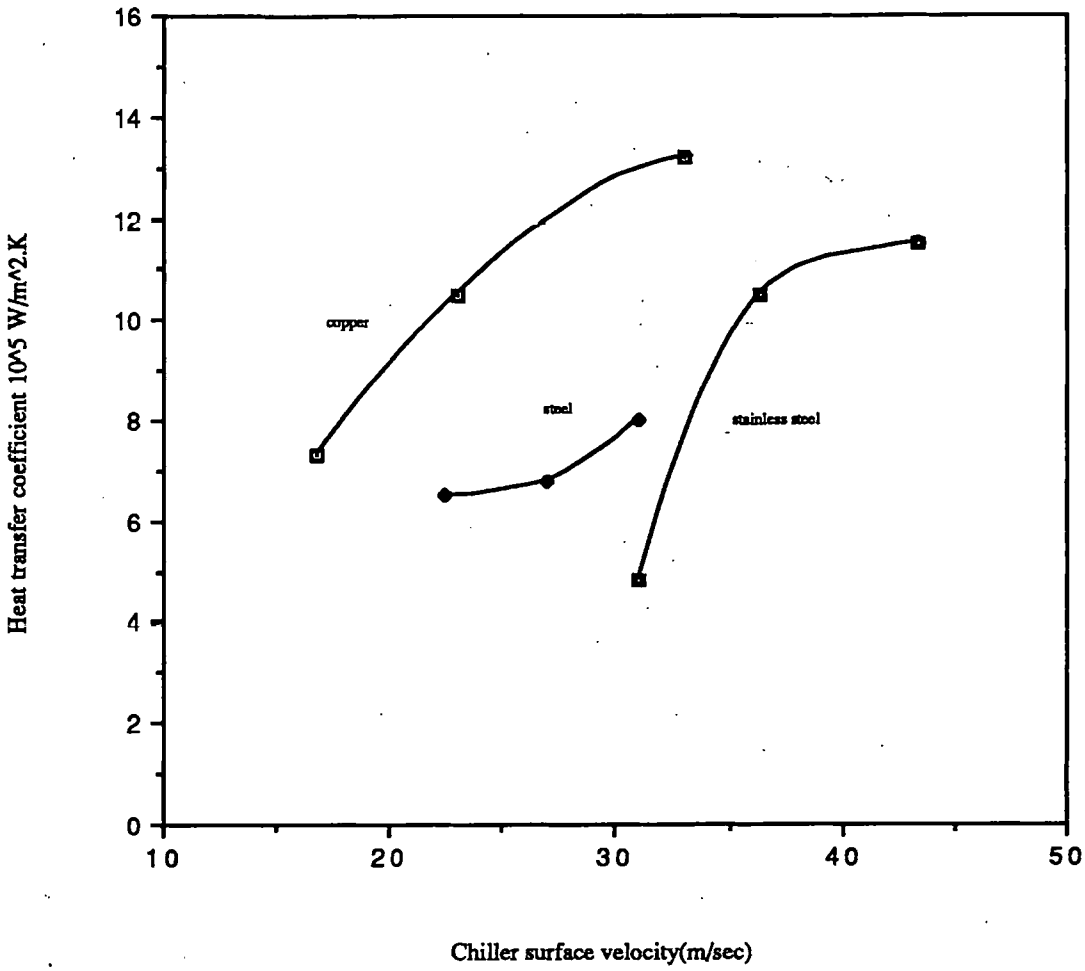

Figure 4.7 The variation of heat transfer coefficient h_i by wheel speed for different wheel materials, Takeshita and Shingu(1986).

value when wheel speed increases as discussed above. The heat transfer coefficients of melt spun Ni-19%P alloy estimated by Takeshita and Shingu(1986) is presented in Figure 4.7. Since in the present research photographic techniques were used to determine the residence distance of strip on the wheel, a new simple heat transfer coefficient h_i is predicted using the fundamental convection heat transfer equation. Assuming the dimensions of residence area as w width and d_{res} length, heat transfer within this area is mostly by convective heat transfer and can be written as

$$Q = h_i (T_{in} - T_w) A = (L_f + Cp\Delta T) \frac{vol \times \rho}{\theta_R} \tag{4.14}$$

therefore, h_i can be defined as :

$$h_i = \frac{(L_f + Cp\Delta T) V_R t \rho}{(T_{in} - T_w) d_{res}} \tag{4.15}$$

where d_{res} is the residence distance, T_{in} is interface temperature, T_w is wheel temperature,w is the width of strip, A is the residence area($d_{res} \times w$), vol is the volume of strip within the residence distance, ρ is density, ΔT is latent heat, Cp is specific heat of the melt. A more accurate value of T_{in} will determine the value of h_i. In the chapter 10 total heat flow equation will be evaluated by an iterative method to approach a balance in heat equation and a reasonable T_s value.

4) Convective cooling of free surface:

Heat transfer at the free surface Q_f consists of radiation heat flow Q_r and natural convection to the surroundings at ambient temperature .

$$Q_f = Q_r + 1.24 (T_t - T_a)^{1.33} \tag{4.16}$$

The second term of this equation is based on an empirical relationship for natural convection for turbulent flow over vertical plates, Perry and Chilton(1973) where T_t is the top surface temperature of the strip and T_a is the ambient temperature.

4.3 The Overall Heat Balance during Melt Overflow

The total enthalpy difference of superheated liquid 18Cr-8Ni stainless steel alloy over the melt overflow lip can be written mathematically in the following form

$$Q_T = M_n(Q_1 + Q_2 + Q_3) \tag{4.17}$$

$$Q_1 = \int_{1508}^{1674} CpFe(\gamma)\,dT + \triangle H_{\gamma\rightarrow\delta} \tag{4.18}$$

$$Q_2 = \int_{1674}^{1808} CpFe(\delta)\,dT + \triangle H_m \tag{4.19}$$

$$Q_3 = \int_{1808}^{1873} CpFe(l)\,dT \tag{4.20}$$

where T_l is the casting temperature and M_n is the number of moles flow within the residence time interval and the specific heats of the various phases at different temperatures are given by Gaskell (1975);

C_p,Fe(γ)=24.34+11.54$\times 10^{-3}T$ Joules /K.mole for temperature range 373°K to 1181°K.

C_p,Fe(γ)=7.69+19.47$\times 10^{-3}T$ Joules /K.mole in the temperature range 1181 °K to 1674 °K.

C_p,Fe(δ)=43.89 Joules /K.mole in the range 1674 °K to 1808 °K.

C_p,Fe(l)=41.80 Joules /K.mole in the range 1808 °K to 1873°K.

Latent heat of solidification($\triangle H_m$)=16239.3 Joules/mole.

M_n can be calculated by multiplying M_r the mole flow rate by the residence time θ_R. M_r can be calculated from the following equation

$$M_r(mole flow rate) = \frac{weight\ \ of\ \ strip/M.W}{length\ \ of\ \ strip/V_R}$$

where M.W. is molecular weight and V_R is the wheel speed. The total heat transfer after the strip reaches its final thickness in the mushy state can be equated to the total heat Q_T

$$Q_T = Q_F + Q_C + Q_H \tag{4.21}$$

where Q_C is the heat transfer by conduction through the thickness of strip, Q_H is the heat transfer by convection at wheel/strip interface(which is the most dominant term in the equation), and Q_F is the heat transfer by radiation and natural convection at the free surface during the residence time interval. The heat transfer after the strip takes off the wheel is by radiation and convection. At this stage, solidification is believed to be completed and thermal stresses originating from solidification shrinkage are generated at the end of the residence zone which creates inverse thermal gradients through the width.

4.4 Gas Boundary Layer Flow

The principle used to explain the occurence of serrated edges and some surface degradation in glassy alloy strip under certain conditions is based on simple boundary layer theory, Schlichting(1968). A thin boundary layer in which the gas molecules essentially move with the same velocity as the substrate surface is established because of viscous drag forces between the substrate surface and adjacent gas molecules. The nature of this thin gas boundary layer and its interaction with the alloy melt puddle (from which alloy strip is continuously drawn) determines whether or not serrated strip edges and surface degradation will occur under a given set of casting conditions. It is assumed that only the very thin gas boundary layer exists immediately adjacent to the substrate molecules the melt puddle width. Smooth edged strip formation has been observed at a gas boundary layer with a Reynolds number Re less than some critical value Re_{cr}. Gas turbulence occuring in the vicinity of the melt pool at $Re > Re_{cr}$ is a mechanism for kinetic energy dissipation and results in the formation of serrated-edged strip. The disturbance created in the liquid pool and strip causes Kelvin-Helmholtz instability. A value Re_{cr} =2000 has been calculated for the critical transition pressures at which strip edges become serrated when casting in He, air and Ar gas, Liebermann(1976). The experimentally defined gas

boundary layer Reynolds number can be given as

$$Re_g = \frac{V_g w}{\mu_g} \tag{4.22}$$

where V_g is gas velocity (assumed equal to substrate surface velocity), w is melt pool width at the contact surface with the substrate (strip width), $\mu_g = \frac{\eta}{\rho}$ =kinematic gas viscosity, η=static gas viscosity, ρ=gas density. Assuming ideal gas behaviour $PV = nRT$ and substituting $V = \frac{nRT}{P}$ into the following gas density equation as

$$\rho = \frac{nM}{V} = \frac{P.M}{RT}$$

Therefore, the Reynold's number of the gas boundary layer interacting with the melt pool may be expressed as

$$Re_g = \left(\frac{V_g w P}{RT}\right)\left(\frac{M}{\eta}\right) \tag{4.23}$$

where P is ambient gas pressure, M is gas molecular weight, T is ambient gas temperature. Note that while the first of the two factors in equation 4.23 relate exclusively to apparatus and processing parameters, the second factor is a physical constant for the gas in which single roller quenching is conducted. Thus the $\frac{M}{\eta}$ values, Weast(1977), given in Figure 4.8 give the propensity for serrated edge formation when using various gases under which strips are cast using fixed processing conditions. Equation 4.22 describes the effect of gas properties which govern the Reynold's number Re_g. The strip edge quality is not only a function of type of surrounding gas but also a function of the flow originates from surface tension and concentration variation on the liquid surface which is called "Marangoni flow", the positive liquid metal pressure within the melt pool, free stream length, surface tension and the amplitude of waves originating from eccentricity of the rotary chiller. In the present study, air was used for the surrounding gas medium and the initiation conditions of edge serrations were studied by varying the other parameters such as liquid metal pressure, flow rate and surface tension.

Gas	He	H_2	Ne	Air	CO	Ar	CO_2	Kr	Xe
10^4 M/η	2.06	2.30	6.49	15.8	16.0	18.1	29.7	34.1	58.1

Order of increasing propensity for serrated strip edge formation

Figure 4.8 Quotient of molecular weight and static viscosity for various gases in which strips can be casted, Weast(1977).

Chapter 5

Survey of Surface Driven Flow

5.1 Introduction

The aim of this chapter is to study the effect of surface tension on alloy and process characteristics considering the interrelated effects of surface tension, alloy composition and temperature. Since the main objective of this work is to achieve uniform strip casting by optimizing the surface tension values of the alloy, it is necessary to know how or whether uniform laminar liquid metal flow during momentum transfer can be achieved and to what extent the surface tension variations affect the final strip characteristics.

The following basic reasons for investigating the surface tension of the alloy are:

1) The first aim is to determine the critical minimum surface tension value for a specific alloy system to produce strip directly from its liquid state. Preliminary studies carried out on Ni-B-Si alloy revealed that some high surface tension values make the initiation of a liquid film in the lip/wheel contact area difficult. Since the oxygen in liquid 304 stainless steel can be controlled by deoxidation agents such as ferrosilicon and surface tension is inversely proportional to the surface concentration of surface active elements, this alloy was chosen for the modelling of melt overflow and the surface tension studies. Sulphur is the second surface active agent which can be added into stainless steel to lower and control it's surface tension.

2) To reveal the composition range of alloys which can be succesfully

used and to determine the possible alloys according to their absolute surface tension values at casting temperatures .

3) To determine the minimum surface tension value which is necessary to prevent instabilities and edge serrations .

4) To understand which surface active element is most effective in reducing and controlling surface tension.

5) To study the importance of melt superheat on the formation of edge serrations and strip characteristics.

5.2 Surface Tension of Liquid

Two principal parameters which influence the surface tension σ_{lv} of a liquid metal are the concentration of surface active elements and temperature, Keene(1983). A knowledge of the influence of these two variables is important in helping to understand how casting instabilities which lead to ragged edged strip can be suppressed so that directly cast strip can be produced with smooth edges. The role of surface tension appears in melt overflow at different stages.

First, the surface tension acts as a physical barrier at the lip/wheel contact point. The process can be run only if the surface tension of the liquid is lower than a critical value, σ_{lv}^{cr}. In this work the critical values σ_{lv}^{cr} for 304 stainless steel and Ni-Si-B alloy with and without Te were investigated.

Secondly, the differences in surface tension along the free surface of liquid metal triggers a fluid flow which is called "Marangoni flow". The fluid may flow from a hot to a cold region or in the opposite direction depending on the temperature coefficient of surface tension of the alloy. Marangoni convective flow occurs at the lip/wheel contact point and in the pouring channel. The aspect ratio of the pouring channel, the nature of Marangoni flow and stirring of the flow by the magnetic field of the induction coil are interrelated.

Thirdly, the fastest growing instability of the pulled out film can be suppressed if the surface tension is higher than another critical value (Chapter

3). Thus edge control of this strip casting process is possible by varying the surface tension. A theoretical description of the shape of the melt pool in melt spinning and other direct strip casting processes shows that the ratio of pool length (l) to width (w) is related to the surface tension of the liquid, (Hillmann and Hilzinger(1984)). The momentum tends to increase l, whereas the surface tension tends to keep l/w=1.

Surface tension is also important on a finer scale. Chapter 3 discussed surface asperities formed on the wheel side of the strip. The nature of these asperities and the number of microweldments per unit area are related to the surface tension of the liquid metal. The expression that relates the activity of species B in an alloy A and surface tension was suggested by Elliott(1981). The reaction for ideal adsorption of species B from the bulk phase onto an unoccupied surface site, s, to form the adsorbed species, B(ads) is

$$B + S = B(ads); \quad K = \frac{\theta_B}{\theta_s . a_s} \tag{5.1}$$

where θ_s is the fraction of active sites not covered

$$\sigma^o - \sigma = RT\Gamma_B^o \ln(1 + Ka_B) \tag{5.2}$$

where σ^o is the surface tension of active sites and σ is the surface tension between liquid and vapour phases. Γ^o is surface excess concentration of species B onto an unoccupied surface site, a_B is the activity of B. Belton(1976) has shown that the surface tension of liquid Fe-C-S melts can be correlated well by equation (5.2), where a_s is the activity of sulphur in the melt. The data produced by Belton are shown in Figure 5.1. It has been reported by Elliot that sulphur is surface active in Fe based alloy systems whereas carbon is not. Belton also showed the surface tension of a number of liquid alloys may be expressed by equation (5.2): (Cu-S, Ag-O, Fe-O, and Fe-S). Turkdogan(1980) has summarized data on the effects of gas species and alloying elements on the surface tensions of liquid iron, copper and aluminum. The data for iron are shown in Figure 5.2.

The Gibbs adsorption isotherm for a constant temperature was given by Allen(1972) in equation 5.3. This equation has been used as a basis for

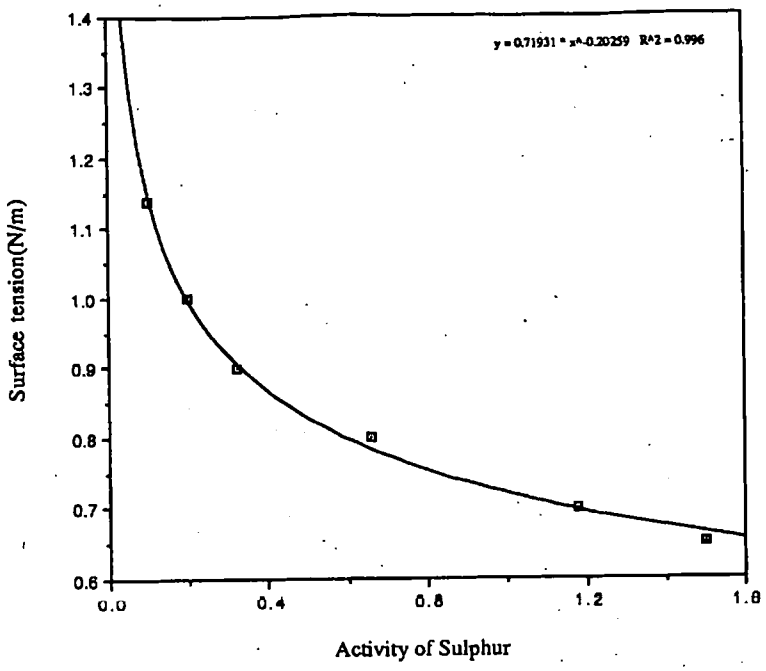

Figure 5.1 Surface Tensions of Liquid Iron alloys containing sulfur at 1450°C, Belton(1976).

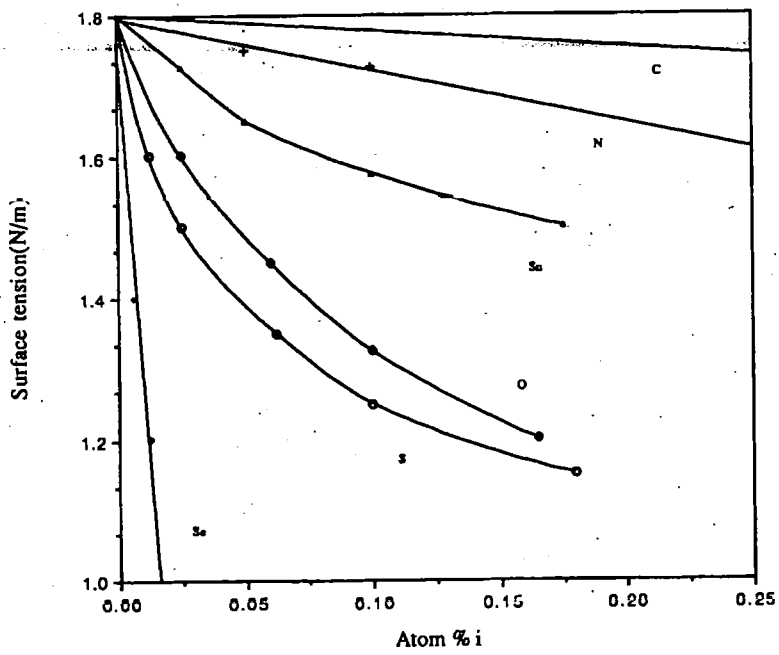

Figure 5.2 Effects of solute species on surface tension of liquid iron at 1550°C, Turkdogan(1980).

interpretation by many investigators studying the effects of surface-active, $\sigma_{LV(2)} < \sigma_{LV(1)}$, additions. The Gibbs adsorption isotherm for a constant temperature was given by Allen(1972) as :

$$-\frac{d\sigma_{LV}}{d\mu_2} = -\frac{d\sigma_{LV}}{RTd(\ln a_2)} = \left[\Gamma_2^0 - (x_2/x_1)\Gamma_1^0\right] \tag{5.3}$$

where a_2 is the solute activity, R is the gas constant, x_1 is the solvent mole fraction and x_2 is the solute mole fraction, T is the temperature, Γ_2^0 is the surface solute concentration. Small nonmetallic additions such as carbon, sulphur, nitrogen, phosphorus and oxygen to iron based alloy cause large reductions in surface tension (Dyson,1963; Halden and Kingery,1955). In the case of oxygen and sulphur, the results have been interpreted in terms of formation of an oxide or sulphide monolayer on the surface. At low concentrations, oxygen is less surface active than sulphur, presumably because of sulphur's larger atomic size and ease of polarization in the presence of iron, Halden and Kingery(1955). It is difficult to obtain measurements of good accuracy of surface tension in multicomponent systems and over a broad enough range of compositions. Therefore, Belton(1972) has derived a relationship for a ternary system such as A(1)-B(2)-C(3). It has been reported by Elliott(1981) that Belton's proposal was successful in predicting the surface tensions of Fe-Cr-C alloys from the work of Walen and coworkers(1962). Since very little data for the interaction coefficients on Fe-Cr-Ni-S system are available, for 304 stainless steel (Fe-Cr-Ni) assumptions were made to calculate the surface excess concentration of sulphur from equation 5.3 considering the system is an iron based alloy.

Surface tension is lowered by surface segregation of surface active elements. The temperature coefficient of surface tension ($d\sigma/dT$) for both iron base ternary alloys and for a stainless steel were found to be positive by Keene(1982) and co-workers.

The temperature coefficient of surface tension of a liquid can be thermodynamically represented by the equation proposed by McLean(1957).

$$-\frac{d\sigma}{dT} = S_o^s + \sum_i \Gamma_i \frac{d\mu_i}{dT} \tag{5.4}$$

where S_o^s is the surface entropy, Γ_i is the surface excess concentration of the i th species in the liquid and μ_i is the corresponding chemical potential of solute. For a binary liquid equation 5.4 becomes

$$-\frac{d\sigma}{dT} = (S_o^s - \Gamma_1 S_1 - \Gamma_2 S_2) + \left(\Gamma_2 - \frac{C}{1-C}\right)\frac{\partial \mu_2}{\partial C}\frac{dC}{dT} \qquad (5.5)$$

The first term in equation 5.5 describes the direct effect of temperature and the second an indirect effect through the influence of temperature on adsorption at the surface layer. The derivative term dC/dT in equation 5.5 represents the change with temperature of the composition due to the change in the degree of adsorption.

5.3 Surface Tension Driven Fluid Flow in Melt pool

In the melt overflow technique liquid metal is displaced over an open channel onto the surface of a rotating chiller. This results in large temperature gradients since the refractory channel wall temperature is about the liquidus temperature while the liquid temperature inside the furnace and within the channel is still comparatively high. Liquid metal is forced and displaced toward the cooler lip and cold rotating wheel surface (which is at about 300 K). These gradients coupled with the additional stirring from the induction coil generate thermocapillary flow and convection in the channel. The fluid flow originating from temperature and surface tension gradients, can be described by the expression:

$$\mu\frac{\partial V}{\partial y} = \frac{\partial \sigma}{\partial x} \qquad (5.6)$$

where x is the direction tangential to the free surface and y is normal to free surface, μ is the absolute or dynamic viscosity and V is velocity. Surface tension gradients γ may be positive or negative depending on the surface active element concentration of the alloy. Keene(1983) reported a positive temperature coefficient of surface tension for Fe-O system and negative for pure iron, Thus:

$$\gamma = \pm\frac{d\sigma}{dT} \qquad (5.7)$$

where T is temperature. The surface tension gradient can be expressed in terms of the temperature gradient and the boundary condition for flow such that:

$$\mu\frac{\partial V}{\partial y} = \pm\gamma\frac{\partial T}{\partial x} \tag{5.8}$$

Normally the surface temperature distribution depends strongly on the flow field originates from surface tension gradient defined by equation 5.7. (Zher, Chen and Mazumder(1988)). In equation 5.6, derivative terms can be assumed as differences and the velocity difference appears after rearranging equation 5.6

$$\mu\frac{V}{y} = \pm\gamma\frac{\partial T}{\partial x} \tag{5.9}$$

$$V = \gamma\frac{\partial T}{\partial x}\frac{y}{\mu} \tag{5.10}$$

The Marangoni number Ma as a ratio of convective heat flow to conductive heat flow.

Convective heat flow=V$\rho c\triangle T$

Conductive heat flow=K$\frac{\partial T}{\partial x}$

The following definition of Marangoni Number can be written as;

$$Ma = \frac{V\rho c\triangle T}{K\frac{\partial T}{\partial x}} \tag{5.11}$$

where $\frac{\rho c}{K} = \frac{1}{\alpha}$ and therefore,

$$Ma = \frac{\gamma\triangle T y}{\alpha\mu} \tag{5.12}$$

In a heat transfer system, the measure of the intensity of convection relative to conduction is described by the Peclet number. The Peclet number(Pe) is based on a thermocapillary reference velocity is the Marangoni number(Ma) which is the basic dimensional parameter of thermocapillary convection:

$$Ma = Pe = \frac{\gamma\triangle T D}{\mu\alpha} \tag{5.13}$$

(where D is liquid pool width and α is heat diffusivity). Typical values of Ma for weld pools are of the order of 10^4 or above, (Zehr, Chen and Mazumder(1988)). Marangoni numbers calculated by using experimental

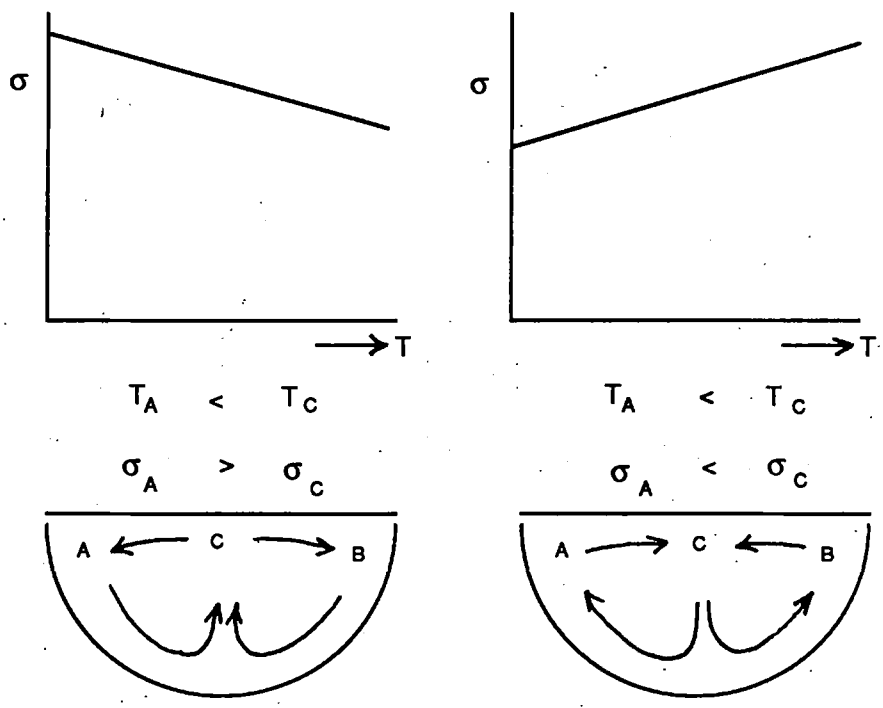

Figure 5.3 Proposed mechanism due to Heiple and Roper(1981) to illustrate the effect of the σ-T curve on the fluid flow pattern.

data for the melt overflow process will be given in chapter 8. The mechanism proposed by Heiple and Roper(1981) explains the effect of the σ-T curve on the fluid flow behaviour of a liquid pool, (Figure 5.4). The flow direction is governed by the surface tension gradient. A positive gradient may drive fluid flow from the furnace wall into hotter liquid. In addition to this phenomenon, flow of liquid metal is induced by displacement within the thermocapillary flow, (Figure 5.3 and 5.4). This interaction may be one of the possible sources of melt pool oscillations. Thermocapillary flow may exist within the furnace anywhere where temperature differences exist. The temperature difference ΔT can be associated with the amount of superheat. The magnitude of the actual thermocapillary velocity V_p can be estimated by;

$$V_p = \frac{\gamma \Delta T}{\mu} \tag{5.14}$$

The fluid flow Q_m originating from the plunger movement can be expressed as a casting velocity (V_c). The cross sectional area of the channel varies as represented in Figure 5.3. The casting velocity increases as the cross section decreases while Q_m remains constant.

The channel width D is another parameter which affects both the temperature difference ΔT and Marangoni convection(thermocapillary flow). Any variation in channel dimension results in different values of V_p and V_c. The interaction between these different flow fields may cause flow parallel or opposed to the main casting direction.

The channel width used in the presented study was 25mm. Details of the process parameters and dimensions of the process are given in the experimental chapter. Surface tension driven flow and pool oscillations originating from fluid interactions described in this section have not been investigated thoroughly so far. It is assumed that the liquid pool in the lip region can absorb the oscillations for modelling purposes. In this research, design and development of the direct casting process consists of planning and control of the alloy chemistry, to reveal the effect of viscosity and surface tension on the pool oscillations and consequent serrations on the solidified strip.

A positive surface tension gradient becomes important when superheated

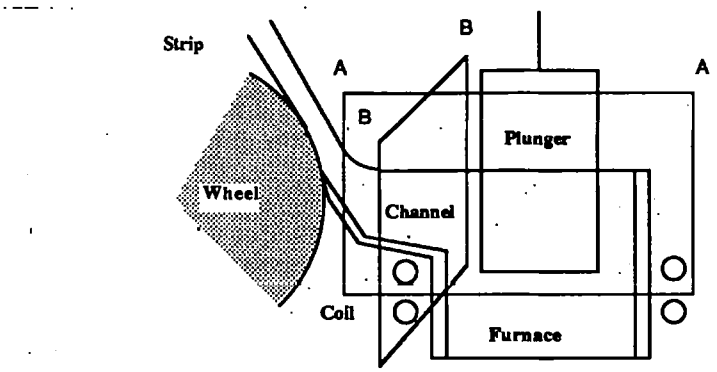

The cross section of meltoverflow furnace

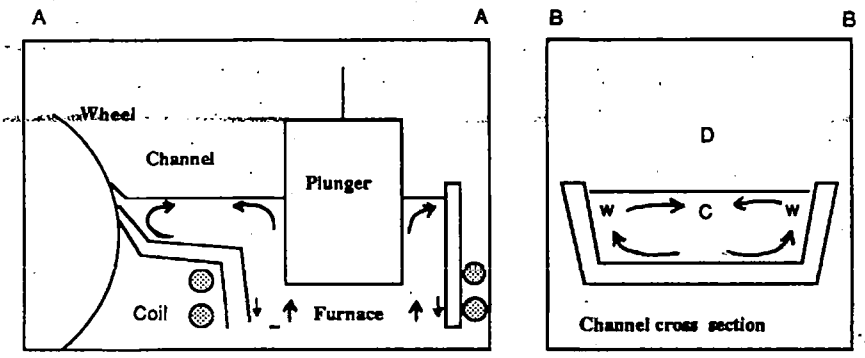

The fluid flow geometry of meltoverflow process

Figure 5.4 The fluid flow geometry of the melt overflow for a positive surface tension gradient.

liquid metal flows toward the rotating chiller since this will result in Marangoni flow. A negative surface tension gradient in the pool/wheel contact area also results in Marangoni flow and most likely promotes a requirement for higher momentum (kinetic energy-m$V^2/2$) to stratify the cooler melt front. High surface tension values may make it impossible to initiate the process. The schematic representation of the melt pool/wheel contact area is given in Figure 5.5. Within the initial contact area A_D the kinetic energy transferred

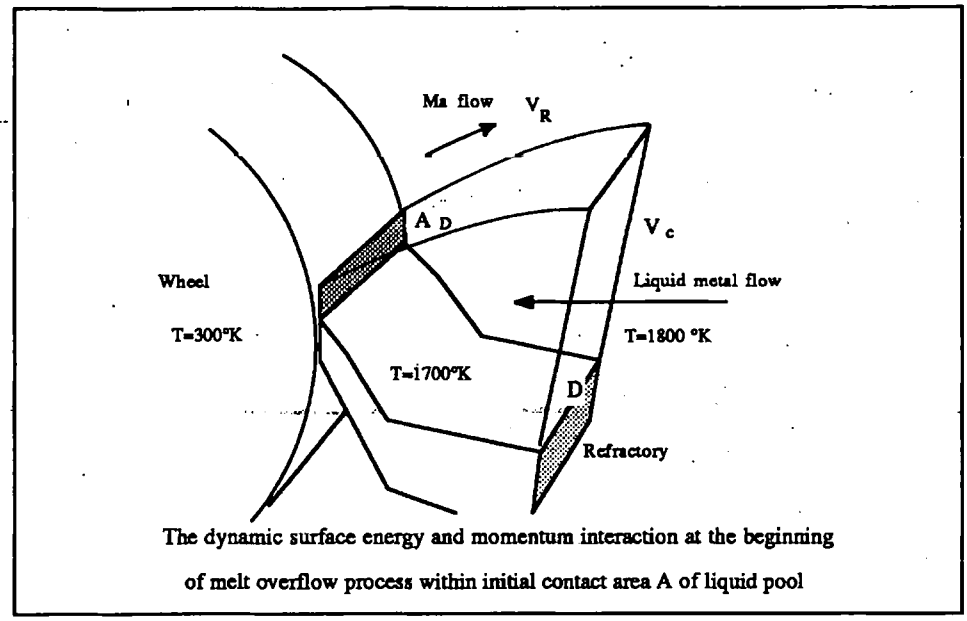

Figure 5.5 Schematic representation of liquid front and momentum transfer of melt overflow.

from the wheel has to be larger than the surface energy of the alloy. As the temperature at the initial contact area increases by heat flow from the furnace the absolute value of the surface tension increases. This can be affected by additions of surface active ingredients which lower the surface energy of the alloy. If the transferred kinetic energy necessary to drag liquid out is larger than the surface energy, a liquid front climbs up the wheel. Ma flow in the opposite direction to momentum transfer can be reduced by heating the liquid charge and refractory material. Since the temperature difference

$\triangle T$ in the equation 5.7 directly controls steady state heat transfer condition in Marangoni flow, it is necessary to keep temperature difference low in flow to maintain laminar continuous flow. This can be done heating the refractory of the pouring channel allowing the superheated liquid to stay in the pouring channel before the strip casting. As the temperature difference between refractory material and liquid flow gets smaller, smooth laminar flow can be achieved by reducing the complex Marangoni convection.

The recirculatory flow is believed to be responsible for the free cast surface roughness that can be found on crystalline or partially amorphous strip, Dantzig(1988). The recirculating liquid breaks loose dendrite tips or even entire crystals from the solidification front redistributing them on the top surface. The recirculation flow in the lip mainly originates from Marangoni convection and turbulent flow. The effect of casting speed and Marangoni convection on cast strip will be discussed in chapter 8. For a complete model it is also necessary to consider gravitation effects on the initiation of convective flow in the lip. A complete solution of the Navier-Stokes equations with heat transfer and surface tension gradient boundary conditions is required and as yet this is not possible.

5.4 Thermocapillary Convection

Liquid convection due to inhomogenities of the interfacial tension in the free liquid surfaces are called Marangoni effects. The inhomogenities of the interfacial tension can be of thermal or chemical origin. They are common phenomena for all liquids with a free surface (interface between liquid and gas or between liquid and liquid). Being surface effects, Marangoni effects have a higher importance in small volumes or near a free surface. Marangoni effects are flow phenomena which are independent of gravity. The investigations of Marangoni effects in a laboratory meets principle difficulties because they are invariably coupled with buoyant convection under normal gravity. Therefore experiments on Marangoni effects under microgravity in space are useful to investigate pure surface tension driven flow. The surface tension

σ_{LV} is temperature dependent. The surface tension of a cold liquid is lower than the surface tension of hot liquid. Therefore, if a temperature gradient exists on the free surface (or free interface) of a liquid, there is also a surface tension gradient in this free surface which drags the surface from hot to cold regions. The surface motion is transferred to liquid layers beneath the surface because of the liquid's viscosity. If the temperature gradient is intentionally and experimentally directed along the free surface, the fluid flow is called thermocapillary flow. The latter case gives rise to the so-called Benard-Marangoni instability with the appearance of hexagonal convection cells when exceeding a critical temperature gradient(Ma number).

The laminar flow state of thermocapillary convection shows a transition to a time dependent (oscillatory) state when exceeding a certain critical Ma number Ma_a^c of the order of 10^4. This has been discovered in simulated floating zone experiments carried out by Schwabe and Scharman(1989). (Liquid cylindrical column with a free cylindrical surface suspended by surface tension forces between two cylindrical rods which are differentially heated to impose an axial temperature gradient along the free surface). Schwabe and co-workers(1989) investigated the effect of gravity on thermocapillary flow. They carried out some experiments under microgravity conditions using n-tetracosane liquid (a transparent liquid without bubbles) with well illuminated tracer particles. The liquid was exposed to a temperature difference. Heaters were situated on each side of the liquid. Up to the temperature difference of ΔT=55°C, they couldn't observed any motion of the tracers from hot to cold in the free surface. But for ΔT=60°C, they reported that there was strong motion in the expected direction.

To explain this suppression of Marangoni convection for smaller Marangoni numbers. Schwabe and co-workers(1989) reported that their test liquid n-tetracosane was not clean and dirt on the free surface acted like a solid layer. This skin suppressed thermocapillary flow only for the temperature difference of ΔT=55°C. At higher temperature difference this solid skin ruptured, thermocapillary flow could start. The flow very near the hot wall and very near the cold wall circulating along the bottom of the cuvette is

due to buoyancy forces(thermal convection).

Liquid metals, particularly high temperature such as $1500°C$ or above it is extremely difficult to observe. There are very few publicated data. Heiple and Roper(1982) have followed fluid flow patterns originating from surface tension difference on traveling welds on stainless steel by observing the weld surface with high speed motion pictures. They observed coalescence of aluminum oxide particles on the surface.

In this research, thermocapillary flow was not investigated directly, but its subsequent effect on the solidifiying strip, the effect of alloy composition and deoxidation on the final product quality were investigated. Since pyrometallurgical properties of liquid metals are complicated, it is useful to utilize the model developed for n-tetracosane and Schwabe's(1989) results to explain surface tension driven fluid flow phenomenon.

Chapter 6

Experimental Procedure

6.1 Introduction

The main objective of this work was to investigate the production of a number of alloys (permalloy superC, iron-chromium-aluminium, nickel base metglass and as a test material 304 stainless steel)as strip, by displacing the liquid charge over a pouring channel onto a water cooled wheel. This study is based on a laboratory scale direct strip casting unit. The work was performed in different stages;

1) A mini induction furnace was designed and constructed by using information obtained experimentally. Some technical information was obtained from 'Inductotherm Generator Company' about the coil dimensions and number of turns necessary for efficient heating and melting.

2) A special crucible with a spout was developed. The pouring channel geometry was determined considering minimum heat loss and maximum mass and heat transfer criteria. The crucible material was an alumina base ceramic and a number of different alumina refractory compositions were used. The main objective was to achieve maximum spalling resistance and performance under a high thermal gradient condition such as dT/dy=210 $^{\circ}C$/mm.

3) A series of stainless steel 304 alloys with different surface active elements were used as test materials to investigate the effect of process and material parameters on the final strip dimensions and microstructures.

4) A silica base slag was used to reduce heat losses and to control alloy composition and sulphur concentration. Since stainless steel alloy was chosen as the test material, silica based slag was used to minimize chromium losses.

5) The wheel speed and lip/wheel contact angle α were fixed after some preliminary experiments. (Wheel speed=2.780 m/sec and $\alpha = 38°$ from horizontal). For modelling experiments, the plunger speed was also kept constant at 3.705 mm/sec.

6) The sheets produced were examined with an optical microscope, scanning and a transmission electron microscope.

7) Samples of alloys produced were prepared in 0.85-1.00 g pellets mass for surface tension measurements by the modified oscillation droplet technique. These measurements were carried out under a helium (99.9% pure) atmosphere.

6.2 Laboratory Induction Furnace Development for Melt Overflow

The coreless induction furnace was made from an 8 turn coil (60 mm height and 110 mm in diameter). The joule heating power was 15 kW and frequency of induction field was 9600 Hz. The furnace melting capacity was 5 kg of stainless steel. This could be melted in 45 minutes. The coil was insulated with a kaolin wool material (6 mm) thick and the inner surface was covered with a tubular alumina material. The furnace body was made from an aluminium frame and sandanyo side and base panels. The furnace was designed to rotate in three axes. The tilting of the furnace in an x-z direction was achieved by installing the furnace into a Y-shape alloy steel frame which is able to rotate in the x-y plane while the furnace can rotate in the x-z plane. This can enable us to adjust the gap between the wheel and lip precisely. The bottom of furnace was made from alumina brick and the space between the coil and the alumina brick was filled with spinel material (MgO, Al_2O_3) in granular form. This insulation technique was used to provide even and steady heat distribution in the crucible. A clay bonded graphite crucible

which can reduces induced field strengths was used to back the isostatically pressed and sintered crucible. The inner crucible which has a spout was installed into the graphite crucible, ramming a spinel powder or mouldable alumina material between them. The final susceptor assembly can be seen in Figure 6.1. The graphite/sillimanite crucible was placed in the induction

Figure 6.1 Isostatically pressed sillimanite crucible(right) and on the left as installed in clay bonded graphite crucible with phosphate bonded alumina plunger(front).

coil of the furnace and the furnace was positioned to set a 38° lip/wheel contact angle. This can be seen in Figure 6.2. The crucibles installed with phosphate bonded alumina backing material were dried at 98°C for 5 hrs and sintered at 900°C for 2 hrs. The gap between pouring channel and the top turn of the coil was 80 mm. A number of preliminary tests were made to determine the optimum channel to coil distance in view of importance of induction heating and heat transfer around the pouring channel. A thermal insulation in 6mm thick kaolin wool backed with mouldable alumina was filled in the gap between pouring channel and coil.

Figure 6.2 The melt overflow furnace positioned at 38° angle to the wheel.

6.3 Crucibles and Plunger Materials

The crucibles and plungers were made from alumina based ceramic materials.

Three different types of crucibles were made:

1) Phosphate bonded crucibles moulded in a silicon rubber mould, dried at 98°C 5hrs and sintered at 1000°C 2hrs. The composition of mouldable alumina material was $SiO_2 = 4.5, Al_2O_3 = 91, Fe_2O_3 = 0.4, TiO = 0.1, CaO = 0.1, MgO = 0.2, P_2O_5 = 3.0, NaO = 0.3(wt\%)$

2) Isostatically pressed and sintered alumina crucibles. The working temperature of these crucibles is $1700°C$ and thermal shock resistance is not as good as sillimanite crucibles.

3) Isostatically pressed and sintered sillimanite crucibles reinforced by phosphate bonded alumina lining. The composition of sillimanite crucibles is $CaO = 0.15, Al_2O_3 = 6, Fe_2O_3 = 0.95, Na_2O = 1, TiO_2 = 0.07(wt\%)$ This material has good thermal shock resistance and a maximum working

temperature is 1600°C. The isostatically pressed crucibles were manufactured by Magna Industries L.t.d.

6.4 Alloy Preparation

A 304 stainless steel alloy which has a nominal composition of weight (%); C:0.08max, Mn:2.0max, Si:1.0max, P:0.04max, S:0.03max, Cr:18.0/20.0, Ni:8.0/11.0 was melted in a mini induction furnace in air. Deoxidation of melt was done by the addition of FeSi(grade 70%), FeMn(grade 86%) and Al. After deoxidation, FeS(grade 25%) was added to lower the surface tension of the alloy.

In the present experimental work at some heats the melt was deoxidized with Al first and FeSi was added later. Although deoxidation power of Si is greater than Mn and Al, FeSi deoxidation may decrease viscosity because silicon reduces the viscosity of steel. FeMn deoxidation followed by Al addition was also carried out at different heats. Based upon a preferential nucleation theory it was reported by Cherukuru(1979) that the stainless steel melts should be deoxidized first by aluminium to create favorable nucleation conditions and later on by silico-manganese or ferrosilicon to produce liquid silicate inclusions which coalesce very easily and float out the melt. Based upon laboratory and also industrial experiments Itiro et al(1970) reported that deoxidation of 304 stainless steel by silico-manganese and aluminium is much more powerful and effective than silico-manganese alone. The percentage of deoxidizers added to the melts for each experiments are given in the Appendix (alloy specification pages). A siliceous granular slag coagulant for which the chemical analysis is given as: SiO_2 : 75.0, Al_2O_3 : 12.0, TiO_2 : 0.30, Fe_2O_3 : 0.30, CaO : 1.00, MgO : 3.7, K_2O : 2.50$wt\%$ was used to form viscous slag on the top because of the following reasons:

1-to reduce heat losses from the free melt surface, especially radiated heat,

2-to reduce the effect of Marangoni flow,

3-to keep chromium losses from liquid stainless steel low,

4-to prevent small inclusions entering the melt pool.

Liquid or solid inclusions may attach to the slag site more easily then when the liquid metal delivery is without viscous slag on the top.

6.5 Specimen Preparation for Microexamination

Metallographic examination was performed on polished and etched surfaces. Sheets were sectioned along their width in through section and embedded into conductive bakelite. After fine polishing with 1 micron diamond paste ,stainless steel strip samples were etched with acidic ferric chloride (0.5g $FeCl_3$, 3.75ml HCl, 156ml H_2O) for about 1.5 minutes.

The transmission electron microscope specimens were prepared by punching 3mm diameter disc samples from strip previously ground with 400, 600 and 1200 mesh abrasive paper and polished with 1 micron diamond paste. The discs were polished in a jet polishing device using an electrolyte of composition; 120ml perchloric acid, 240ml glycerol and 840ml methanol. The best jet polishing conditions to achieve a large dimple radius and large area were found to be voltage=50 volt, flow rate=4, electrolyte temperature=4°C, current is variable.

6.6 Temperature Measurements

The degree of melt superheat was measured by an Icron two colour optical pyrometer attached to a Philips strip chart recorder. The pyrometer lens was positioned above the liquid metal delivery point and focused on the liquid melt pool/wheel contact area. The temperature of the liquid pool were recorded against time on a chart recorder operating at 30mm/min.

6.7 Colour Photography of Melt Overflow

An Olympus OM2N single lens reflex camera with a motor drive attached was used to photograph the melt overflow strips solidifiying on the chiller. 100 ASA daylight colour film was exposed at a rate of 1 frame/sec. The

camera lens aperture settings were fixed after preliminary experiments at f5.6. The exposure time of 10^{-3} sec was determined by photometer. Since the wheel rotating speed at 2.7 m/s would move 2.7 mm in 10^{-3} sec, the photographs virtually freeze the motion of strip on the wheel.

To minimize processing errors, the same roll of film was been used to record each melt overflow run. By placing the densitometer aperture on a colour negative, the colour density was measured at the melt pool and at various points along the length of the strip. The temperatures of the melt pools were measured by an optical pyrometry and plotted as x-axis against the corresponding colour densities as y-axis. The graph is given in Appendix.

6.8 Film Colour Density Measurement

The colour film negatives were scanned by a Melico colour photodensitometer which can measure red, blue, green and white colour densities. The instrument was used to measure the amount of red light being transmitted through a 1mm diameter aperture placed on the colour negative film. The variation of colour density against temperature is reported as almost linear for red light(wavelength 620- 700nm), Gillen and Cantor(1985). The calibration results of this work showed that It is more sensitive to temperature variations.

6.9 Image Processing of Colour Photographs

The colour photographs of each melt overflow experiment were analyzed by a photogrammetrical study, using a system of image processing at Earth Science Faculty, Image Analysis Laboratory of the O.U.

6.10 Surface Tension Measurements

Surface tensions of 304 stainless alloy used in the melt overflow experiments were measured by a Modified Oscillating Droplet(MOD) technique. This

technique was originally developed by Lu(1975) and his co-workers, and differs from conventional methods which are used to measure surface tension such as 'pendant drop' in which liquid metal/ceramic interaction is involved. It is a dynamic method based on oscillations of a levitated droplet by an alternating magnetic field under an inert atmosphere. Problems associated with liquid contamination from the specimen holder (probably ceramic) are thereby avoided. The apparatus available for the current work was developed as part of an associated programme, Grant, Cummings, Wood and Blackburn(1988). Theory of surface tension measurements by oscillating droplet technique are given in Appendix.

6.10.1 Experimental

MOD experiments were performed under helium atmosphere. The levitating magnetic field was generated by a 15kW induction heating generator which has a frequency of 450kHz. The samples (0.9-1g) are loaded in a tower system of ceramic cups just in the centre axis of levitation coil. The chamber was pumped down to less than 10^{-1}Pa and backfilled to 5×10^{4}Pa research grade helium purified by a titanium, copper oxide and molecular sieve purification train. The sample is heated by eddy currents driven by the induction field. When the sample was molten, the droplet temperature could be controlled either by adjusting the power to the coil, or by passing gas over the sample using four diametrically opposed 'blowers' in the xy plane.

The image of the oscillating molten droplet is transferred through a zoom lens(80-200mm) onto the grids which is a rectangular window on the photoresistive diod. A single observed from top, provides information on the Σ and Δ bands, i.e the Π band is suppressed from top view. From the side a double slit which has two rectangular grids intersect each other at 45 degree observed the three bands. Theoretically with the two detector orientations, slit geometries and relative intensities of the peaks, it should be possible to correctly identify the three bands and obtain w_R and hence the surface tension. The amplified signals come from top and side detectors are digitized

then saved on a data and computer where a discrete fourier transformation was performed. A minimum of two minutes was allowed for stabilization before 1024 samples at 400 samples per second were simultaneously taken for three channels(two detectors and an optical pyrometer). Figure 6.3 represents the schematic diagram of the set up of modified oscillation droplet technique.

The frequency spectra after fourier transformation appears as in Figure 6.4. The figure shows the two spectra obtained from both side and top detectors as superimposed peaks at different frequencies. Deduced surface tension values are given in this text and are used to predict thickness and instability conditions for melt overflow. The results are given in next chapter.

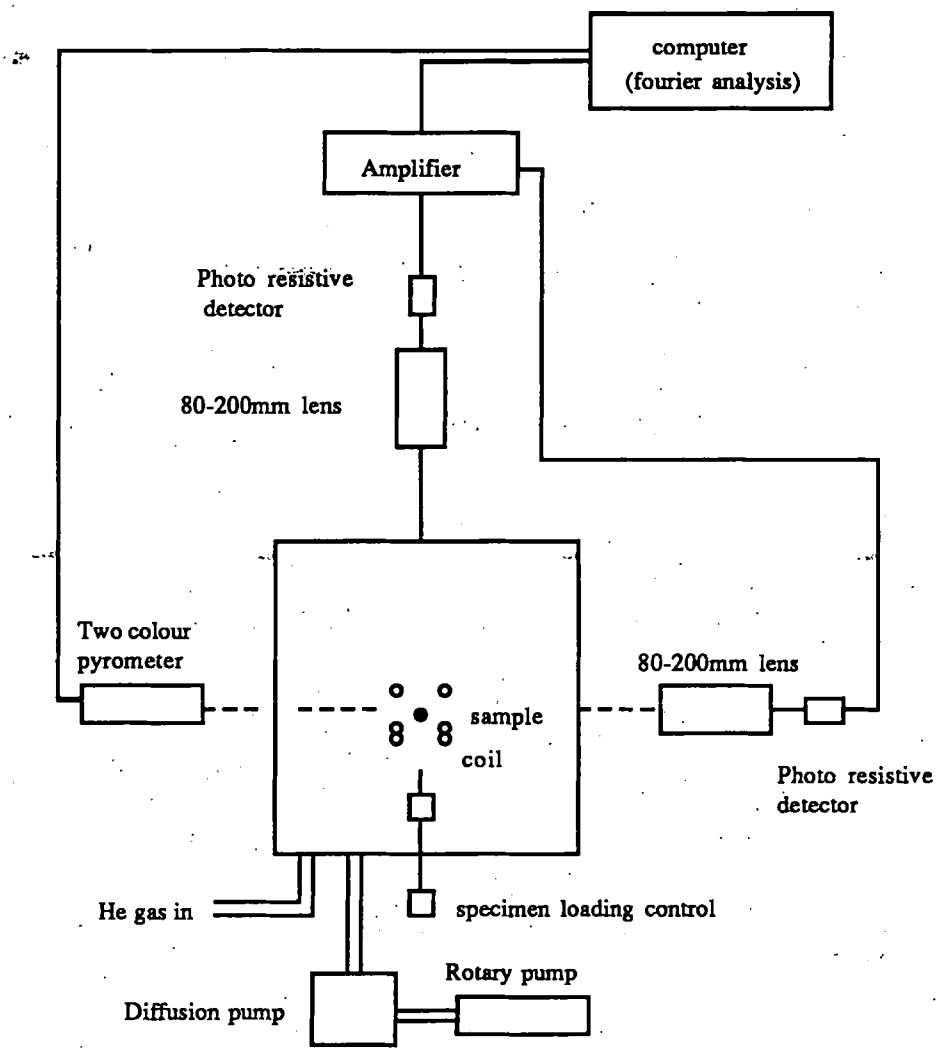

Figure 6.3 The schematic diagram of the apparatus to determine the surface tensions of molten metal droplet by oscillating droplet technique.

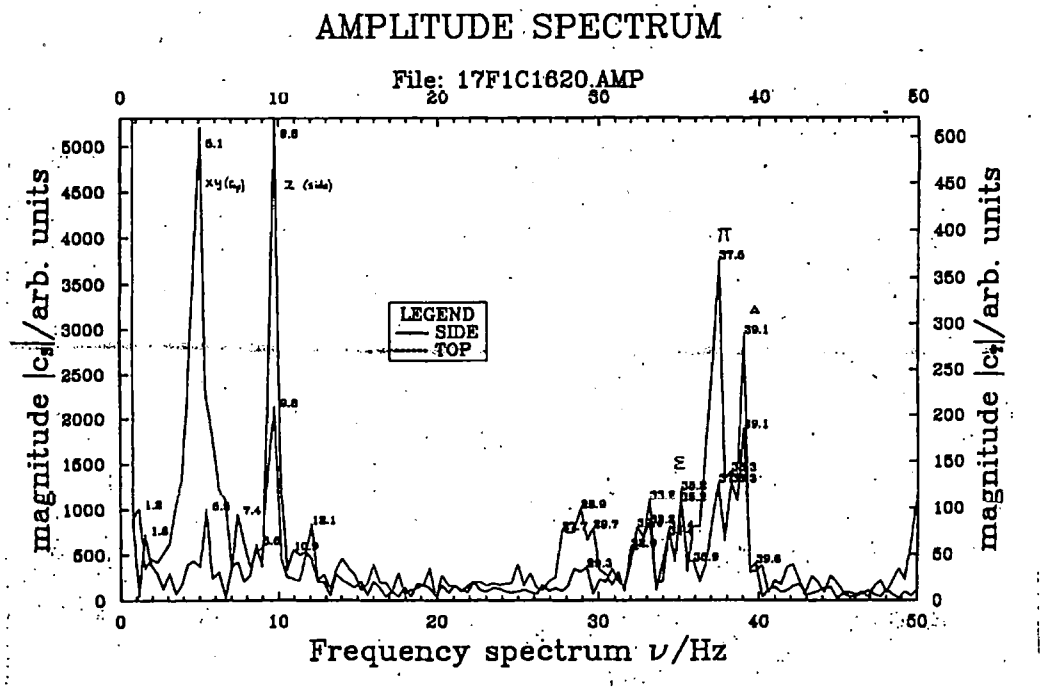

Figure 6.4 The frequency spectra of fourier transformation of oscillation data collected from side and top detectors.

Chapter 7

Results and Discussions about Surface Tension Measurements

7.1 Concentration Dependence

A series of 304 stainless steel alloys which contain different sulphur and oxygen contents were investigated to observe the effect of surface active elements on the surface tension of the molten alloy. The results of surface tension measurements revealed that sulphur can markedly reduces the surface tension, particularly in the concentration range 0.01-0.1 wt $\%S$ when σ_{LV} values reduce to 2.2 Nm^{-1} from 1.4 Nm^{-1}. Figure 7.1 shows the variation of surface tension of 304 stainless steel alloys against %Sulphur at temperatures 1500°C and 1700°C. This figure shows that increasing the temperature increases the surface tension probably by the desorption at the liquid/gas interface. The mass transport rate in the molten levitated sample controls the sulphur evaporation rate on the surface. Consistency and similarity between Figure 7.1 presented in this chapter and Figure 5.1 suggested by Belton(1976) and shown in chapter 5, indicates that the surface tension of iron based alloys(including 304 stainless steel) varies exponentially with the concentration of sulphur. Experimental results of surface tension measurements carried out by using different sulphur contents have been analyzed to derive a relationship between surface tension and sulphur content. Curve fitting was undertaken, the general equation which governs the experimental

data is

$$\sigma_{LV} = C_1 (\%S)^{-n} \tag{7.1}$$

where C_1 and n are constants for a given temperature. The numerical values of the constants of the curve fittings are given in Table 7.1.

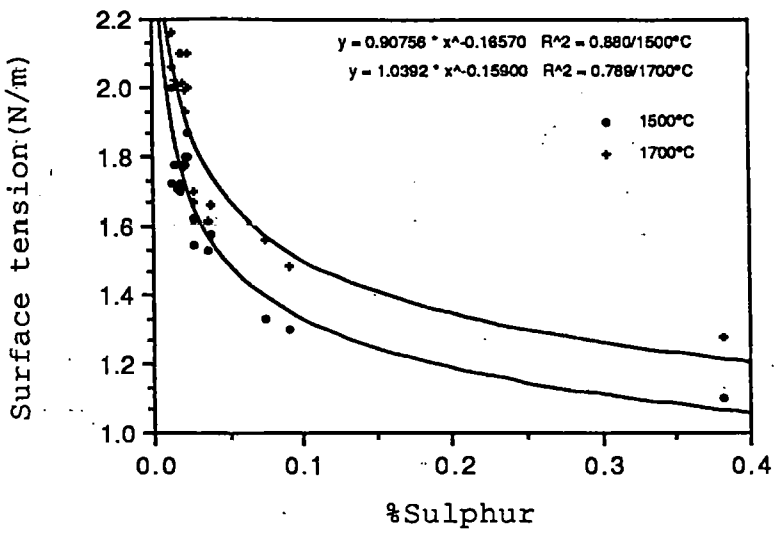

Figure 7.1 The effect of temperature and sulphur on surface tension of 304 stainless steel.

Equation 5.3 has been used as a basis for interpretation by many investigators studying the effects of surface active elements, $\sigma_{LV(2)} \leq \sigma_{LV(1)}$, additions, Allen(1972). As shown in Figure 5.2 small nonmetallic additions to liquid iron cause large reductions in surface tension, (Halden;1955, Kozakevich;1961, Tsarevskii;1960, Dyson;1963 and Turkdogan;1980) Assuming Henry's law holds mole fraction for solute activity a_2 in equation 5.3 can be substituted for the solute mole fraction x_2=0. Surface solute concentration Γ_2^0 from equation 5.3 can be calculated from the plot of surface tension against ln(%S). When σ_{LV} is plotted against ln %S, the slope is equal to C_3 and this corresponds $\Delta\sigma_{LV}/\Delta(\ln a_2)$ in equation 5.3. Therefore, the equation obtained by the regression analysis of the surface tension measurements

of 304 stainless steel was given in the following form:

$$\sigma_{LV} = C_2 - C_3 \ln \%S \tag{7.2}$$

where C_2 and C_3 are constants at a specific temperature. Surface excess can be calculated substituting C_3 values in equation 5.3. The values of these constants and surface excess of sulphur in 304 stainless steel alloys used were given in Table 7.2. The results of surface excess sulphur concentrations calculated showed small variation with temperature, (Figure 7.2).

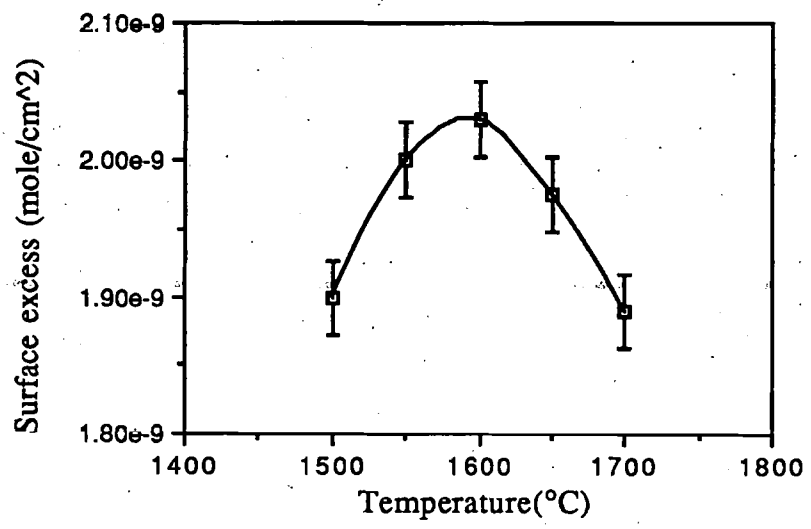

Figure 7.2 Surface excess concentration of sulphur above liquidus temperature.

7.2 Temperature dependence

The variation of surface tension of 304 stainless steel at high temperatures for different oxygen and sulphur contents are presented in Figure 7.3. This figure shows how the interrelation between solute concentration effects the surface tension and temperature coefficients of surface tensions. The constants and

C	a	Temperature °C
0.907	0.166	1500
0.915	0.171	1550
0.944	0.170	1600
0.982	0.167	1650
1.039	0.160	1700

Table 7.1 The curve fit constants of surface tension against sulphur content at high temperatures of 304 stainless steel.

C_2	C_3	Surface excess mole/cm^2	Temperature °C
0.784	0.244	$19.0 * 10^{-10}$	1500
0.784	0.257	$20.0 * 10^{-10}$	1550
0.789	0.270	$20.3 * 10^{-10}$	1600
0.838	0.271	$19.7 * 10^{-10}$	1650
0.894	0.268	$18.9 * 10^{-10}$	1700

Table 7.2 Surface excess sulphur concentrations of 304 stainless steel.

slopes of the linear plots of the surface tensions can be described as

$$\sigma_{LV} = d + \frac{\partial \sigma}{\partial T} T \tag{7.3}$$

where d is a constant. Surface tension values are plotted against temperature for different surface active element concentrations in Figure 7.3 and given as Table 7.3. This table shows the surface active solute concentrations and the temperature coefficients of surface tension. Figure 7.3 and Table 7.3 showed that the alloy with the lowest surface active solute concentration (O=158ppm, S=150ppm) has the highest temperature coefficient. On the other hand the alloy with the highest solute content (O=137ppm, S=3820ppm) has the lowest surface tension. Keene and co-workers(1986) proposed that if a strongly surface active element exist in a liquid the second term in equation 5.5, whose magnitude changes with temperature, becomes dominant. In this case, it is possible to have a large temperature coefficient of surface tension which has a positive value. One might therefore obtain a larger value of $d\sigma/dT$ and a lower value of σ. This proposal is not supported by the results of this study. The temperature coefficient is not high as theoretically expected according to Keen's proposal.

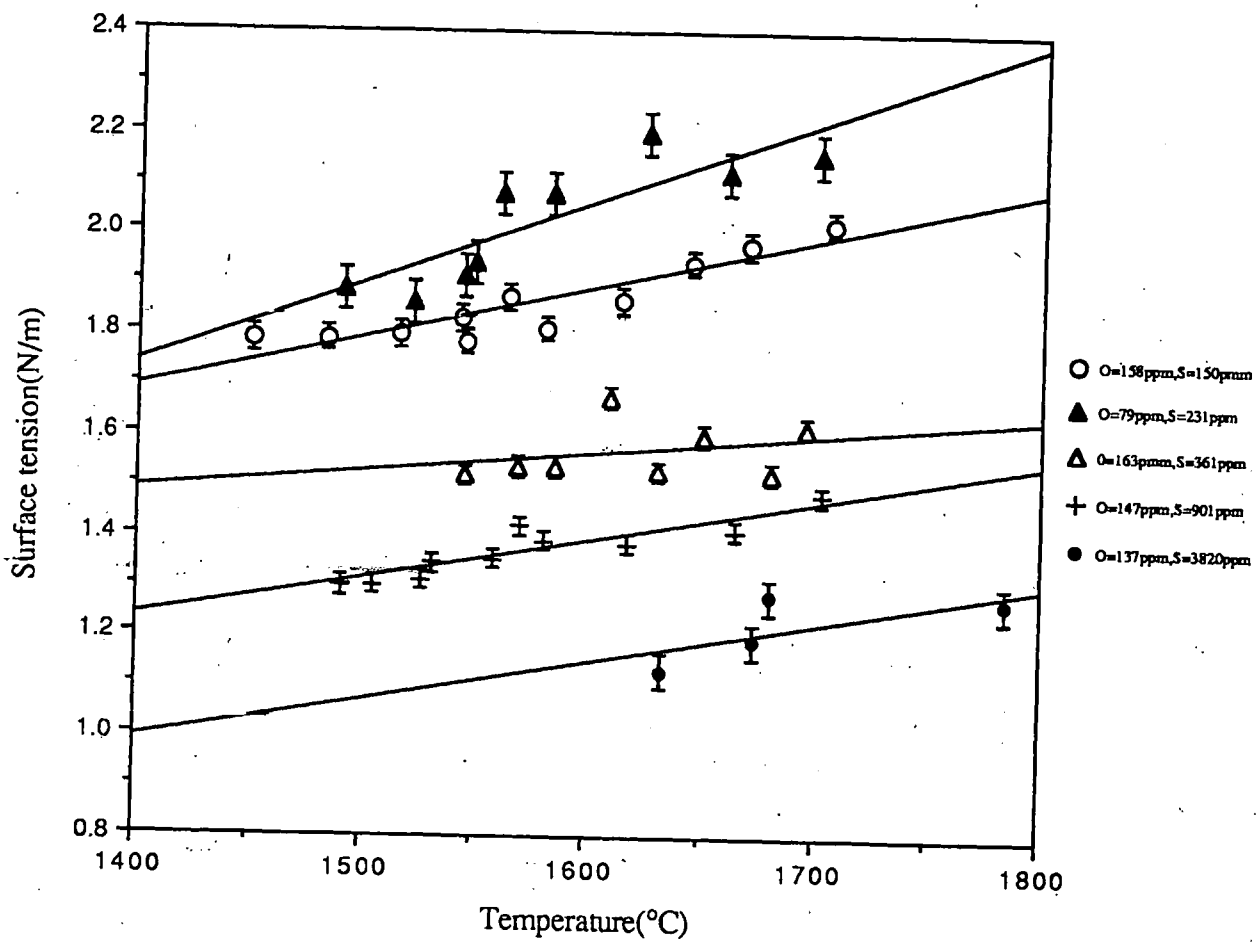

Figure 7.3 Surface tension of 304 stainless steel at different oxygen and sulphur content above liquidus temperature.

σ N/m	d N/m.°C	∂σ/∂T mN/m.°C	O (ppm)	S (ppm)
1.8-2.0	0.327	0.973	158	150
1.9-2.2	0.485	1.587	79	231
1.5-1.6	0.991	0.355	163	361
1.3-1.5	0.141	0.780	147	901
1.1-1.2	-0.098	0.777	137	3280

Table 7.3 The surface tensions and temperature coefficients for the various surface active solute concentrations of 304 stainless steel.

Chapter 8

Results and Discussion on the Casting of Strip

8.1 Introduction

The delivery of molten metal onto the water cooled wheel to produce strip requires the following crucial considerations for the single roller direct casting technique;

- Design of caster, pouring channel, lip and refractory materials.
- Control of gap between casting wheel and crucible lip during metal delivery.
- Control of alloy chemistry of melt, viscosity and surface tension.
- Process control(including superheat, wheel and plunger speed, the stability of meniscus and casting rate).

The design and manufacturing of high performance refractories with high thermal shock resistance and insulation of pouring channel are crucial considerations. Detailed information about the refractory and induction furnace are given in Chapter 6. The pouring channel lip dimensions and heat transfer conditions in furnace are related to thermocapillary flow(Marangoni flow). The channel has to be designed to keep temperature difference in the flow minimum. Marangoni flow may result in edge defects and variation in width of strip.

The other factors controlling the casting process are related to the de-

sign of casting apparatus, the casting wheel, crucible and furnace associated with it. Wheel material composition and size should be selected according to the alloy system being cast. Wheel material affects both wetting by the molten metal and heat conduction away from the solidifying strip. Often the wheel material is chosen for a single criterion, such as maximum thermal conductivity. Wheel size should be viewed as affecting contact pool length (the distance parallel to casting direction at which liquid metal resides on the chiller before thin strip is dragged out) and thermal cycle time (i.e cycle time between hot metal contact at the lip). The other considerations in addition to wetting and thermal conductivity; thermal fatique and surface maintenance are two important criteria to consider for large scale production. The importance of drum surface chemistry is directly related to wetting, which subsequently affects several other operational parameters. For example, as the degree of wetting decreases, the strip temperature leaving the drum increases. Wetting also affects the cooling rate and the microstructure of the strip. These two factors, strip temperature and microstructure, affect the post casting treatment and handling.

The strip dimensions are related to the material flow rate, viscosity, surface tension and heat flow conditions. Width of strip is controlled by the width of the pouring channel lip. Strip thickness, however is controlled by several factors such as the composition of strip material being cast, viscosity, surface tension, heat capacity, thermal conductivity, melting and freezing characteristics and density.

Since it is necessary to obtain good surface properties in thin strip casting the importance of establishing a molten steel pouring technique which will ensure a stable meniscus level is a critical technical problem, (Tozawa, Moriwaki and Yasukawa(1990)). A stable meniscus can be formed by controlling the alloy chemistry and the casting rate. Uniform and controlled casting rate yields good and continuous strips. Any variation of casting rate results in defects and edge serrations. Contact pool length is a geometric factor that is determined by the radial position of the furnace lip(9 o'clock, 12 o'clock, etc), lip geometry design and wheel size. Contact pool length

is one factor affecting strip thickness and quality. However, it is not easy to establish a quantitative relationship between pool length and strip thickness. The drum temperature, surface must not only be controlled, but it must be uniform over the entire drum surface since it affects the wetting characteristics and thus the heat transfer surface area and variations would cause variations in strip characteristics, especially thickness.

In this chapter, the results of strip casting experiments on the interrelation of meniscus, melt pool shape and surface tension are presented and the effects of these parameters on the strip dimensions and quality will be discussed.

8.2 Design of pouring channel and lip

A great deal of attention must be paid to the preparation of the molten metal by controlling the viscosity, surface tension and flow rate for the casting step in strip casting by melt overflow. Channel width and channel geometry must be carefully designed. First, liquid metal has to be delivered from the furnace by displacing the furnace charge by an inert (refractory)plunger. At the end of this initial plunger movement, the pouring channel is filled with liquid metal but soon after the metal in the channel solidifies. It is necessary to keep at least 1mm gap between lip and wheel until the solidified charge in the pouring channel remelts and spontaneously moves toward the rotating wheel.

Remelting of the charge in the pouring channel requires specific heat transfer conditions. Primarily, refractory thickness and quality of insulation materials are extremely critical factors because they are related to the performance of caster. Liquid metal which has high specific heat and superheat has to be delivered within a channel without loosing its superheat. But the channel refractory must maintain its rigidity and soundness, even though a drastic thermal gradient exists through its thickness. The top turn of the induction coil is right underneath of the refractory to provide induction heating to the charge in the channel. But a refractory thickness more than

8mm and a coil to pouring channel surface distance more than 15mm results in low heating efficiency. So strip casting is not possible for this condition. The importance of designed of pouring channel and lip becomes more clear if the heat losses are high and furnace efficiency is low. Heat in pouring channel is found to be most critical operation parameter. The sufficient volume of metal and heat should be kept in pouring channel before the casting. The width(w) to height(h) ratio of each cross section area along the mass flow direction controls the heat loss and efficiency. Because this ratio is related to the surface area to volume ratio of the channel. Lower the surface area to volume ratio corresponds lower the heat losses. The heat in channel can be calculated as $Q_{ch} = (volume \times density/mol.weight)(Q_1 + Q_2 + Q_3)$ from equation 4.18,19,20. The Q_{ch} along the mass flow direction for a casting at $1630°C$ and w/h ratio determined experimentally for the most efficient channel geometry are given in Figure 8.1.

8.3 Thermocapillary Convection and Surface Film Effect

The stainless steel alloys deoxidized by ferromanganese resulted in smooth edge uniform strips compared to ferrosilicon deoxidized runs which ended up with serrated edge strips in some experiments. Figure 8.2 shows the strips produced under different casting conditions and deoxidation practice. These serrations may also originate from variation of solid skin composition and strength proposed by Schwabe and co-workers(1989). This may be because the surface film on the liquid suppressing the surface tension driven flow and subsequent instabilities. In melt overflow, both Marangoni and Kelvin-Helmhotz instabilities may originate and develop within the melt pool. The melt pool is not disturbed both by the transferred wheel momentum and air flow created by wheel and also the surface tension fluctuations, Marangoni flow and the main fluid flow of casting process. It is a complicated problem and the combined disturbances may result in smooth or serrated edge strip.

The final strip quality depends on :

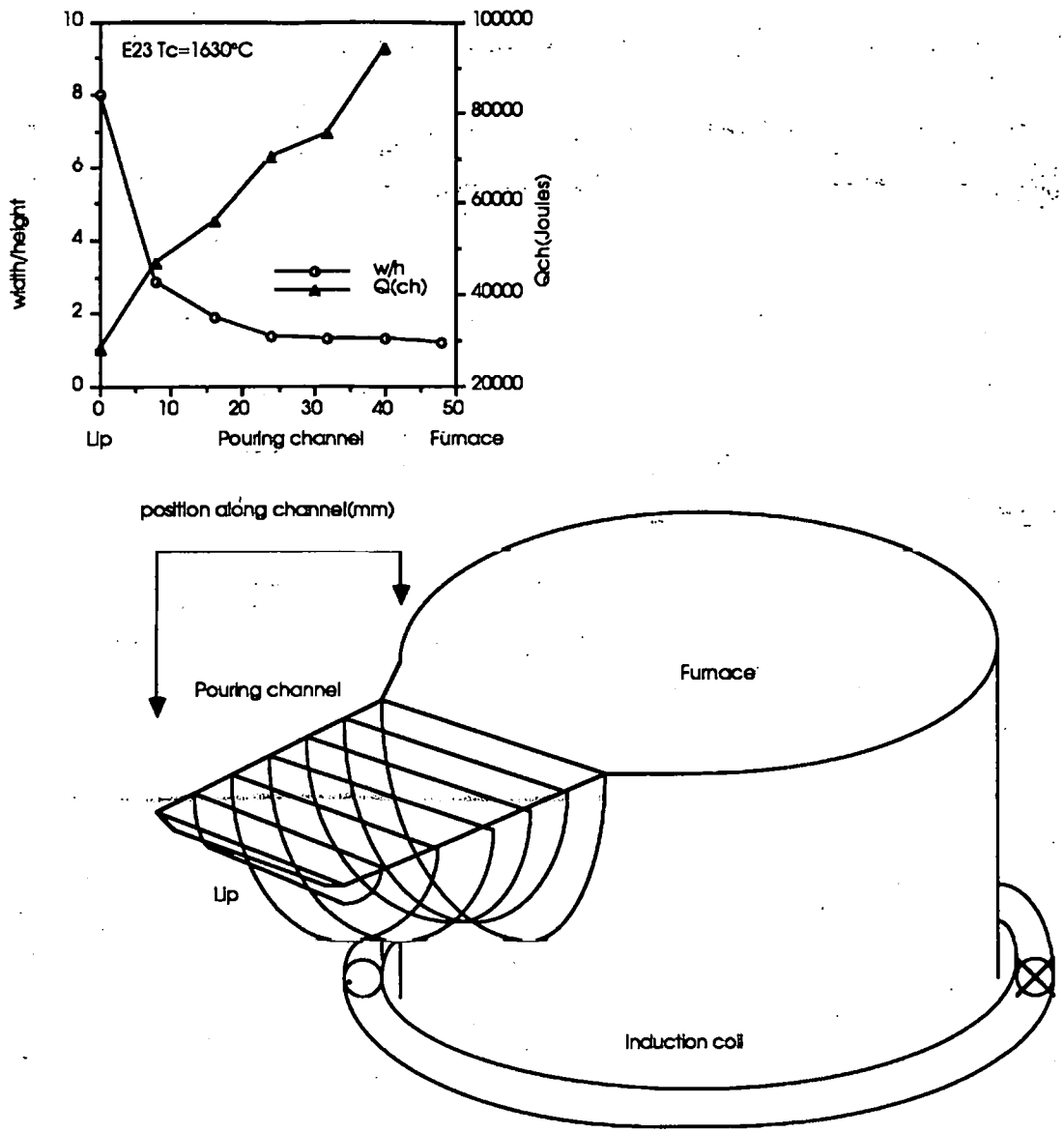

Figure 8.1 The schematical cross section of furnace pouring channel and variation of dimensional ratio and heat in channel for a casting at 1630°C.

1-The difference between casting speed and theoretical speed necessary to wash away instabilities. Figure 8.2 shows how ΔV value affects the suppressing the instabilities and serrations.

2-Marangoni number of the process should be small. This can not be seen easily because the suppression of Ma flow is also dependent on the surface film chemistry.

3-Deoxidation which will control the liquid surface film viscosity.

4-The melt viscosity which can be controlled by adjusting the superheat, silicon and sulphur content of alloy.

The importance of surface film on the liquid metal flow was reported by Massoubre and Pflieger(1978). They developed a method for transforming molten steel directly into solid wire with a diameter of about 0.1mm. To produce a continuous wire, the jet should be solidified before the break up occurs; to increase the cooling time, it is therefore necessary to lengthen the cylindrical part of the jet. Massoubre and co-workers also reported that surface active elements incorporated into the steel could help increase this length by decreasing the surface tension. Previous work in the field was reviewed and augmented by Hansen(1965) regarding the propagation and damping of waves at fluid interfaces shows that the formation of a viscous film on the surface of the jet can considerably modify the development of the striction waves which cause the break up of the jet. The formation of such a film can be achieved through various chemical reactions between one element of the steel and one element of the cooling atmosphere. Among all the possibilities, the formation of an oxide sheath through the reaction between a reductant added to the steel and an oxidant included in the cooling medium is the easiest way in terms of industrial development. Silicon steel was used the cooling medium, which was mainly hydrogen, carried an oxidant made by adding oxygen donors such as steam, carbon dioxide or carbon monoxide to it. Therefore, on the surface of the jet an almost pure silica film should be formed. Continuous cylindrical jets were observed by Massoubre under these conditions.

The viscosity of the oxide film appearing at the surface of liquid stream

is an important factor for wire spinning and possibly for melt overflow. This oxide film, is probably silica. The viscosity of pure silica is very high at a temperature of 1500°C (10^9 poises are reported), Massoubre and Pflieger(1978). This decreases in the presence of metallic oxides. As regards silicon steel the superficial layer formed always contains some traces of iron oxide and for stainless steel chromium oxide or iron-chromium oxide, Massoubre and Pflieger(1978). It can contain other oxides, depending on the steel composition. It has been proven experimentally by Massoubre and co- workers that this glassy phase must retain a relatively high viscosity to play its part properly. Massoubre also reported that if the operating conditions involve the formation of a film of low melting silicates, the viscosity of which can be lower than 1 poise, the sheath stabilizing effect is no longer sufficient, and the break up into drops, though postponed, happens before before solidification.

In Figure 8.2 Korber and Oelsen's(1957) proposed curve of equal deoxidizing power of silicon and manganese at temperature of 1550 °C has been reproduced. For all the compositions corresponding to area 1, the oxidation product at equilibrium is silica. All compositions of area 2 correspond, to an oxidation product, low melting silicates with various ratios of silica/manganous oxide. Massoubre reported that as soon as the ferromanganese had dissolved into the steel in the crucible, that is, after a few seconds, the wire disappeared and shot was obtained. It is proposed that the silicon content of a steel containing manganese must be sufficient for the first oxidation product. Cherukuru and Mamro(1979) reported that the stainless steels deoxidized by aluminium and silicomanganese yields liquid iron, chromium aluminium and manganese silicate inclusions which float out the melt easily. These oxide inclusions are complex of Fe, Al, Cr, Si and Mn only and Cherukuru and Mamro also investigated these inclusions and reported that after microprobe examinations no simple oxides like Al_2O_3, SiO_2 or MnO were present. This shows that the products of deoxidation of silicon and manganese also nucleate heterogeneously upon already existing chromium aluminium oxides. The ferromanganese deoxidized stainless steels

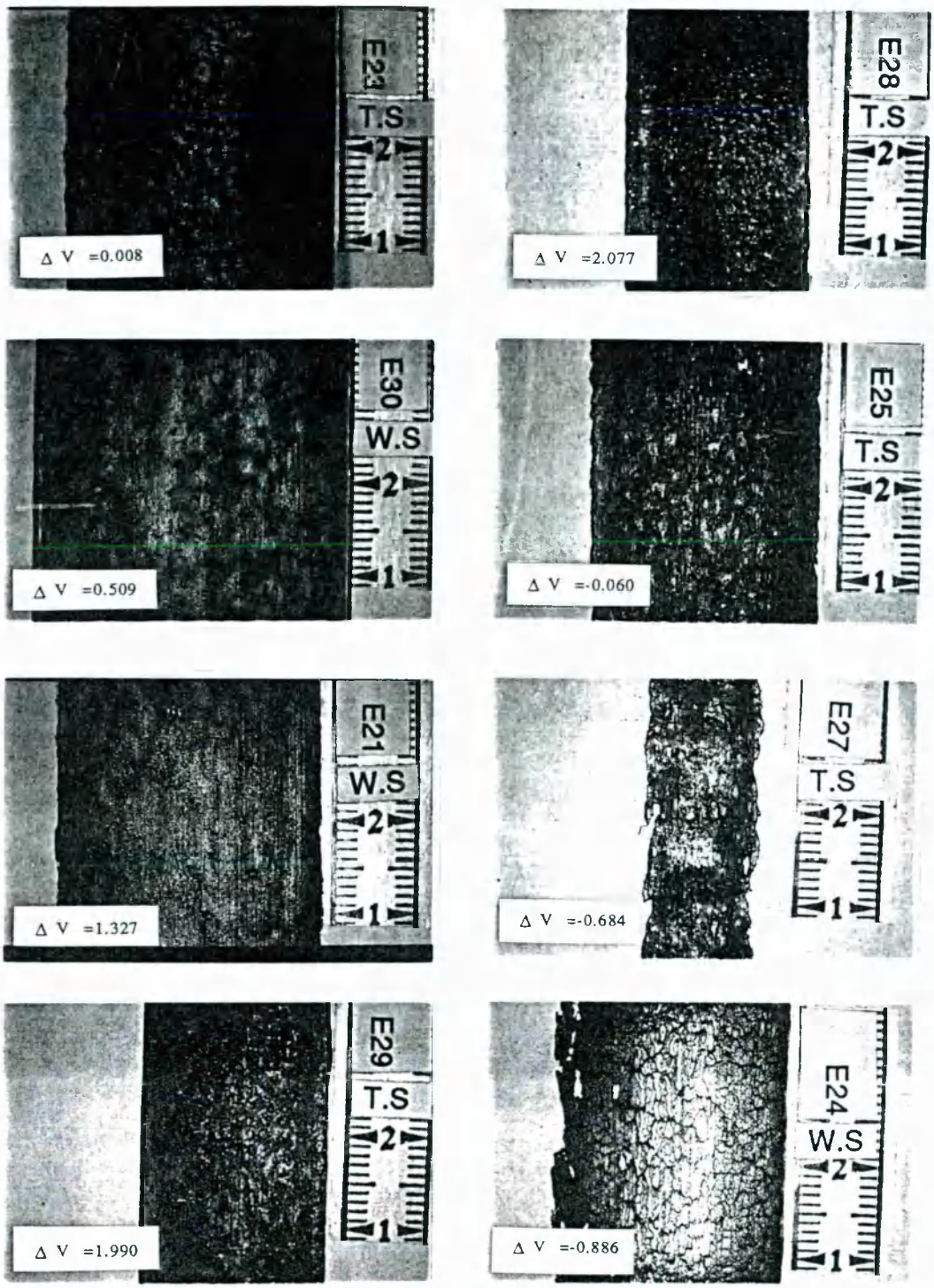

Figure 8.2 The strips produced under various casting speed and deoxidation agents. E numbers refer to specific experiments and ΔV values refer to the difference between casting speed and theoretical speed necessary to wash away instabilities.

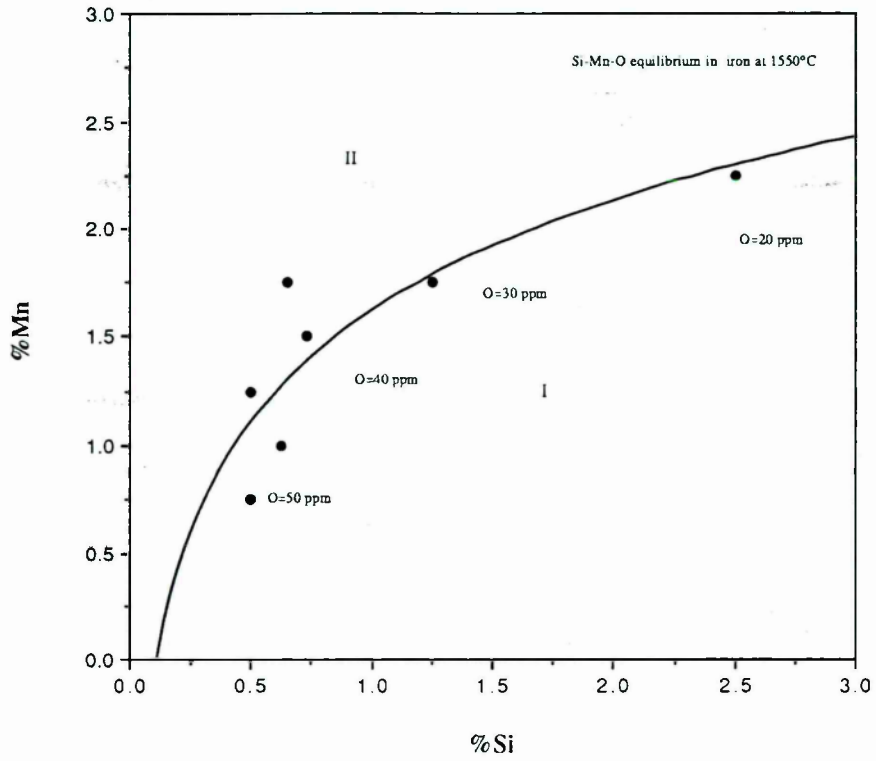

Figure 8.3 Deoxidation power of Mn and Si in liquid steel proposed by Korber and Oelsen(1957).

melts probably yielded such a complex liquid oxide film on the surface of melt pool and the viscosity of this oxide film was sufficiently high to stabilize the developing Marangoni flow.

8.4 The effect of Surface Tension on Strip Edge and Melt Pool

The aim of surface tension measurements was to investigate the role of the temperature coefficient and the absolute value of surface tension at casting temperature on the melt pool shape, the critical conditions in which growing instability suppressed by σ_{LV} and the as- cast strip characteristics.

First, the possible relation between temperature coefficient of alloy and strip edge serrations were analyzed to reveal the Marangoni flow dependence of the instabilities. Table 8.1 presents $\frac{d\sigma}{dT}$ against serration size and variation in width. Although there is no strong linear dependency between temperature coefficient and the nature of serrations in a wide range such as 1.01×10^{-3} to -6.22×10^{-5} both low and high serration size may occur according to the value of Marangoni number and the value of surface tension at pouring temperature which governs the critical casting speed necessary to wash away instability waves travel within the melt pool. It can be understood that increasing sulphur concentration doesn't control the temperature coefficient and Marangoni flow, but it reduces the absolute value of surface tension and increases the size of serrations. Surface tension values of 304 stainless steel alloy and Ni-B-Si alloy greater than 2.4 Nm^{-1} corresponds to high surface tensions which prevent liquid surface of liquid pool from dragging parallel to the momentum transfer by the wheel. High σ_{LV} values were observed when deoxidation by Al and FeSi were applied effectively attaining final low oxygen concentrations such as 95 ppm O in stainless steel.

For surface tension values lower than 2.2 Nm^{-1} almost every run could have produced some strips succesfully, dragging the liquid metal in the pool out and forming the strip on the wheel.

The presence and severity of instabilities and their final effects on the

%S	σ at Tcast (N/m)	dσ/ dT *10^{-3}	Description of strip	Width(mm) min	mean	max	Edge notch size-Se(mm)		Δ V (cm/sec)
0.0122	2.09	1.010	uniform edge low oxide	28	28.5	29	0.7-1	(1)	0.008
0.0127	2.15	0.814	uniform edge low oxide	29	29.5	30	0.5-0	(1)	
0.0150	2.02	0.973	uniform edge low oxide	20	20.0	20	0.001	(2)	1.99
0.0170	1.94	1.359	serrated edge, voids	11	11.5	12	1.2-1	(2)	-0.684
0.0181	1.71	-0.062	uniform edge, low oxide	7	7.0	7	0.1-0	(2)	
0.0189	1.94	1.362	non uniform width	4	5.0	6	0.05-0	(1)	
0.0195	1.97	1.479	serrated edge, voids	22	26.0	30	1	(2)	-0.060
0.0203	1.95	1.215	serrated edge, voids	22	26.0	30	1	(2)	
0.0217	1.84	0.772	serrated edge	15	17.5	20	0.05-1.5	(2)	
0.0224	1.83	0.957	uniform edge	15	17.5	20	0.05-1.5	(2)	2.077
0.0231	2.15	1.587	uniform edge, low oxide	29	29.5	30	0.5-0	(1)	
0.0232	1.99	1.529	uniform edge, low oxide	32	33.0	34	0.01-0	(2)	0.509
0.0268	1.72	0.425	uniform edge, some voids	26	27.0	28	0.05-0.01	(2)	
0.0272	1.67	0.643	uniform edge, some voids	26	27.0	28	0.05-0.01	(2)	1.327
0.0361	1.58	0.355	serrated edge	5	5.5	6	1.6-1	(2)	
0.0382	1.63	0.449	serrated edge, voids	20	22.5	25	0.01	(2)	
0.0736	1.43	1.224	uniform width, oxide	25	30.0	35	2	(1)	
0.0901	1.42	0.780	serrated edge, oxide	25	30.0	35	2	(1)	-0.886
0.3820	1.11	0.777	serrated edge, voids	8	9.0	10	2-3	(2)	

(1) serration at one side

(2) serration at both sides

** sulphur in sample after surface tension measurements

Table 8.1 Strip characteristics and temperature coefficients.

strip were analyzed by considering Ma for the system. High Ma may be a result of a wide lip, high alloy temperature coefficient or superheat of liquid metal. The Marangoni numbers calculated from equation 5.13 are between 247000 and 57850. The highest Marangoni number corresponds to a serrated edge strip with an edge notch size 1.2mm and lowest Marangoni number 57850 corresponds an edge notch size 0.05mm. Although the other experimental results on edge serration sizes are not strongly related to Marangoni number, the extreme cases revealed that there is consequence effect of high Marangoni number on strip edge characteristics. The Marangoni numbers of all experiments are given in Appendix. Experimental observations by video camera revealed that high instabilities exist at the beginning and of the melt delivery. Marangoni flow developed on the melt pool may be the source of capillary waves and variation in the width of strip. But pool stability is also related to fluid flow rate and its subsequent suppression effect on the instabilities. In melt overflow experiments lip width was kept constant as 30 mm since wider values developed high Marangoni flows and caused breaking up of liquid stream.

Since a ferrous alloy's viscosity term in the Marangoni number is also oxygen and sulphur dependent it is difficult to investigate the effects of these elements on surface tension, serrations and viscosity individually. This shows that low viscosity results in thin strip and low surface tension results in failure of preventing the instabilities such as Marangoni and Kelvin-Helmholtz due to the subsequent effect of sulphur in solution. Thickness calculations which includes hydrodynamic limiting liquid thickness prediction will be presented in the following section.

Liquid metal delivery in melt overflow is a delicate operation and needs considerable attention since the unconstrained liquid metal flow has to be controlled by both surface tension and flow rate. At the initial stage liquid metal front is forced to move by head creating by plunger down drive. At this very first time severe Marangoni and Kelvin- Helmholtz instabilities develop. This was observed during every experiment performed. Soon after the molten metal is succesfully dragged out of the pool, flow develops and

yields thin strip on the chiller.

For the surface tension of alloy between 2.1 and 1.4 Nm^{-1}, uniform strips can be produced for wheel speed 2.78 ms^{-1}. Equation 5.3 explains the balance between shear forces created by the wheel counteracting the surface tension in the liquid surface. The flow rates such as 21.8, 16.7, 14.2 and 9.8 $c^3.s^{-1}$ yielded edge defects free and the strips with saw edges. The variation of melt pool dimensions against time creates new equilibrium conditions for flow to stabilize itself if surface tension values are small and ΔV values are negative as in experiments 24, 25 and 27 (Figure 8.2). Surface waves generated by flow rate fluctuations and momentum transfer gradually develop during travel from the centre to the upper region where solidification starts. The shape of the wave is frozen as a saw edge pattern by solidification. Some waves are suppressed by surface tension before they reach the solidification point. The strips of experiments of 21, 23, 28, 29 and 30 (Figure 8.2) which were consistent with the criterion proposed by Anthony and Cline(1978) and given in chapter 5 revealed that waves could have been suppressed before they reached the solidification point under specific circumstances.

These results also demostrate that ΔV the speed difference of the experimental casting speed V_c which was given in appendix and the theoretical speed-V_j necessary to prevent instability waves defined in equation 3.7 is a major criterion that we can use to explain saw edge formation. Yuhara and co-workers observed a similar edge saw formation in twin-roll process but they applied electromagnetic field which created Lorentz forces to suppress surface waves on the melt pool. Optical photography was used to examine the side view of melt overflow and meniscus in developing region. Figure 8.4 shows the meniscus and developing of thin strip on the chiller. The liquid metal heights at the lip were found to be directly proportional to the pool length where the liquid metal is dragged out of the pool. This can be seen in Figure 8.5. Liquid height drops gradually toward the end of melt delivery. The liquid heights such as 9 and 8 mm generally yielded saw edged strip but liquid heights such as 14 and 16mm yielded uniform strips. The width of strips varies between 9 and 30 mm. The results revealed that the di-

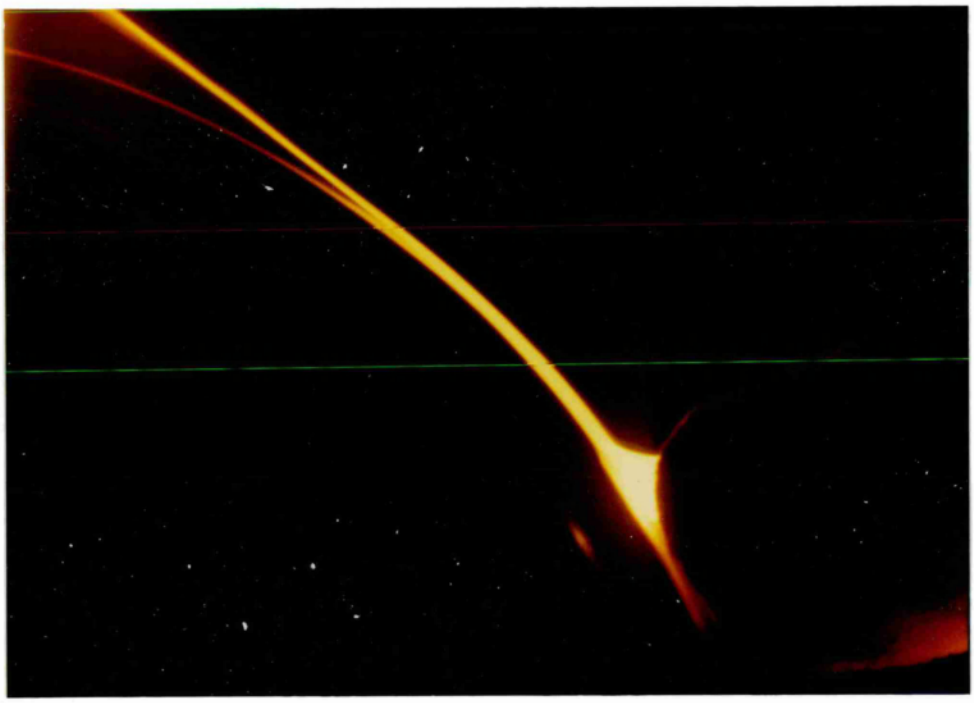

Figure 8.4 Meniscus and developing of thin stainless steel strip on the wheel.

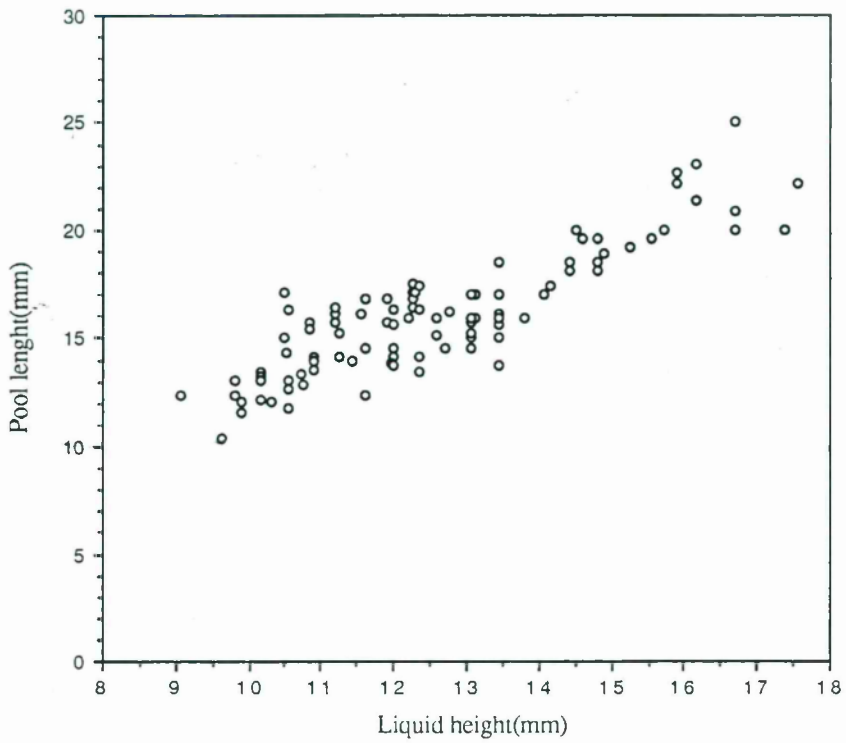

Figure 8.5 Melt pool dimensions measured by photographic enlargement technique.

mensionless liquid height (Lh)/width (w) ratio for a series of stainless alloys which have different surface tensions were in range of 0.3-0.9. Good edge strips were produces in experimental conditions which provide a ratio such as 0.6-0.9. The measurements done on the side view photographs of the meniscus and analysis of surface tensions performed by the modified droplet technique showed that Lh/w ratio was linearly proportional to the surface tension. Figure 8.6 shows this relation. Melt pool shape observations on the

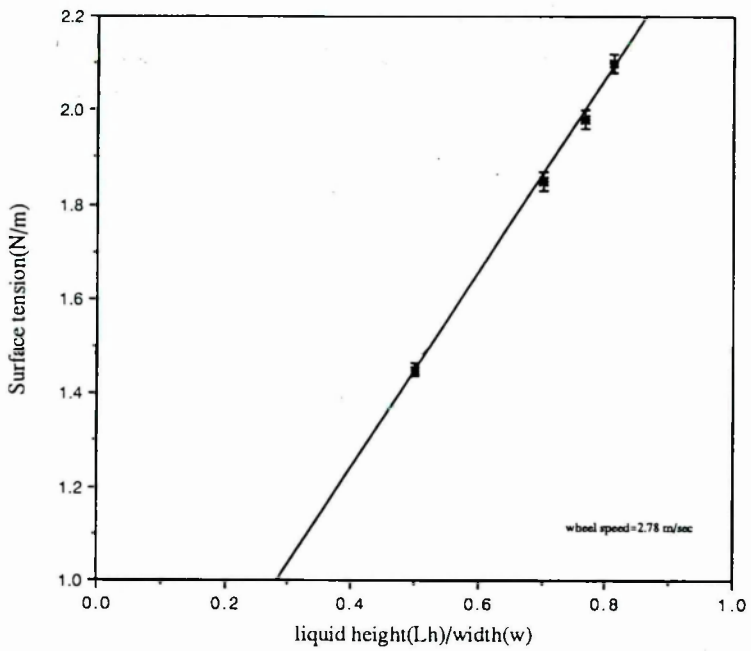

Figure 8.6 The effect of surface tension on liquid height/width ratio.

photographs revealed that alloys which has high surface tension has bigger meniscus radius. As an example, these radius values were measured as 14.52 and 7.7 mm for the surface tensions 1.98 and 1.43 Nm^{-1}.

8.4.1 Meniscus Characteristics

Meniscus and strip formation of 304 stainless steel strip casting were photographed and are shown in Figure 8.4. The meniscus of liquid film formation region was investigated. Photographic enlargement technique was used to measure capillary radius for the melt overflow experiments using 304 stainless steel with different surface tension values. The relationship between the strip thickness and the radius of curvature of the meniscus at its apparent point of tangency with the wheel was obtained by regression analysis of the data and capillary numbers calculated. The result is

$$\frac{t}{R} = 2.830 \times 10^4 \times (Ca)^{2.93} \tag{8.1}$$

where t is the strip thickness, R is radius of curvature and Ca is capillary number. The exponent and constant of this equation are different than equation 2.18 proposed by Ruschak(1976) for aqua solutions due to high surface tension and viscosity values of liquid metals compare to aqua solutions.

8.5 Melt Pool Oscillations

A series of experimental side view photographs showed that variation of liquid level and melt pool length were nonlinear. A synchronized correlation against process time were observed between these parameters. Figure 8.8 shows that any long wave may develop within the melt pool instantly appears at the end of liquid pool. A variation of width was also observed on the strips. The stable melt pool condition in runs like 23, 25 and 29 yielded uniform width strips.

The possible origin of long wave length oscillations are related to thermal convection and non uniformity in flow and melt delivery from the furnace by constant plunger movement. The author suggests that practical operational skill is essential to control liquid metal delivery. It was observed that at the beginning of metal delivery owing to the unsteady state heat transfer to the refractory of pouring channel and unbalanced heat losses within this zone, viscosity and subsequent flow rate variations occured the during process.

Another characteristic of single roller strip casting at low wheel speed ($2.78 ms^{-1}$) is variation of residence distance against operation time. This was observed during melt overflow of stainless steel. This may presumably originate from unconstrained strip flow and back travelling waves reaching to the end of solidification zone. Another reason is irregular disintegration of oxides on the surface of strip on the wheel side. These variations in the residence area was not observed in melt overflow of Fe-Cr-Al and pure aluminium due to stable and thin alumina formation on the surface. Figure 8.9 shows the periodic variation of residence distance of strip on the wheel. A wavelength of residence distance variation 0.65, 0.80 and 0.96 s^{-1} were observed for experiments 24, 25 and 27.

8.6 The Relationship of Strip Dimensions to Casting Conditions

The derivation of the functional relationships between casting conditions and strip dimensions have been carried out, observations are:

1) Strip dimensions are basically controlled by momentum transport and volumetric flow rate of liquid metal and its physical properties such as viscosity, surface tension and density.

2) Molten metal impinges on the circumferential surface of the water cooled wheel where it stays in contact for a time equal to melt pool length/wheel speed. The solid/liquid interface advances perpendicular to the chiller surface at a rate dependent on heat extraction across the wheel/strip interface. Dendrites grow perpendicular to the chiller. They form a solid boundary layer.

3) If momentum transfer from the chill surface is much faster than thermal transport, a liquid boundary layer is dragged out of the melt pool by the moving substrate to solidify further downstream. The velocity gradient is continuous across the depth of the pool.

The functional relationship of strip dimensions thickness and width were investigated and their dependency on flow rate were examined from the

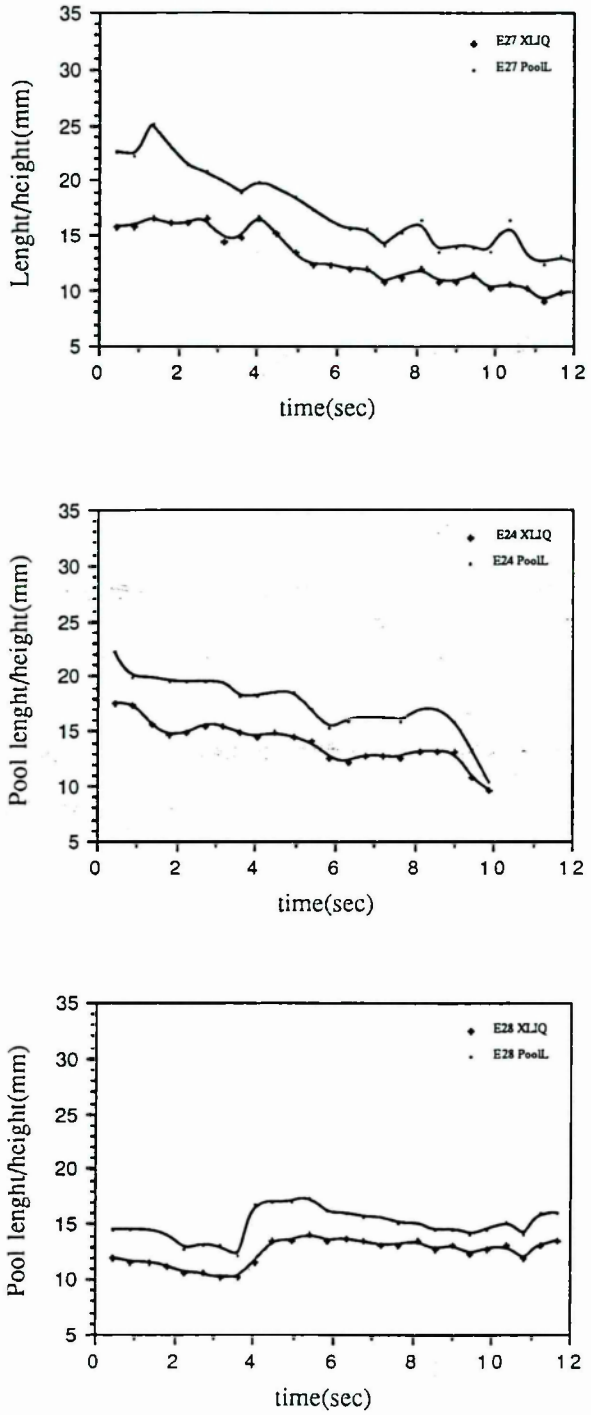

Figure 8.7 The variation of pool length and height against time in melt overflow

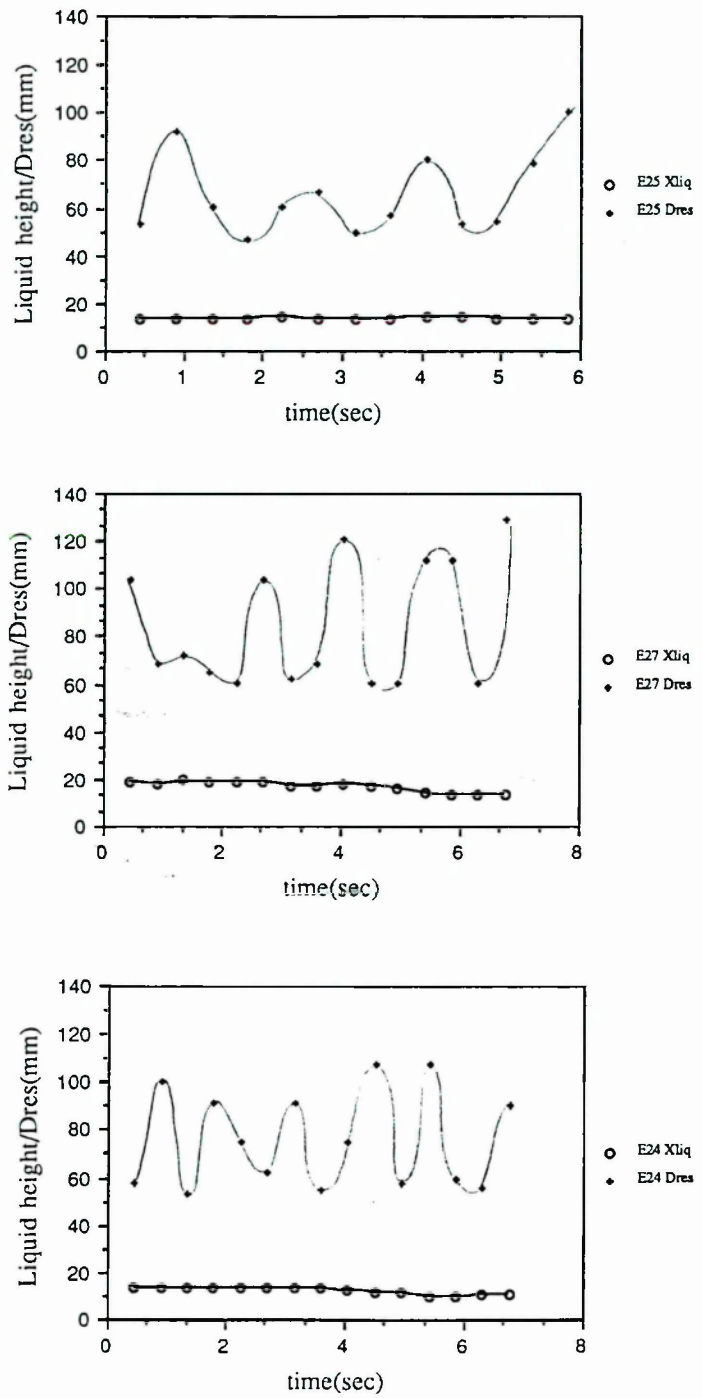

Figure 8.8 The variation of residence distance during melt overflow of stainless steel

equations 2.54 and 2.55 given in chapter two. The value of exponent were found to be as 0.81 from the regression analysis of thickness and flow rate data. This result is different than the results reported by Kavesh (1976) for melt spinning of $Fe_{40}Ni_{40}P_{14}B_6$ alloy which the exponent was found to be in the range 0.77-0.73. On the other hand the value n calculated from the regression analysis of width and flow rate data were calculated as 0.797. So the exponent calculated from two set of equation and data are consistent. Since the interpretation of the numerical value of n is still a matter of argument by a number of investigators. It is assumed as a number to define the equations 2.54 and 2.55. Hence the equations of thickness and width can be written as;

$$t = 1.3331\frac{Q^{0.19}}{V_R^{0.81}} \qquad w = 0.751\frac{Q^{0.81}}{V_R^{0.19}} \tag{8.2}$$

The graphical presentation of experimentally obtained data is given in Figure 8.10. The width was found to be strongly dependent on flow rate for melt overflow of stainless steel. In contrast, strip thickness was a weak function of volumetric flow rate- Q. The results are consistent with those of Liebermann and Graham(1976), Cantor(1980), Liebermann(1980), Kavesh(1976) and the results of this work.

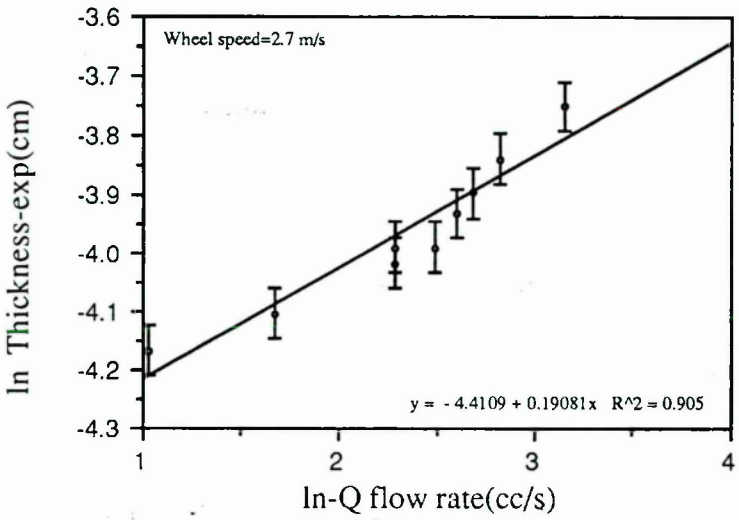

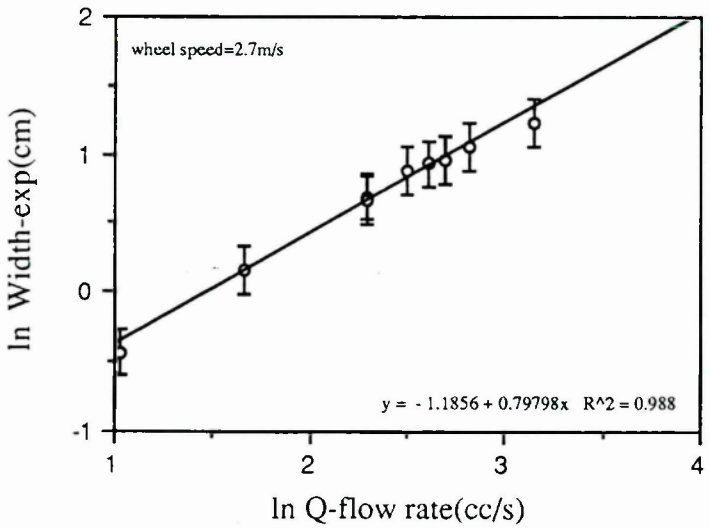

Figure 8.9 The log-log presentation of variation of strip dimensions against volumetric flow.

Chapter 9

Results and Discussion in Heat Transfer Analysis of Melt overflow

9.1 Introduction

The heat transfer analysis of a solidifying thin strip on a rotary chiller are studied in Chapter 4. The analytic solution of heat conduction equation (Equation 4.5) given in Chapter 4 with both convective heat transfer boundary condition and latent heat releasing at solidification temperature range is not possible. This is can only be solved by numerical techniques such as finite difference method.

The model of solidification studied in this section basically consisted of analytical and numerical solutions of the heat conduction equation. Initial calculations showed that these two solutions are identical if the latent heat releasing effect is not included.

In this section finite difference temperature simulation and experimental temperature data are presented. Experimental free surface temperatures were deduced from the photographic measurements. The colour photographs were analyzed by the photogrammetrical technique explained in Chapter 6. An iterative method was employed to find a consistent strip/wheel interface heat transfer coefficient comparing experimentally derived and numerically calculated free surface temperatures. The heat in the metal which needs to be released for solidification of strip on the chiller has been compared with

the calculated heat transfer.

9.2 Finite difference temperature simulation of solidifiying strip

One dimensional heat conduction in perpendicular to the substrate direction was analyzed using a NAG fortran library routine to integrate single linear or non-linear parabolic partial differential equations, using the method of lines and Gear's method (a forward integration technique). Although the strip specific heat was replaced by $C+\frac{L}{\Delta T}$ an arrest was not observed for temperature ranges during solidification 1290-1473 $^{\circ}C$. A three dimensional graphic plot of temperature simulation of melt overflow strip is presented in Figure 9.1. The residence time of the strip is 0.017 sec and casting temperature is 1580 $^{\circ}C$. For large hypothetical undercoolings such as 200-250 $^{\circ}C$, considerable temperature arrest was determined for the range of 1470-900 $^{\circ}C$. This result is consistent with Hayzelden, Rayment and Cantor's (1983) result.

9.3 Free surface temperature analysis of melt overflow strip

Photographic temperature predictions combined with temperature measurements with optical pyrometry was used to predict free surface temperatures. This technique which employs a two colour optical pyrometer focused on the same point in the liquid pool. Simultaneously an optical camera takes a photograph of the same area in order to gather both calibration and free surface cooling data. Lohberg and Muller(1969) have also used pyrometry to measure cooling rates of 10^5 and $10^6 K s^{-1}$ for gun splat quenched Cu and Al respectively. The optical pyrometer readings were recorded on a calibrated Philips strip chart recorder for each experiment. The colour negatives were used to quantify a particular colour hue (red light) which corresponds to the liquid metal temperatures in the melt pools and along the free surface of the

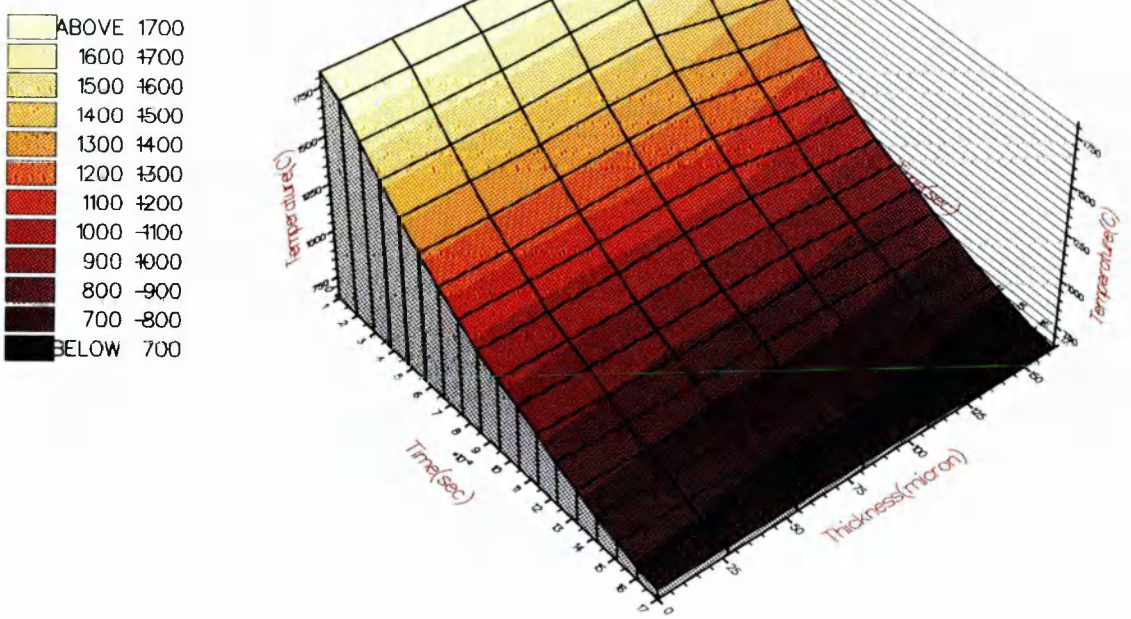

Figure 9.1 Finite difference simulation of temperature field through thickness of strip solidification on chiller for h=5.5 $\times 10^4$ W/m.K for solidification range of 1473-1290 $^\circ C$.

strip for each different experiment. This instrument measured the amount of red light being transmitted through a 1mm diameter aperture placed on the colour negative film. A calibration curve was produced for colour density of the melt pool on film against temperature readings from the same area by optical pyrometry. This graph is presented in the appendix.

The film negative of the top view of each experiment such as in Figure 9.2 was also scanned by a photodensitometer along casting direction. Temperatures predicted from the calibration curve after colour density mea-

Figure 9.2 Direct casting of stainless steel 304 strip over the pouring channel onto the rotary chiller, developing and solidifying of strip by melt overflow.

surements along the colour film of the free surface (experimental) are presented in Figure 9.3. Numerical calculations of free surface temperatures for different empirical heat transfer coefficients were also plotted and shown in the same figure in order to observe any matching between calculated and experimentally determined surface temperatures. The free surface temperature analysis showed that high amounts of undercooling exist at the initial

part of the contact zone but the cooling rate gradually decreases as a result of both recalescence and surface oxidation. A temperature arrest was determined from the top surface temperature predictions via the photographic technique. In Figure 9.2 right after the liquid pool a smooth uniform liquid zone can be seen. After this zone solidification is completed and colour density variation along the surface shows an increase in cooling rate.

The variation in heat transfer coefficient can be estimated from Figure 9.3, which are superimposed experimental free surface temperature curves and calculated for temperature values assuming equilibrium freezing of stainless steel. A post-photographic imaging technique was used to reveal any recalescence occuring during solidification of the strip. Pseudocolour imaging obtained by computer simulated the free surface temperatures.

Temperature variations across the width of the strip show a central darker region and brighter edge, (Figures 9.2 and 9.4). A similar darker central region has been observed previously in melt spun Ni-Superalloy strips by Warrington and Davies(1982). After examination of Figures 9.2 and 9.4, the following possibilities can be suggested to explain the brightening of the strip leaving the contact zone during melt overflow.

1-The central region was adhering better to the wheel surface, leading to greater cooling.

2-The brightening in the edge of strip is associated with recalescence caused by the 304 stainless steel alloy undercooling significantly before the solidification process is nucleated and perhaps the strip in Figures 9.3 and 9.5 remain liquid over most of the field of view so that strip formation is momentum rather than thermal boundary layer controlled which was proposed by Vincent, Herbertson and Davies(1982). i.e a thin liquid strip is dragged out of the melt pool and then solidifies further downstream, rather than a thin solid strip being dragged directly out of the melt pool. According to this hypothesis, the latent heat of solidification should not be included in the heat flow analysis of the cooling by finite difference analysis. The calculated cooling curves were presented in Figure 9.3

3-The strip leaves the wheel and moves from in focus condition and it

may be an out of focus image. Thus, photographs of a constant colour source show an increase in film density as the source moves towards the camera.

4-The brightening on the photographs such as Figure 9.2 and 9.4 corresponds to a temperature well above the 1290-1470$°C$ equilibrium freezing range of 304 stainless steel strip.

Solidification shrinkage leads to poorer thermal contact with the wheel and cooling rapidly becomes near-Newtonian beyond the melt puddle.

The pseudocolour imaging of colour photographs of melt overflow in Figure 9.2 can be quantified by a computer and colour density values of each point on the square grid can be identified using a calibration curve produced from colour densities of melt pools also mapped by pseudocolour imaging. This technique can be used for qualitative interpretation of free surface cooling. Figures 9.2 and 9.4 showed that a sharp temperature drop from 1700$°C$ to 1500$°C$ existed outside the melt pool as measured by a colour densitometer. This sharpness of transition gradually decreased in the casting direction toward the strip residence region.

The dimensional analysis done by previous investigators, Hanses and Anderko(1958), Katgerman(1980), Katgerman and Vanden Brink(1982) showed that, strip formation is usually closer to thermal rather than momentum boundary layer controlled. Thus solidification is complete when the top surface strip temperature reaches 1270-1470 $°C$, shortly after the edge of the melt pool. The latent heat of solidification should therefore be included in the heat flow analysis and computer programme. Gillen and Cantor(1985) reported that the cooling is near Newtonian during melt spinning, with heat transfer coefficients and Biot numbers in the range 6×10^4-$2\times10^5 \mathrm{W}m^{-2}K^{-1}$ and 0.07-0.2 respectively. Gillon and Cantor (1985) also suggested a possible mechanism for strip formation during melt spinning, the strip is formed in the vicinity of the melt puddle (i.e by thermal boundary layer control), where thermal contact with the wheel is sufficiently adequate that cooling conditions are near-ideal.

The following conclusions can be made after examination of photographs of free surfaces and temperature predictions.

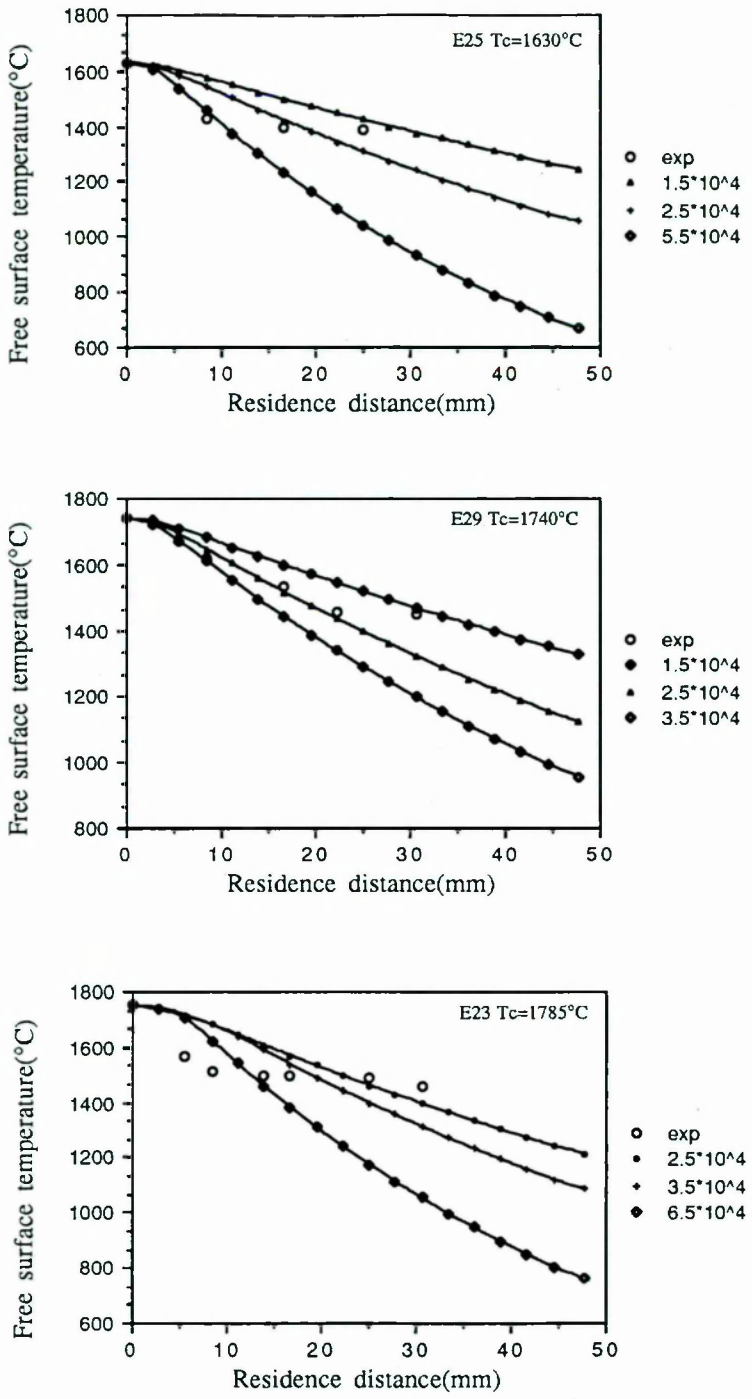

Figure 9.3 Free surface temperatures calculated from finite difference integration for heat transfer coefficients in the range of 1.5 to $6.5 \times 10^4 \mathrm{W} m^{-2} K^{-1}$ and measured by colour photodensitometer.

1) The heat transfer coefficients are in range of $7.5\times10^4-5.5\times10^4 W/m^2K$ at the initial time period of development of the zone beyond the melt pool. This reduces to $2 \times 10^4 W/m^2K$ at the end of the area under observation.

2) A uniform temperature zone is observed where the free surface temperature is nearly the solidification temperature of stainless steel. This zone corresponds to the mushy liquid dragged out of melt pool.

3) Considerable recalescence was indicated near the edges beyond the undercooled temperature zone. There is a 500 $^\circ C$ temperature difference between the edge and the middle of the strip measured by blue colour analysis.

9.4 Heat Flow Analysis

In this section an analysis of heat flow and heat transfer coefficients at the strip/wheel interface are discussed. Since, heat flow from the strip to the gas is controlled by convective heat transfer, an assumption has to be made to fit convective heat transfer boundary condition. The heat flux, calculated from a numerical integration route by solving the parabolic nonlinear partial differential equation 2.25 at the interface, was compared to total heat in the strip calculated from equation 4.17. Equation 2.26 for a chill/strip boundary was used to calculate local heat flow to the interface.

Finite difference results showed that heat flux varies in the through thickness direction. A typical temperature difference at the interface calculated from finite difference integration is 65-85$^\circ K$ in 0.001 second for heat transfer coefficients in range 3.5-5.5 $\times10^4 W/m^2K$. The heat flux value can be calculated from the modified Equation 2.26 as;

$$Q_{int} = K\frac{T_s - T_{i-1}}{m}A \tag{9.1}$$

where T_s is the temperature at the wheel side y=0 at time θ, T_{i-1} is the temperature at m=t/5 at time θ, in through thickness direction (y), A is the cooling area which is defined as w(width)$\times V_R$ (chiller speed). To predict heat transfer coefficient during the process, free surface temperatures were

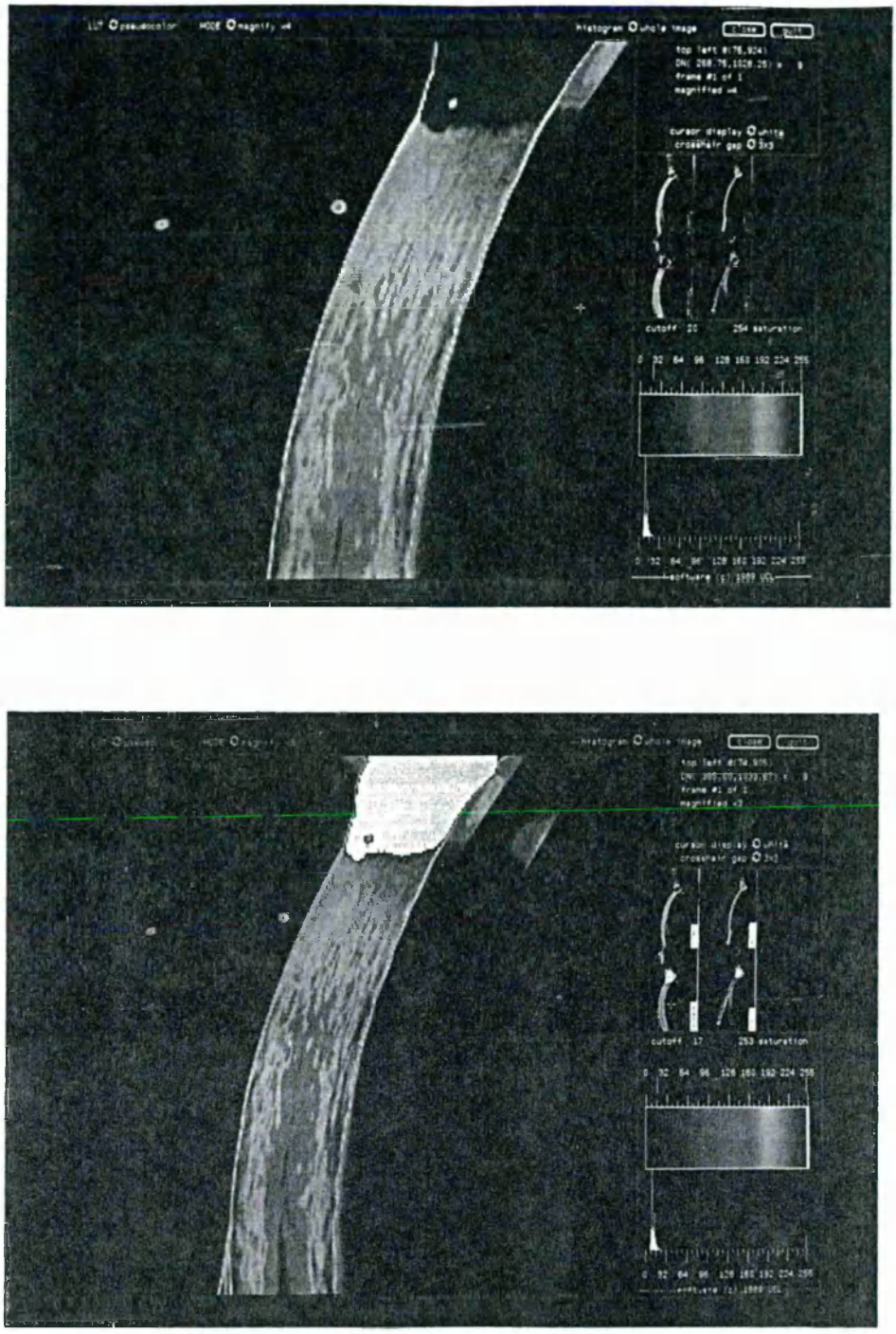

Figure 9.4 Pseudocolour simulation of gray scale light spectra of free surface by histogram.

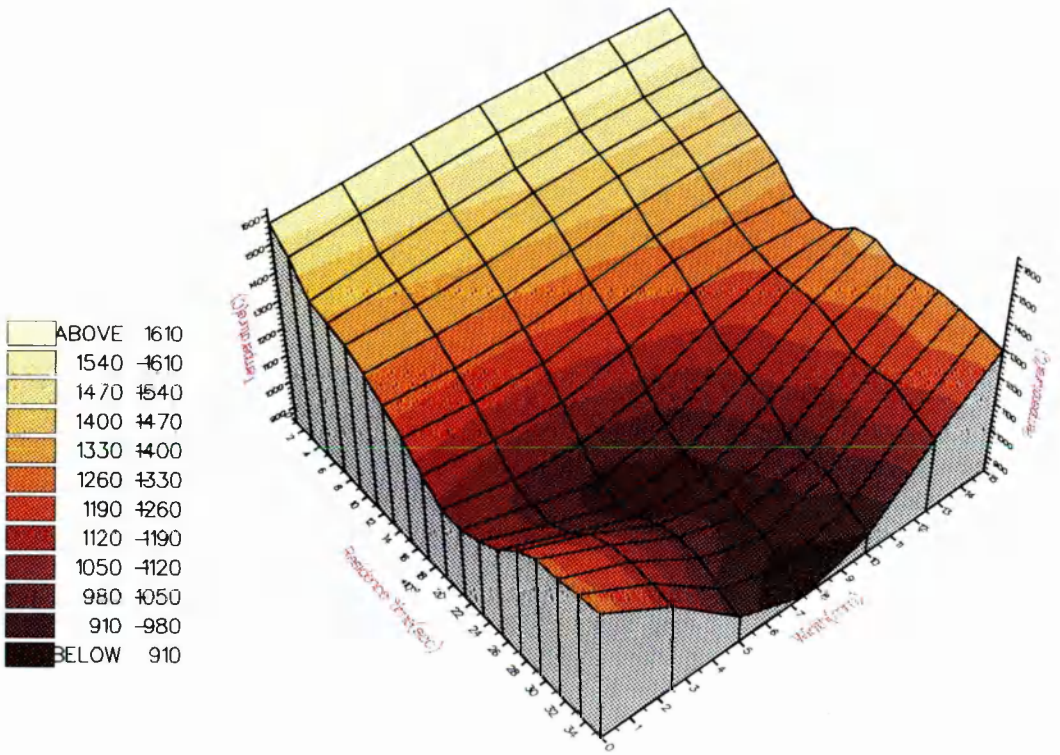

Figure 9.5 Free surface temperature field of strip in Figure 9.2 analyzed by thermogram.

deduced from colour negatives using the calibration the curve derived from photography given in Appendix. Heats in metal strip were calculated for 0.02 sec experimental residence time for a range of $298°K$ to T_c and are given in Table 9.1, column 3.

The question arises here as to whether strip releases its superheat and latent heat in residence area before it takes off. Values of only latent heat and superheat for experiments with 0.02 sec residence time are given in Table 9.1, column 4.

Assuming the heat transfer coefficient predicted from free surface temperature analysis controls the value of heat flow by conduction which is given in column 7 and the release of superheat and latent heat, a comparison can made to test the consistency. As an example for the strip produced in exp 23, the amount of latent+superheat is equal to 1376 joules. Assuming most of the heat is transferred by conduction through thickness a heat transfer coefficient can be deduced from table 9.1 between 3.5 and 6.5 $W.m^{-2}K^{-1}$ which correspond to the conduction heat range of 695 and 1517 Joules given in column 7. The results are given in Table 9.1. Consistent numerical values were observed between heat flow corresponding to predicted heat transfer coefficients and super+latent heat values.

Conductive heat flow values against heat transfer coefficients are given in Figure 9.6. The values of heat transfer by radiation calculated from equation 4.1 show that the proportion of heat released by radiation is a small quantity compared to heat transfer by convection and conduction corresponding to about 0.5% of total heat transfer.

The variation of heat transfer coefficient during strip casting process is difficult to determine because the amount of heat released can not be measured accurately during the process. Tozawa and et al (1990) measured inlet and outlet water temperatures of the chiller and determined heat transfer coefficients by repeating calculations of heat flux in strip and equivalent values of heat taken in by the chiller. They also studied the variation of heat flux and heat transfer coefficient against distance from the liquid pool meniscus. In this study the wheel temperature was assumed to be 298 $°K$.

Exp no:	T_{cast} (K)	Total heat 298 K-Tcast (Joules)	Latent+ Super heat (Joules)	Superheat (Joules)	h (W/m^2K)	Conduction through thickness (Joules)	Radiation (Joules)
23	2058	3655	1376	523	10000 25000 35000 65000	204 496 695 1517	9.4
25	1903	2176	662	130	15000 25000 65000	265 429 1010	5.74
29	2013	2612	912	315	15000 25000 45000	209 340 585	6.09
30	1853	4584	1290	134	35000 45000 55000	700 878 1047	7.63

Table 9.1 Heat flow analysis results of experiments in 0.02 sec residence time.

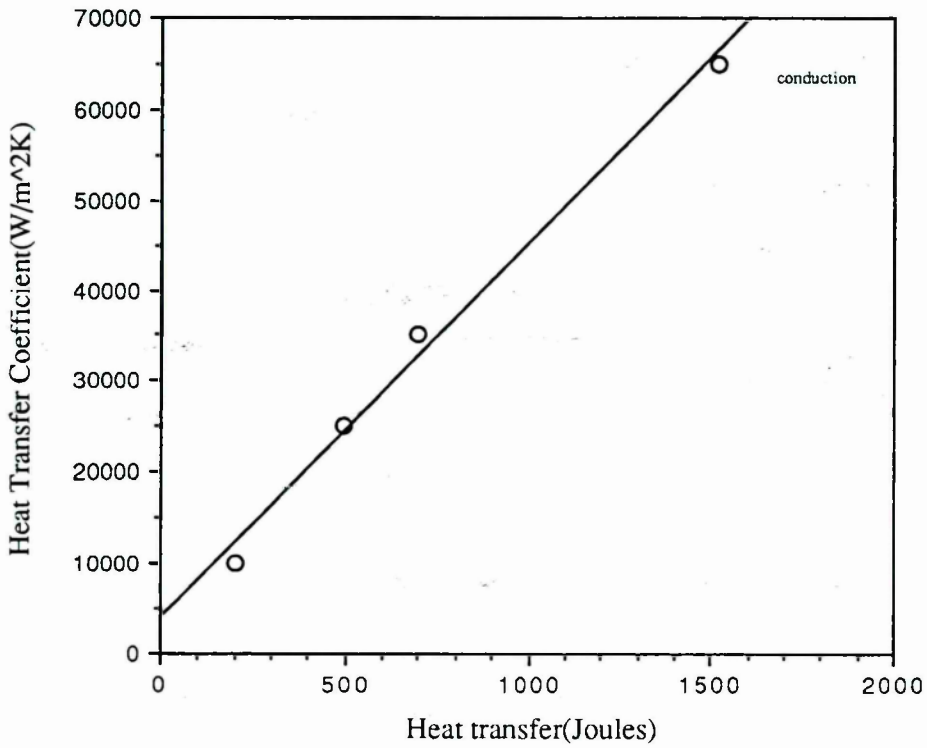

Figure 9.6 Heat transfer by convection and conduction at different h_i.

Chapter 10

Results and Discussion of Strip Formation

10.1 Heat transfer dominant strip formation

The thickness determination by combined heat transfer was explained in chapter 2. Thickness is a function of heat transfer coefficient and the time of liquid metal contact with wheel. A finite difference computer programme was used to simulate the temperature distribution through the thickness of the strip. Interface temperatures were calculated for possible different heat transfer conditions. The heat transfer model suggested and developed by Gaspar(1986) assumes liquid metal in contact with chiller is at solidification temperature. In this work, this model was used to calculate the thickness associated with heat transfer. Finite difference results show that, for the equilibrium solidification range of stainless steel, cooling curves are continuous and no temperature arrest is apparent. The computed wheel/strip interface temperatures were also show continuous decay for a constant empirical heat transfer coefficient. Theoretically, if oxidation on the surface leads to poor strip/wheel contact and a low heat transfer coefficient, the temperature of the pool in contact with the wheel might be above liquidus. Traces of copper detected on the wheel side of the strip surface supports this hypothesis. This may be due to erosion by liquid metal on the wheel surface.

Through thickness temperatures calculated by finite difference computations were used to predict the value of heat flux near to the wheel side in the strip 1/5 thickness away from boundary. This heat flow by conduction is set to equal to heat transfer by convection at the boundary. Assuming there is no temperature gradient inside the chiller interface, interface temperatures were calculated. In fact interface temperatures also vary with time. For the simplicity of calculations, interface temperatures were assumed constant for each different heat transfer coefficient. For a strip casting at $1580°C$, for possible heat transfer coefficients $3.5 \times 10^4, 4.5 \times 10^4$ and $5.5 \times 10^4 W/m^2K$ the calculated interface temperatures are about 1120-1198$°C$. The thickness associated with conduction within the thermal boundary for the residence time of the mushy liquid(0.005 sec) was calculated according to two different cases;

1) Interface temperatures is the solidus temperature (T_m) derived from finite difference results.

2) Interface temperatures are the casting temperatures owing to the massive heat flux toward the pool in melt overflow.

The heat transfer coefficients were also calculated by an iterative technique substituting the experimental thickness to the equation derived by solving the positive root of equation 2.51 which represents the thickness formation within the residence time of liquid pool on the chiller which is nearly equal to 1/3 dwell time of strip(measured on the photographs) before it takes off (total residence time of strip is nearly 0.02 sec for a wheel speed 2.73 m/sec).

These results showed that thickness formation by conductive heat transfer is heat transfer coefficient dependent and thicknesses based on this model are close to experimental values, (see Figure 10.1).

10.2 Momentum Transfer limited Model

Assuming the liquid metal dragged out of melt pool is not solidified until it reaches its limiting value the liquid metal limiting thickness was calculated

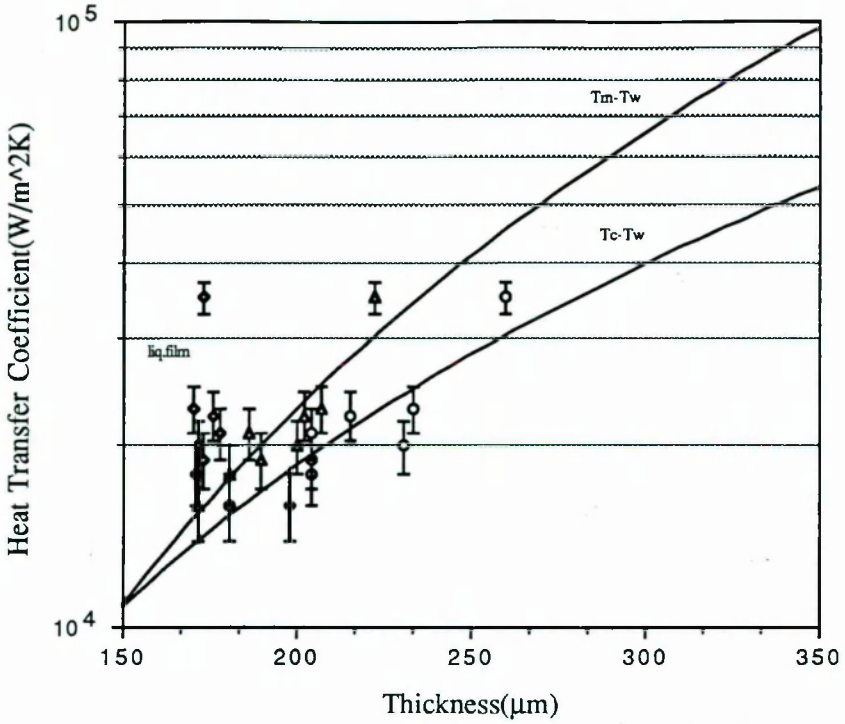

Figure 10.1 Thickness associated with heat transfer.

using the data produced by melt overflow experiments carried out using 304 stainless steel alloy as test material. The capillary number (which represents the ratio of surface tension forces to viscous forces) controls the thickness formation of the liquid film. The calculated values of capillary number for this study are shown in Figure 10.2. The lower curve represents the values calculated assuming equilibrium viscosity data. The higher experimental thickness values at the left hand side of graph for low capillary numbers originates due to low wheel speeds. Therefore a question arises here whether the undercooled viscosity values are high enough to lead the high numerical thickness values from equation 2.13. or thermal field contribution plays role in the boundary layer leading to a solidified layer on the wheel and liquid layer dragged out on top of it.

The thickness values calculated are about 190-170 μm for equilibrium viscosity values from equation 2.13. The viscosity values were estimated from the literature data published by Morita and Iida(1981). The viscosity of liquid iron based alloy is sensitive to impurity content. Frohberg and

Cakici reported that the addition of 0.05 percent sulphur lowers the viscosity 20 percent.

The surface tension values in capillary numbers were measured as described in previous chapter. The results of this study showed that experiments carried out using high sulphur content alloys yielded thin serrated edge strips. The side view photography showed that at low wheel speeds such as 1.4 and 1.7 m.s^{-1} liquid metal level and pool length were large (13mm, i.e the distance at which liquid metal stays in contact with chill surface). This may results in thermal boundary layer formation at lower wheel speed. Therefore it reduces the temperature of the liquid of meniscus and increases viscosity drastically and capillary number.

It has been suggested by Sun and Davies(1987) that thermal transport contribution in thickness formation becomes significant for heat transfer coefficients h$\gg 10^4 W.m^{-2}K^{-1}$ and the proportion increases from 50% at $10^5 Wm^{-2}K^{-1}$ to 80% at $10^6 Wm^{-2}K^{-1}$ for $Fe_{80}P_{13}C_7$ alloy. This is thought to cover the typical range of h that pertains in melt spinning for a number of alloy systems. Since the melt overflow experiments were carried out under air, oxidation on the liquid metal pool in contact with the wheel most likely reduces the heat transfer conditions leading to poor contact between strip and wheel. As a result of this, heat transfer coefficient varies. The solidified layer within the melt pool during the latent heat releasing stage (recalescence) may drag liquid from melt pool. So strip leaving the melt pool may not be completely solidified. For some conditions thickness formation is momentum transfer controlled especially if casting temperature and superheat is high.

Another consideration which supports the proposal is that liquid film thickness calculations are in good agrement with experimental thickness values. Also there is good agreement with Gutierrez's computed streamline pattern and temperature field in the meniscus connected to the strip coming out of meniscus presented in Figure 2.4 and Figure 9.4 of the presented study. As a result strip leaving melt pool during melt overflow is probably in mushy state and completes solidification further to the end of residence

distance which is approximately twice the melt pool length. The liquid thickness calculated for capillary numbers such as 0.008-0.009 are in good agreement with experimental thickness values.

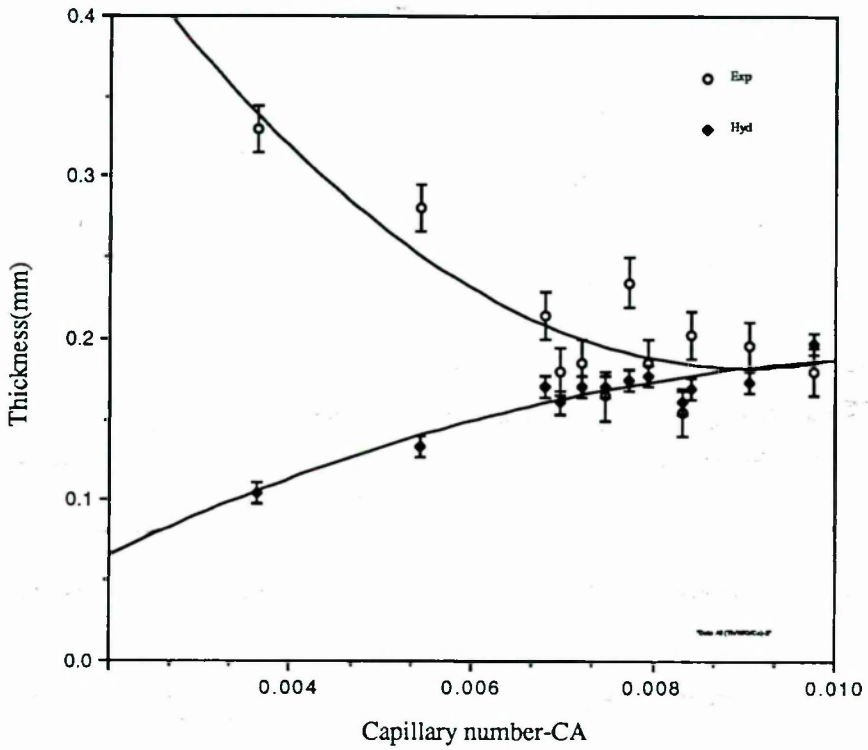

Figure 10.2 Experimental thicknesses(Exp) and calculated liquid film thickness(Hyd)

10.3 General remarks on strip formation

The mechanism of strip solidification was studied by correlating analytic and numerical values with experimental data. Experimental free surface temperatures (Figure 9.3 and 9.5) suggest that liquid in the melt pool is dragged out and the temperature of this zone is above the solidus temperature. This results supports the proposal that thickness formation is momentum transfer

controlled and liquid might be in a mushy or undercooled state. Calculation of the undercooled viscosity by an iterative technique was attempted entering experimental thickness value into equation 2.13. Calculated undercooled viscosities corresponding thickness values are 0.0076 N.$sec.m^{-2}$ and 0.0072 N.$sec.m^{-2}$ for thickness values 225μm and 211μm.

The displacement thickness was calculated from equation 2.35 is 140μm for liquid pool length(measured on the photographs)=20 mm, wheel speed=2.73 msec^{-1}, liquid stainless steel density=7200 kgm^{-3} and maximum viscosity calculated (from limiting film thickness equation(2.13) assuming the strip staying on the chiller is liquid)=0.0076 N.$sec.m^{-2}$. Substituting equilibrium viscosity values reported by Morita and Iida(1981) into equation 2.32, the displacement thickness for liquid steel is about 127 μm assuming the same casting conditions. Experimental thickness values corresponding to the same casting conditions is about 195 μm. The displacement thickness calculated from equation 2.35 proposed by Katgerman(1983) for strip thickness prediction does not include the surface tension and liquid dynamic pressure effects. Therefore the displacement thicknesses calculated from equation 2.35 are less than the thicknesses measured.

Chapter 11

Investigations into Solidification Microstructures

11.1 Introduction

The purpose of this chapter is to investigate and explain the as- cast microstructures of a stainless steel strips produced by the melt overflow technique. Since the primary goal is to produce strip from liquid melt pool in large quantities with uniform dimensions, microstructural control is of secondary importance but remains a crucial aspect of strip casting. Since the as cast microstructure is dependent on thickness and cooling rate plus solidification behaviour of particular composition, process parameters and meniscus characteristics, additional effort has to be made to control composition. For rapid solidification of iron base alloys a knowledge of the crystallization of phases such as delta ferrite, ferrite and austenite depending on the cooling rate and composition is necessary.

Dendrite arm spacing as a microstructure refinement parameter is inversely proportional to the local average cooling rate. Compositional uniformity can be achieved by annealing. Eliminating of segregation is more easily for the microstructures consisted of small secondary dendrite arm spacings.

In this section the results related to the microstructures of as cast 304 stainless strips are presented. Solidification mode characteristics such as

dendrite arm spacings and cell size were used by many investigators to predict the heat transfer coefficient across the wheel/strip interface. To reveal a correlation between the cooling rate attained during strip casting and secondary dendrite arm spacings is not the most appropriate technique to understand actual solidification. Because of "ripening" of secondary dendrite arms during liquid/solid interface motion an approximate relation between these parameters can be assumed. The rate of solidification predicted by this technique was compared to the calculated heat transfer by analytical and numerical methods presented in Chapter 4. In the following sections dendrite arm spacings measured of the experiments will be presented and discussed, then a rate of solidification will be predicted comparing literature data and the dendrite arm spacings measured.

The microstructures examined by TEM revealed interdendritic delta ferrite among austenite dendrites in some strips. Delta ferrite is a metastable phase that exists in 18 Cr-8 Ni stainless steels at high temperatures which is supposed to transform into austenite during cooling. The existance of this phase and results of TEM investigations will be discussed in this section. At a finer scale defects such as dislocations which may appear as grain boundary ledges and fault pairs were observed. The defects may originate from thermal stresses due to the high solidification rate. TEM photographs of these defects are also presented in this section.

11.2 Interpretation of Microstructures

In this work an austenitic stainless steel(18Cr-8Ni) strips were produced in various thickness 165-360 μm. Figure 11.1 shows that as cast microstructures was consisted of first nucleation start regions on the wheel side where plane front stabilization occurs then fine cellular structures and finally toward the free surface, fully developed dendritic structures can be seen. On the wheel side where nucleation starts some large equiaxed region in regular and irregular intervals were observed. Optical microscopy revealed that this equiaxed region were consisted of very fine cellular structure which can

be distinguished by polarized light condition. Dendrites radially originated from equiaxed nucleation sites reached the free surface as fully cellular or dendritic structures. The proportion of cellular structures were found to be very high for thick strips such as 350 μm thick. This may be due to the stabilization of cellular structure at low cooling rate. Secondary dendrite arm spacings measured on the through thickness of as cast strips which were 185 μm thick are in range of 1-4 μm. A direct positive relation can be derived by measuring the secondary dendrite arm spacings and plotting against thickness. This shows that dendrite arm spacings are cooling rate and thickness dependent parameters. This can be seen in Figure 11.2. The through thickness section photographs in Figure 11.1 consisted of non dendritic, cellular and dendritic regions which is consistent with the thermal gradient predictions presented in Chapter 9. The formation sequence of this solidification structures are both related to thermal gradient and undercooling of liquid/solid interface depending on the alloy composition and surface tension which is mentioned in this section. All secondary dendrite arm spacings measurements were carried out at the same through thickness region where secondary arms developed. Average secondary dendrite arm spacings were used to predict the solidification rate experimentally. Although this method is not a very accurate for solidification rate prediction due to "ripening", the solidification rate can approximately be estimated. The estimated values of the solidification rate is about almost 10^4 $^\circ C/$sec for thickness range of 200 μm. The rate of solidification during rapid solidification of stainless steels is not uniform since there are solidification mode transitions such as transition from plane front to cellular and cellular to dendritic later on.

Through thickness temperature calculations of solidifiying 304 stainless strip performed by finite difference method shows that temperature drop in 0.001 sec is around 75 $^\circ K$ near to strip/wheel interface and 8 $^\circ K$ in a region close to the free surface. There is agreement between the sequence of solidification modes observed in the microstructures of this work and the theory proposed by Abe, Miyazawa and Nakamura(1988) on plane front stabilization at high cooling rates. Some primary stalks of plane front so-

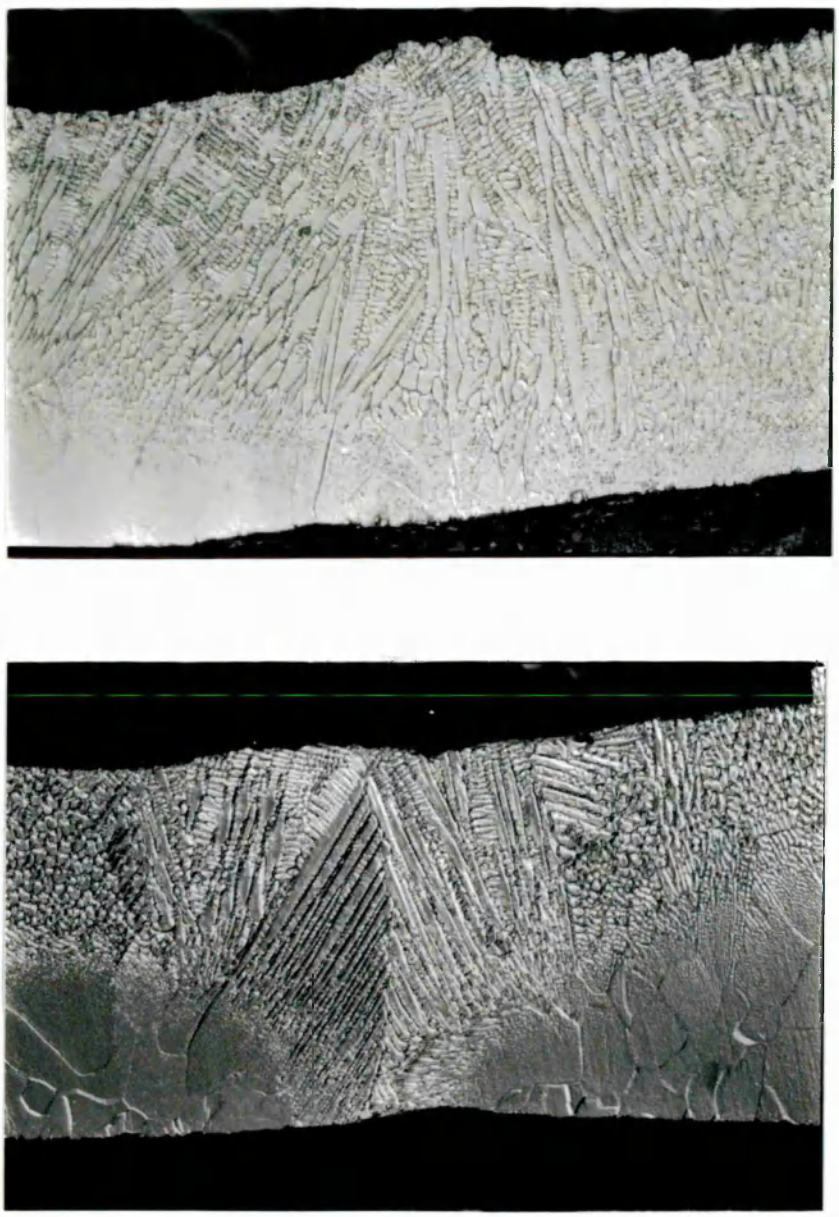

Figure 11.1 Through thickness section of as cast strip.

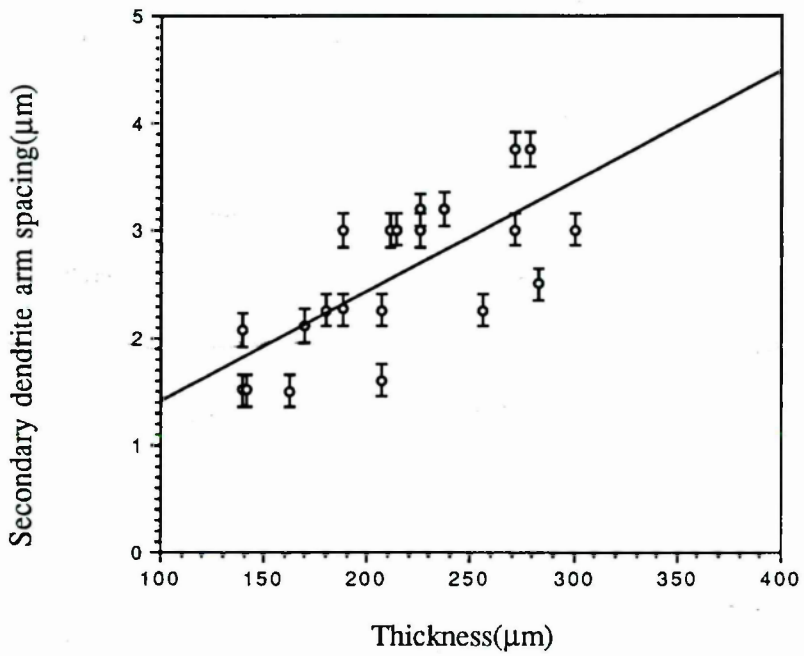

Figure 11.2 Secondary dendrite arm spacings measured through thickness of as cast 304 stainless steel strips.

lidification structutes may even reach to the free surface of the strip. The solidification mode transition can be explained by considering the thermal gradient(G)-solidification rate(R) diagram proposed by Smugeresky(1982). This diagram is given in Figure 11.3. Thermal gradient is high at the first time period of liquid strip in contact with chiller, and G/R ratio is greater than 2. So planar interface is stable until to G/R ratio is lower than 2. For G/R ratio between 2 and 1/2 cellular structure is stable where the gradient is lower. Finally, dendritic structures develop at G/R ratio less than 1/2 where thermal gradient is low and solidification rate is high. This sequence has been observed in the microstructures of as cast strips and there is a good agreement with Smugeresky's proposal.

11.2.1 Solidification Mode

The theoretical background information is given in this section to explain the conditions of formation of dendritic, cellular and plane front structures revealed after examinations of microstructures of as cast strips. The solidification mode is classified by the crystal growth rate and the thermal gradient in the liquid phase with increasing crystal growth rate the solidification mode changes schematically from plain front to cellular, dendritic, cellular again and finally to plain-front at a growth rate known as the absolute stability limit. The condition for the transition is expressed by the following equations proposed by Abe, Miyazawa and Nakamura(1988).

1) A planar interface can be obtained in two different conditions : either at low growth rates according to the constitutional supercooling theory, or at very high growth rates because the front is stabilized by the surface tension σ_{LV}; this second case is called absolute stability. Condition for plane front solidification at low crystal growth rate(V_c) can be written as;

$$V_c \leq \frac{DG_l}{\Delta T_0} \tag{11.1}$$

2) When unstability occurs, the alloying elements segregate to form solidification cells or dendrites. The cell walls are usually decorated by precipitates, Fayard, Duflos and Lasalmonie(1985). Condition for transition from cellular

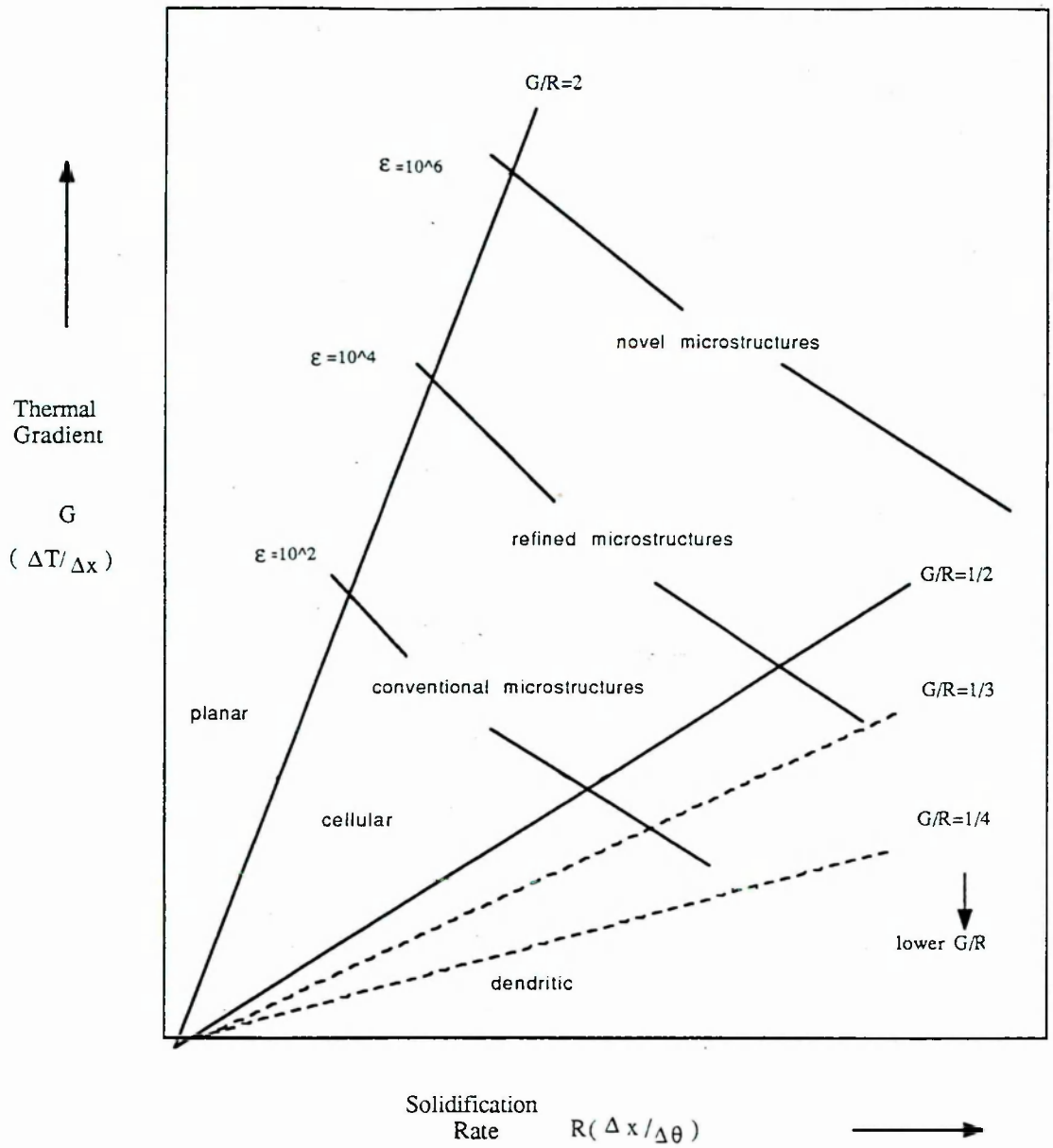

Figure 11.3 Schematic relationship between the cooling rate(ε), The thermal gradient(G) and the solidification rate(R), Smugeresky(1982).

to dendritic solidification is;

$$V_c = \frac{2DG_l}{\Delta T_0} \tag{11.2}$$

3) Condition for plane-front solidification at high growth rate (absolute stability limit)

$$V_c \geq \frac{\Delta T_0 D}{k_0 \Gamma} \tag{11.3}$$

where ΔT_0 is the range of solidification temperature which can be defined as; $\Delta T_0 = \frac{m_1 C_0[k_0-1]}{k_0}$, Γ= Gibbs-Thomson coefficient($\frac{\sigma}{\Delta S_v}$), S_v is volumetric entropy of fusion, k_0 is equilibrium distribution coefficient, m_1 liquidus slope, C_0 solute concentration in liquid, G_l is temperature gradient in liquid, D is diffusion coefficient in liquid. Cooling rates in range 10^2 to 10^4 $^\circ C/$sec were reported as typical observed cooling rates in melt drag and melt overflow processes. The high solidification speed achieved in this range is enough to eliminate secondary dendrite arms in most alloys to give a cellular structure with a spacing one order of magnitude smaller than in the case of a massive casting solidified against a chill were reported by Hubert, Mollard and Lux(1973).

11.2.2 Dendritic Solidification

The dendrite arm spacings measured on the through thickness section of the as cast strips were found to be in the range of 1.5 to 4 μm for corresponding thickness range of 150 to 300 μm. In this section solidification time of the 304 stainless steel strip on a moving chiller is discussed. Essadiqi and Masounave(1987) predicted the solidification time of 304 stainless steel from secondary dendrite arm equation which is given in this chapter(equation 11.16). Using the same equation a solidification time for the strip produced by melt overflow was calculated as 0.02 sec. This is very close to the residence time calculated from photographs as 0.017 sec(or 46 mm residence distance). This agreement confirms the hypothesis "Strip solidifiying on the chiller is mushy and solidification is completed just before the strip leaves the chiller".

Solidification processes involving dendritic solidification are carried out commercially over a range of cooling rates of almost 15 orders of magni-

tude from 10^{-6} K/sec for large ingots to nearly 10^{9} K/sec for surface treatments. Dendrite tip velocities, or isotherm velocities, range from as little as 10^{-5}cm/sec to as much as 10^{4}cm/sec. The results published by Jones(1978) lists examples of the various solidification processes and their respective regimes of cooling rates. At relatively slow rates of solidification of castings and ingots, nucleation generally occurs with little or no undercooling. It has been long known experimentally that dendrite tips grow into the melt with little undercooling so that dendrite tip is equal to liquidus temperature of alloy. With rapid infinite interface kinetics, uniform interdendritic liquid, and constant partition ratio, k, the microsegregation which results from the dendritic growth is then described by widely used "local solute distribution" equation, often referred to as Scheil equation as;

$$C_s^* = kC_0\,(1 - f_s)^{k-1} \tag{11.4}$$

where C_s^* is the composition of the isoconcentrates surrounding, f_s is fraction solid both during and after solidification and C_0 is the initial fraction liquid. The Scheil equation almost always predicts more microsegregation than is observed experimentally and this is due to three factors; one is diffusion in the solid; a second, more important is "ripening" of secondary dendrite arms, i.e, the dissolution of small dendrite arms during solidification and the consequent more rapid growth of larger arms. A third factor reducing extent of microsegregation is "temperature gradient migration" of arms (the dissolution and reprecipitation of solid as a result of improved temperature gradient, Allen and Hunt(1979). If dendrites are grown slowly but with a steep temperature gradient, as in a crystal growing furnace, dendrite tip temperature no longer remains near the liquidus temperature but is depressed as a result of solute diffusion down the concentration gradient from behind the dendrite tips. The dendrite tip temperature can be given by the simple relation proposed by Flemings(1974).

$$\Delta T = \frac{DG}{R} \tag{11.5}$$

where is tip undercooling, G is temperature gradient, and R is growth rate (dendrite tip growth velocity). Equation is valid only up to a tip undercool-

ing (ΔT) equals to the temperature range between the liquidus and solidus. At this undercooling, the constitutional supercooling becomes criterion for plane front growth. The solute diffusion down the thermal gradient, modifies the Scheil equation and the new "local solute redistribution equation" becomes

$$C_0^* = kC_0\left(\frac{a}{k-1} + \left(1 - \frac{ak}{k-1}\right)\right)(1-f_s)^{k-1} \tag{11.6}$$

where a=-$\frac{DG}{mRC_0}$, and m=liquidus slope, k is partition ratio

11.2.3 Dendrite arm spacing

It has been known for over twenty years that increasing the rate of solidification reduces dendrite arm spacing arm spacing. For dendrites of all non-faceting metallic alloys dendrite arm spacing described by Flemings(1981) as;

$$d_2 = a\dot{\varepsilon}^{-n} \tag{11.7}$$

where d_2 is secondary dendrite arm spacing, $\dot{\varepsilon}$ is cooling rate($\frac{dT}{d\theta}$) and a and n are constant; n is usually about $1/3$ as would be expected from the "ripening" mechanism that controls the secondary dendrite arm spacing. When solidification is by columnar grains primary dendrite arm can be measured and this is found experimentally in usual castings and ingot to follow a relationship similar to equation 11.7 but with a slightly higher exponent generally n approaches $1/2$.

In recent years a reasonable semi-quantitative model for the formation of spacing has been developed. The method employed by some investigators involves the tip curvature required at the dendrite tip by surface tension and diffusional requirements to that required at the back of the tip so as to satisfy solute conservation according to equations 11.4 or 11.6. Hunt(1979) has analyzed dendrite parameter using the spherical cap approximation and Wasson(1978) carried out the analysis using the Trivedi parabolic tip approximation. Both workers employed the minimum undercooling principle to choose tip curvature; The equation developed by Wasson(1978) is;

$$d_1 = 4.76\left(\frac{T_M\sigma_{LV}}{L_V}\right)^{0.26} G^{-0.5}\left(\frac{m[1-k]DC_0'}{R}\right)^{0.24} \tag{11.8}$$

where d_1=primary dendrite arm spacing, L_V is volumetric heat of fusion, G is thermal gradient, σ_{LV}=liquid surface tension and T_m is melting temperature;

$$C_0' = C_0 + \frac{k}{1-k}\frac{DG}{mR} \tag{11.9}$$

For high values of the metal-mold heat transfer coefficient, a simple substitution of $\dot{\varepsilon}$=G.R in equation 11.8 yields a relation of the form;

$$d_1 = a\dot{\varepsilon}^{-n} \tag{11.10}$$

where n=3/8, a is a constant and $\dot{\varepsilon}$ is cooling rate. Kattamis and Flemings(1966) studied iron and nickel-based alloys, achieved undercoolings of $300°K$ and for stainless steel 316 undercooling of $475°K$ and $\Delta T/T_L$=0.28 were reported by Mac Isaac(1983). As undercooling is increased, the dendritic morphology tends to become simpler, and ultimately quite cylindrical as a critical undercooling of $170°K$ is approached. The grain size is not effected by undercooling up to this point, although the dendrite arm spacing is somewhat reduced. It has been reported by Flemings(1983) that rapid heat extraction greatly reduces the dendrite arm spacing of the dendritic samples and the grain size of the highly undercooled samples. It can be understood that "coarsening" or "ripening" has a major effect on the morphologies observed, and it seems reasonable to conjecture that the transition from a coarse dendritic structure to a fine spherical structure is not the result of enhanced nucleation but the result of ripening or dendrite remelting. This proposal explains the formation of very fine cellular structure in the nucleation zone at the wheel side of 304 stainless steel strips investigated in this work and given in Figure 11.1. Mac Isaac et al(1983) reported the structure of type 316 stainless steel (which contains phosphorous) droplets which were undercooled $475°K$ or 0.28 T_L in a glass matrix. Second dendrite arm spacings of austenitic 304 stainless steel were investigated by many investigators such as Esaka(1988), Sugiyama et al (1974), Wolf(1986), Kasama et al (1987). The relationship between the secondary dendrite arm spacing and the average cooling rate for austenitic stainless steel is shown in Figure 11.4. Secondary dendrite arm spacings in steels

have been the subject at numerous studies, Polich and Flemings(1965), Ibaraki, Okamoto and Matsumoto(1968), Suzuki, Nagaoka and Iwata(1968), Suzuki and Nagoka(1969), Gungi, Kusaka, Ishikawa and Sudo(1974), Jacobi and Schwerdfeger(1976), Edwardson, Frederiksson and Svenson(1976), Taha, Jacobi, Imaqumbai and Schwerdtfeger(1982), Taha(1986), the majority of which were steady state unidirectional solidification experiments. The solidification variables, growth rate (R) and temperature gradient (G) may vary independently and the following empirical relationship is proposed for d_2 secondary dendrite arm spacing, Polich and Flemings(1965);

$$d_2 = kR^m G^n \tag{11.11}$$

the exponents m and n are usually found to be similar for secondary dendrite arm spacing measurements, their values being close to 0.4 for low carbon steels, Jacobian and Schwerdtfeger(1976), Edvardsson, Fredriksson and Svensson(1976), Taha, Jacobi and Magumbai(1982). It is also normal to relate the dendrite arm spacings to local solidification time (θ_f), the suggestion of Flemings(1966) where θ_f is the freezing temperature difference between the liquidus and solidus divided by the cooling rate.

$$\theta_f = \frac{T_l - T_s}{R.G} \tag{11.12}$$

where T_l is the liquidus temperature and T_s is the solidus temperature. Secondary dendrite arm spacings are reported by Cramb(1988) as the following relation;

$$d_2 = L\theta_f^r \tag{11.13}$$

Kattamis and Flemings(1965) considered secondary dendrite arm spacing to be a coarsening phenomena, similar to Oswald ripening and showed theoretically that the exponent r should be 0.33. Actual results of other investigators have ranged from 0.17 to 0.55 with most recent results for lower carbon steels being 0.44 reported in a quide to the solidification of steels (Jerkontoret(1977)). The parabolic freezing law is to be a close approximation to actual results for most slab or strip casters. Kasama(1987) has shown that for very thin strips (<0.05 mm in stainless steel) this law is not exact and

has to be modified to take into account contact resistance. In this strip casting, the cooling rate in $C°/\text{min}$ is often quoted as a measure of rapid solidification. For carbon steels the data produced by Suzuki et al (1968) analyzed and reported secondary dendrite arm spacing and growth rate as;

$$d_2 = 710 \quad R^{-0.39} \tag{11.14}$$

growth rate were also reported as for low carbon steels

$$R = 7069 \quad x^{-1.71} \tag{11.15}$$

where x is thickness measured in mm and x>0.1mm. Masounave and co workers(1988) reported that for 304 stainless steel cast on a moving chiller, the relationship between the secondary dendrite arm spacing and solidification time is expressed as follows, Essadiqi and Masounave(1987).

$$d_2 = 15.42 \quad \theta_f^{0.347} \tag{11.16}$$

The solidification times corresponding to 4 and 12 μm are 0.02 and 0.48 sec respectively.

11.3 Composition analysis of as cast microstructures

Intercellular delta ferrite cores were observed in the microstructures of 304 stainless steel strip investigated in this work by transmission microscopy. Figure 11.4 shows delta ferrite within two austenite grains. The compositions of interdendritic and primary dendrite arm regions of as cast 304 stainless steel strips which is given in Figure 11.4 were analyzed and results are given below as wt%; Dark interdendritic region (δ-ferrite);

Fe:71.56, Ni:8.75, Cr:19.26, Al:0.00, Si:0.433

White primary arm regions (γ-austenite);

Fe:68.94, Ni:8.83, Cr:20.89, Al:0.19, Si:1.16

Nucleation start region at the wheel side (large equiaxed grains of primary high Cr austenite);

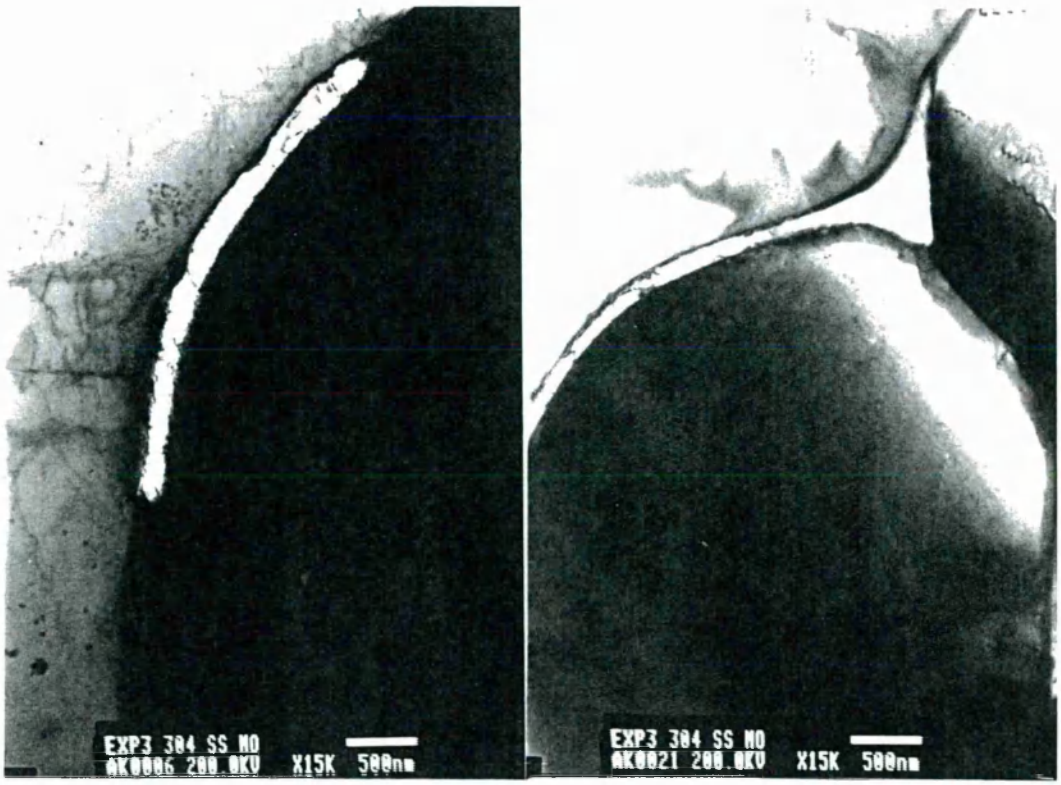

Figure 11.4 Delta ferrite skeleton within austenite dendrite arms.

Fe:70.47, Ni:9.02, Cr:19.97, Al:0.00, Si:0.54

For single roller casting of 304 stainless steel composition Love and Nauman(1988) reported that microstructure of strip consisted of three different regions:

A-darkened grains with dendritic cored internal structure

Fe 71.62, Cr 18.86, Ni 8.88, Si 0.64.(low chrome austenite)

B-light grain with uniform shading no evidance of dendritic growing Fe 71.31, Cr 19.54, Ni 8.36, Si 0.78.(high chrome austenite)

C-dark grain boundaries

Fe 71.34, Cr 23.81, Ni 4.85 (ferrite core)

for about thickness in range of 1.03-0.81 mm. Slight chromium deficiency in the interdendritic regions yielded the formation of delta ferrite according to Schaeffler diagram shown in Figure 11.5 due to the rest of liquid composition is shifted to the austenite+delta ferrite duplex region yielding interdendritic delta ferrite. The background information about the solidification and the formation of phases at different compositions for metastable

stainless steel solidification are presented in the following section.

11.3.1 Solidification Characteristics Structure and Phase Stability of 18Cr-8Ni Stainless Steel

In this section background information is given about the composition dependence of formation of phases may exist in rapidly solidified 304 stainless steel. Generally stainless steels can be divided into major three categories depending upon the matrix phase (austenite-fcc, ferrite-bcc and martensite-bct). The phase fields of these alloys are first represented by Schaeffler diagram modified by Scheider(1986) which is shown in Figure 11.5. The diagram was originally derived for welding process problems associated with stainless steels but represents a good dimensional method to predict the possible resultant phases depending upon the effect of alloying elements. The equivalent axes are given by;

$$Cr-eq = Cr+2(Si)+1.5(Mo)+5(V)+5.5(Al)+1.75(Nb)+1.5(Ti)+0.75(W) \quad (11.17)$$

$$Ni-eq = Ni+Co+0.5(Mn)+0.3(Cu)+25(N)+30(C) \quad (11.18)$$

The brackets represent the weight percent in solution in the alloy. Although the diagram predicts the quenched phases some investigators reported additional considerations. Fredriksson and Stjerndahl(1982) repoted that segregation ratio increases with increasing cooling rate. Their considerations indicated that back diffusion during solidifications is of major importance during ferrite solidification. In stainless steels a transition from a peritectic to a eutectic reaction occurs, Fredriksson(1972) at intermediate cooling rates. In many Fe-Cr-Ni steels such as 18Cr-8Ni stainless steels the solidification starts with a primary precipitation of austenite. During this reaction the ferrite is isolated from liquid. It is well understood that large undercoolings are obtainable by rapid solidification techniques and the high temperature δ-ferrite formation is suppressed or the rapid solid state quench is still insufficient to prevent the initial δ-ferrite transforming to austenite, Bee and

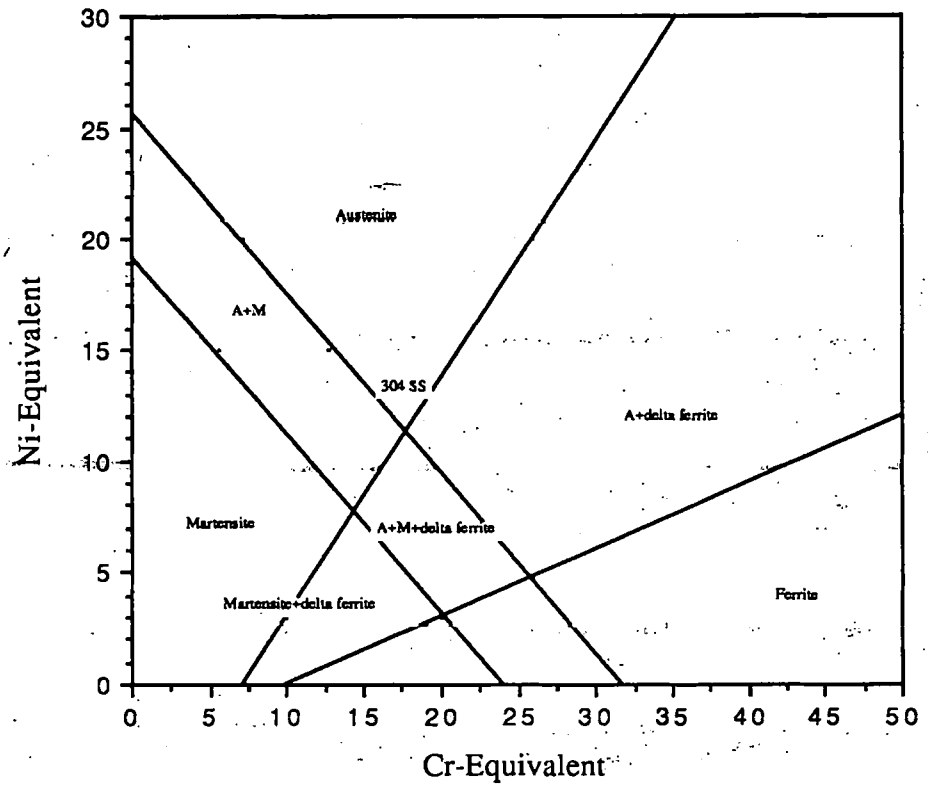

Figure 11.5 Schaeffler diagram modified by Scheider(1986).

Wood (1982). Some observations by Fredriksson(1972) demostrated that nitrogen may have a very strong effect and primary formation of δ-ferrite in 18Cr-8Ni steel is favoured by high rate of solidification where as primary formation of austenite is favored by high nitrogen content. Birat and coworkers reported that 304 stainless steel strips produced by twin roll caster consisted of primary austenite dendrites instead of primary ferrite as is usually the case for slabs of the same composition. Austenitic primary stalks whereas the globular grains, which have been formed by slower growth in the liquid pool have an α- ferrite dendritic network. The interpretation is related to the dependance on solidification rate of the dendrite tip remelting which is higher for ferrite than for austenite at high rates, Bobadilla and Lacaze(1988). Some authors also reported that if crystals are allowed to dwell in the liquid pool longer than the contact time on the wheel, large grains form. Love and Nauman(1988) reported that in general, the solidification of an 18Cr-8Ni stainless steel passes from liquid through a ferrite+liquid region, through an entirely ferritic region, and through a solid-solid transformation to form austenite. The solidified structure should have dendrites of austenite with intercellular δ-ferrite cores, Dean(1988). Due to the rapid, non-equilibrium cooling of the liquid metal, a metastable primary austenite appeared to form. Region which was relatively high in nickel was more austenitic than region which was ferritic and higher in chromium and lower in nickel.

At high cooling rates such as $10^5 - 10^6\ ^\circ C/\text{sec}$, microstructures of rapidly solidified steels can be explained by using Schaeffler diagram. Johnson and co-workers(to be published) reported that using Moassbauer spectroscopy it has been observed that rapid solidification suppresses the martensite start (M_s) temperature, and stabilize austenite at low Cr concentrations but it also inhibits diffusion assisted formation of ferrite at higher Cr concentrations. As a whole, rapid solidification leads to a shift of the austenite minimum in the Schaeffler diagram towards lower Ni and higher Cr concentrations, and at the same time the duplex fields become narrower. Application of the Schaeffler diagram to rapidly solidified stainless steels therefore

necessitates certain changes which particularly depend on the Cr content. Johnson and co-workers reported that at low Cr concentrations M_s is suppressed and the austenite/martensite two phase field is narrowed. At higher Cr concentrations where diffusion assisted ferrite formation is inhibited, the austenite/ferrite boundary is considerably lowered. As a whole, rapid solidification leads to a general lowering of the phase boundaries towards lower Ni content. At the same time the austenite minimum is shifted to a Cr concentration 20-22 wt percent.

Chapter 12

Summary

The primary objective of this thesis is verification of direct continuous casting of high melting point alloy strip. In order to acheive this objective a laboratory scale melt overflow furnace which has a capacity of 5 kg stainless steel was developed. The heat transfer conditions were found to be critical in the pouring channel refractory, (Figure 8.1). This work verified and conformed that with this pouring channel geometry and sillimanite refractory 304 stainless steel strips can be produced. But experiments revealed that uniform strips with good edges can be produced for only when both the casting speed and the surface tension of alloy are controlled. The thickness of stainless steel strips are about 200 μm for a wheel speed 2.73 m/sec.

In this thesis the strip formation on the rotary chiller was modelled using momentum transfer, casting instability and heat transport equations. The effect of material properties and casting conditions on final strip edge quality were thoroughly investigated and very good agreement was observed between capillary wave instability theory which explains the effects of liquid material properties and process parameters on the edge characteristics of the strips presented in chapter 3, and the modelling experiments results presented in Figure 8.2.

Experiments with materials possessing high surface tension values such as 2.2 Nm^{-1}-2.4 Nm^{-1} showed that strip casting with this technique is not possible. The liquid dynamic pressure should exceed the surface tension of the alloy or momentum should be sufficient enough to drag the liquid from

the melt pool against surface tension forces(equation 2.33).

The free surface photographs and temperature calibrated photograph results (Figure 9.2 and 9.4) revealed the existance of mushy liquid dragging out of melt pool.

Assuming the strip dragging out of melt pool was liquid, equation 2.13 was used to predict the liquid film thickness substituting the surface tension values measured by a modified oscillation droplet technique and viscosity values estimated from the data of Morita and Iida (1981).

The meniscus of liquid film formation was photographed (Figure 8.4) and the radius of free surface curvature measured is about 15 mm. This result is further evidence of liquid dragging out of melt pool. If the strip leaves the melt pool as solid proposed by Gaspar(1986) the radius of free surface curvature is intersected by a straight line which corresponds to the free surface of solidified strip. This was not observed during most of the experiments.

Experiments carried out using materials possessing different surface tension values revealed that strip edge serrations occurred at low surface tension values and negative $\triangle V$ which is further evidence of the existance of a mushy liquid zone. The velocity difference $\triangle V$ between the minimum stream velocity which is given in equation 3.7 and the experimental melt delivery speed was found to be an effective parameter for predicting good strip production. The strips with positive $\triangle V$ (Figure 8.2) have good edge quality. On the contrary strips with negative $\triangle V$ have edge serrations as a result of capillary wave instability. The effectiveness of instability waves on the surface and edge of the strip is related to whether the strip is liquid, solid or mushy when it leaves the melt pool. If the strip leaves the melt pool as solid, or liquid which has sufficiently high surface tension, instability waves do not result in edge serrations. Since the skin of liquid of low surface tension and mushy strip is not strong enough to prevent instabilities, capillary waves reach the surface resulting in edge serrations.

The thicknesses associated with heat transfer in equation 2.52 were used to verify the experimental strip thickness forming within the residence time

of the mushy liquid measured on the photographs.

Free surface temperature calibrated photographs revealed that the strip reaches the solidification temperature zone before it leaves the chiller, (Figure 9.4 and 9.5).

The residence time of this mushy liquid is slightly less than the time of liquid metal contact to the chiller(0.005 sec), which is the maximum time which can be assumed to calculate the thickness associated with heat transfer, Gaspar(1986). Gaspar et al suggested that strip formation is heat transport controlled only and develops in the thermal boundary layer which exists in the liquid pool in contact with chiller. But Figures 9.2 and 9.4 show the existance of a mushy liquid and Figure 8.2 confirms the effect of capillary waves on the mushy strip as edge serrations. So the thickness associated with heat transfer should be calculated for the residence time of mushy zone instead of residence time of the liquid pool in contact with the chiller.

Both the liquid film thickness predicted and the thickness associated with heat transfer calculations for the mushy zone are very close to the experimental thicknesses measured for a wheel speed of 2.73 m/sec.

The heat released to the chiller/wheel interface by conduction through its thickness, and radiation from the free surface, was modelled considering the strip dragging out of the melt pool to be mushy and solidifies at the end of residence zone.

The heat transferred by conduction through the thickness, convection at the wheel/strip interface and radiation at the free surface were calculated assuming the heat transfer coefficients deduced from the free surface temperature data fitting with calculated free surface temperatures using the finite difference technique, (Figure 9.3).

These results are given in Table 9.1. This table explains that the heat released by conduction and convection is quite close to the latent and superheat released within the total residence time of strip on the chiller. However, the calculations cannot explain the rate of release of latent heat and exact position on the chiller.

Both modelling of the strip formation and experimental results show that strip leaves the melt pool as a mushy liquid and therefore the surface tension of 304 stainless steel alloy should be controlled in the range of 1.9-2.0 N/m to prevent capillary melt instabilities, and their consequent result: edge serrations.

Bibliography

[1] Abe.Y.K, K.Miyazawa and M.Nakamura(1987), *Materials Science and Engineering.* Vol.98, p.351-355.

[2] Abbaschian G.I and S.A.David(eds) (1983), *Proc.Conf on Grain Refinement in Castings and Welds*, Metallurgical Society of AIME, Warrandale, PA. pp87-95.

[3] Adams C.M (1958), *"Thermal Considerations in Freezing" in Liquid Metals and Solidification*, ASM.

[4] Allen B.C (1963), *Trans.AIME* vol.227, p.1175.

[5] Allen B.C (1972), *"Surface Tension of Liquid Metals" in Liquid Metals Chemistry and Physics.* ed. Sylvan Z.Beer.,Marcel Dekker, inc. New York.

[6] Allen B.C and W.D.Kingery (1959), *Trans. AIME* Vol.215, p.30.

[7] Allen.D.J and J.D.Hunt(1979),"*Solidification and Casting of Metals*", The metals Society, Book 192, London.p.39

[8] Anthony T.R and H.E.Cline (1979), *J.Appl.Phys* vol.50, p.245.

[9] Anthony T.R and H.E Cline (1978), *J.Appl.Phys* Vol.49 No2 , p.829.

[10] Batchelor G.K (1970), *Fluid Mechanics* (University Printing House, Cambridge)

[11] Brasmer S(1979), *M.S. Thesis*, Urbana, Illinois. U.S.A.

[12] Bee J.V and J.V.Wood(1982), *Metal Science* Vol.16, p.268.

[13] Belton G.R(1972), *Met.Trans.*, Vol.3, p.1465.

[14] Belton G.R(1976), *Met.Trans.*, Vol.7B, p.35

[15] Bernstein I.M and B.B.Rath(1972), *Surface Science.*, Vol .31, p.101

[16] Bewley B.P and B.Cantor(1986), *Int. Journal of Rapid Solidification* Vol.2 pp.117

[17] Bobadilla M, J.Lacaze and G.Lesoult(1988), *J. of Crystal Growth 89* ."Influence des conditions de solidification sur le deroulement de la solidification des aciers in oxydables austenitiques"., pp.531-544.

[18] Bondi A (1953), *Chem Rev*,Vol.52, p.417

[19] Boulby K and J.V.Wood(1986), *Powder Metall* Vol.29, p.32.

[20] Bower T.F, H.D.Brody and M.C.Flemings(1966), *Trans TMS- AIME*, Vol.236, p.624-634.

[21] Brimacombe O.K and F.Weinberg(1972), *Met.Trans.*, 3. p. 2298

[22] Cantor B and Cheese (1980), *J.Mater.Sci.* Vol.15, pp.2658-2661.

[23] Cantor B (1982), *Rapidly Solidified Amorphous and Crystalline Alloys*, p.317

[24] Chang and Russell (1965), *Phys. Fluids*, Vol.8, pp.1018-1026.

[25] Cherukuru M.K.S(1979), in *Tool Alloy Steels*, " Improvement of cleanness of stainless steels by modified deoxidation". Vol.13.pp.95-100.

[26] Chipman J and K.L.Fetters (1941), *Trans. ASM*, Vol.29, p.953.

[27] Clyne T.W (1983), *Modelling of Casting and Welding Process II* , p.146. ed. Conf.Proc. The Met.Soc.AIME.

[28] Cottrell A.H(1953), *Dislocations and plastic flow in Crystals*, Oxford University Press

[29] Coughlin J.P(1954), *U.S. Bureau of mines Bulletin 542.* "Heats and Free Energies of formation of inorganic Oxides".

[30] Cramb A.W(1988), *"Casting of Near Net Shape Products"*,Ed. Y.Sahai, J.E.Battles, R.S Carbonara, C.E Mobley., The Metallurgical Society.p.673

[31] Crank J(1984), *"Free and Moving Boundary Problems"*, Oxford, Clarendon Press. p.217-282.

[32] Grant, Cummings, Wood and Blackburn(1988), To be published(Metal Powder Report)

[33] Cummings D.L and D.A Blackburn(1988) "report for NPL contact C109247" to be published.

[34] Davies H.A(1985), *Rapidly Quenched Metals* p.101.

[35] Dean D.C(1988), *"The Physical Metallurgy of Cast Type 304 Stainless Steel". Iron and Steel maker.* Vol.15 , pp. 12-15.

[36] Dyson B.F(1963), *Trans.AIME* Vol.227, p.1098.

[37] Dzhemilev N.K, S.I.Polel and B.V.Tsarevskii(1964), *Fiz. Met.i Metallov*, Vol 18(1),p.77. English Transl. 18(3), p.158, English Transl.

[38] Edvardsson T, H.Fredriksson and I.Svensson(1976),*"A study of the solidification process in low-carbon manganese steels", Metal science*,Vol.10., p.298-306.

[39] Elliott J.F(1981), *Metallurgical treatises*, AIME, p.54.

[40] Eremenko V.N,Y.V.Naidich and A.A.Nosonovich(1960),*Zh.Fiz.Khim*, Vol.34(5), p.484. English Transl.

[41] Esaka H et al.,(1988),*"Relation between secondary dendrite arm spacing and cooling rate for 304 stainless steel,"Current advances in materials and process"*, (Report of the ISIJ meeting),vol.1(1), p.268.

[42] Esmail M.N and R.L Hummel(1975), *Chem Eng Sci*, Vol.30, p.1195.

[43] Essadiqi E and J.Masounave(1987),*"Strip casting of 304 stainless steel"* NRCC/IMRI, Boucherville, Quebee, Canada, Report IGM87RT-205-621-R.

[44] Fayard F, F.Duflos and A.Lasalmonie(1985),*"Rapidly Quenched Metals", p.811.*

[45] Flemings M.C(1974), Solidification Processing, *Mc Graw Hill, New York*

[46] Flemings M.C(1981), Metallurgical Treatises, *The Metallurgical Society of AIME. p.291-299*

[47] Flemings M.C(1985) Rapidly Solidified Crystalline Alloys., *Proceedings of TMS-AIME, p.3*

[48] Flemings M.C, T.F.Bower and H.D.Brody(1966), Trans TMS-AIME, *Vol.236.p.624-634.*

[49] Flemings M.C and Y.Shiohara(1984), Materials Science and Engineering. *Vol.65, p.157-170.*

[50] Fisher R.M, H.Hashimoto and J.W Negele(1966), Sixth International Congress for electron microscopy. *Kyoto.*

[51] Fredriksson H(1972), Metall Trans,*Vol 31, p.2989.*

[52] Fredriksson H and J.Stjerndahl(1981), Metal Science., *Vol.16., p.575-585.*

[53] Gaskell D.R(1975), "Applications of Thermodynamics to Metallurgical Processes", *AIME lecture notes, p.13.*

[54] Gaspar.T,L.E.Hackman,Y.Sahai,W.A.T.Clark and J.V.Wood(1986), Proc:Conf.on Rapidly Solidified Alloys *1985 2-4 Dec, Vol.58, p.23-26.*

[55] *Gaspar T, Y.Sahai and L.E.Hackman(1986),* "Rapid Solidification of Titanium alloys" *in Titanium Rapid Solidification Technology Ed.F.H Froes D.Eylon. Pub. A.I.M.E, p.89-96.*

[56] *Gillen A.G and B.Cantor(1985),* Acta Metall, *Vol.33. No:10, pp:1813-1825.*

[57] *Greenwood A and J.B.P Williamson(1966),* Proc Roy Soc .*London A., p.295,300.*

[58] *Gungi K, K.Kusaka, E.Ishikawa and K.Sudo(1974),* "Solidification structure of high speed tool steel",Tetsu-to-Hagane, *Vol.59.p.1089, Trans.1515, Vol.14,1974, p.257-266.*

[59] *Gutierrez E.M and J.Szekely(1986),*Metal.Trans B. *Vol.17B, p.695-703.*

[60] *Gutierrez E.M and E.Miravate(1988)* "A mathematical model of the stip casting process", in Casting of Near Net Shape Products. *The Met Soc.1988. Ed. Y.Sahai, J.E.Battles, R.S Carbonara, C.E.Mobley.*

[61] *Gutierrez E.M and E Miravate.*NASA Contractor Report *179551. pp.59-103.*

[62] *Hackman L.D and T. Gaspar(1986),* Industrial Heating, *L III(I), p.36-38.*

[63] *Halden F.A and W.D.Kingery(1955),* J.Phys.Chem, *Vol.59, p.557.*

[64] *Hansen M and K.Anderko(1958),* The constitution of Binary Alloys *Mc Graw-Hill, New York.*

[65] *Hansen(1965),* Progress in Surface and Membrane Science, *Academic Press, New York.*

[66] *Hayzelden C(1984) .Phil Thesis, Sussex University.*

[67] *Hayzelden C, J.J Rayment and B.Cantor(1983),* Acta Metall. *Vol.31.*

[68] Heiple C.R and J.R.Roper(1981), Rockwell International Report *RFP-3174 Rockwell International Energy Systems Group Golden, Colorado, U.S.A.*

[69] Heiple C.R and J.R.Roper(1982), Welding Journal, *"Mechanism for minor element effect on G.T.A fusion zone geometry"., 61(5).p.97, 102.*

[70] Higgins B.G and L.E Scriven(1980), Chem.Eng.Sci, *Vol.35, pp.673-682.*

[71] Hillman H and H.R.Hilzinger(1978), Rapidly Quenched Metals, *Vol.1, p.22.*

[72] Hiro T et al(1970), JISI Japan, *Vol.56., pp.1182.*

[73] Hirsch P.B, A Howie, R.B.Nicholson(1965),"Electron Microscopy of Thin Crystals", *p.268. Ed. P.B.Hirsch, A.Howie, R.B.Nicholson, D.W.Pashley., Butterworth. William Cloves and sons Ltd.*

*[74] Hondros E.D(1965),*Proc.Roy.Soc.,Ser.A, *Vol.286, p.479.*

[75] Hubert Jean Claude, Francois Mollard and Benno Lux(1973), Z,Metallk. *Vol.64, p.835.*

[76] Hull R.J(1989), Trans.ASME, *Vol.111.,May, pp.352-356.*

[77] Hull D(1975), Introduction to Dislocations. *Pergamon Press. p.105.*

[78] Hunt J.D(1979), Solidification and Casting of Metals, The Metals Society Book 192. *London. p.3.*

[79] Ibaraki M, T.Okamoto and H.Matsumoto(1968),"The structure of unidirectionally frozen metastable iron-carbon alloys"., *J.Japan.Inst of metals. Vol.32, pp396-402.*

[80] Inman M.C and H.R.Tipler(1963), Met.Rev., *Vol.8, p.105.*

[81] Itiro T et al(1970), JISI Japan. *Vol.56, pp.1182.*

[82] Jacobian H and K.Schwerdtfeger(1976), "Dendrite morphology of steady state unidirectionally solidified steel", *Met.Trans., Vol.7A., p.811-820.*

[83] Jerkontoret(1977), "A guide to the Solidification of Steels"

[84] Johnson E, L.Graaback, J.V.Wood, A.Johansen and L.Sarhalt Kristensen(To be published in J.Mat Sci.Eng)

[85] Jones H(1978), "Rapid Solidification Processing", *R.Mehrabian, B.Kear, M.Cohen, eds.Claitor's Publihing Div. Baton Rouge, La. P.28*

[86] Katgerman L(1980) Scripta Metall, *Vol.14, p.861.*

[87] Katgerman L(1983), "Modelling of Casting and Welding Process II", *The Metallurgical Society of AIME. p.139.*

[88] Katgerman L and P.J Van den Brink(1982), Rapidly Quenched Metals IV, *Japan Inst. Metals, Sendai. Vol.1, p.61.*

[89] Kato S and H.Yoshida(1971), Tetsu-Ta-Hagane. *Vol.57, p.1976-1984.*

[90] Kasama A, et al(1986), "A consideration of the rapid solidification of steels by twin-roll caster", *Trans.Iron.Steel.Inst.Japan. Vol.26(4)B, pp.139-140.*

[91] Kasama A, S.Mizoguchi, K.Miyazawa, M.Hozn and T.Sugai(1987). Near net shape casting, A publication of the iron and steel society, "A consideration on the rapid solidification of steels- Solidification of steel by twin-roll caster", *p.59-63.*

[92] Kattamis T.Z and M.C Flemings(1965), Transactions of the Metallurgical Society of AIME. *Vol.233, p.992.*

[93] Kattamis T.Z and M.C Flemings(1966), Transaction of the Metallurgical Society of AIME, *Vol.236, pp.1523-1532.*

[94] Kattamis T.Z and M.C Flemings(1970), Transaction of the Metallurgical Society of AIME., *Vol.1, pp.1449-1451.*

[95] *Kaufman S.M(1967)*, Acta metal, *Vol.15., p.1089.*

[96] *Kavesh S(1976)*, Metallic Glasses. *American society of Metals, p.36.*

[97] *Kavesh S(1976)*, "Rapid Solidification Technology Source Book", *ASM.,p.81. Ed.R.L.Ashbrook, ASM, Metals Park Ohio.*

[98] *Keene B.J(1983)*, "A Survey of Extant Data for the Surface Tension of Iron and its Binary Alloys". *NPL report DMA(A)67. p1.*

[99] *Keene B.J, K.C.Mills, J.W.Bryant and E.D Hondras (1982)*, Can.Metall. Quart. *Vol.21, p.393-403.*

[100] *Keller J.R and T.L.Bergman(1989)*, Trans. of the ASME. *Vol.111, Aug. p.690.*

[101] *Korber and Oelsen(1957)*, Metallurgie du fer, Dunod, Colombier.

[102] *Kozakevitch P and G.Urbain(1961)*, Mem.Sci.Rev.Met, *Vol.58(6), p.401, Vol.58(7), p.518., Vol.58(12), p.931.*

[103] *Kozakevitch P, S.Chatel, G.Urbai and M.Sage(1955)* , Rev. Met*(Paris) Vol.52, p.139.*

[104] *King D.La.W(1970)*, U.S Patent No: 3 522 036

[105] *Landau L.D(1959)*, Fluid Mechanics

[106] *Landau L.D and V.G Levich(1942)*, Acta Physicochimica *URSS 17, Ed. B.V Deryagin, Dokl.Akad.Nauk SSSR 39, 11(1943)*

[107] *Levich V.G(1962)*, "Physiochemical Hydrodynamics", *Ch1, Prentice Hall inc. Englewood Cliffs. W55-3092 p.378-681.*

[108] *Li J.C.M(1961)*, J.Appl. Phys, *Vol.32, p.525.*

[109] *Li J.C.M and Y.T.Chov(1970)*, Met.Trans., *Vol.1, p.1145.*

[110] *Liebermann H.H and Grahams(1976)* I.E.E.E, Trans on mag., *p.21*

[111] *Liebermann H.H(1980)*, Mater Sci.Eng, *Vol.43, pp.203-210.*

[112] Liebermann H.H and C.D.Graham(1976), Jr.IEEE Trans. Mag*12, No:6,921.*

*[113] Liebermann H.H and G.D.Graham(1976),*Jr., Joint Magnetism and Magnetic Materials, Intermag Conference AIP/IEEE, *Pittsburg (unpublished).*

[114] Love D.B and J.D.Nauman(1988), in "Casting of Near Net Shape Products", *ed.Y.Sahai, J.E.Battles, R.S.Carbonara and C.E Mobley, pp.597.*

*[115] Lu w.K and A.E.Hamielec(1975),*Can.Met.Quart. *Vol.14.p.111*

[116] Mac Isaac D.G, Y.Shiohara, M.GChu and M.C Flemings(1983), in "Proc.Conf. on Grain Refinement in Castings and Welds", *Metallurgical Society of AIME, Warrandale, PA. Ed,G.I Abbaschian and S.A David.*

[117] Marcinkowski M.J(1970), "Conference of Fundamentals Aspects of Dislocation Theory", *Gaithersburg, Maryland, April 21-25(1969), NBS Special Publication. No:317 (Washington D.C).*

[118] Marcinkowski M.J(1971), "Electron Microscopy and Structure of Materials". *University Of California Press. Berkeley, Los Angles. London pp.394-396.*

[119] Maringer R.E(1988), Mat.Science and Eng. *Vol.98, p13.*

[120] Mascanzoni A and G.Bazzichelli(1970), Phil Mag *Vol.22, p.857.*

[121] Massoubre J.M and B.F Pflieger(1978), AlChE Symposium Series. The American Institute of Chemical Engineers. *No.180, Vol.74, p.48-57.*

[122] Masounave J, J.Blain and E.Essadiqi(1988) "La coulee directe de me'taux" Se'minaire sur les nouvelles applications de l'acier face a concurrence des materiaux de substitution, commission Economique pour l'Europe, Luxembourg, 2 au 6 mai.

[123] "Metals Handbook", *8 th ed (1961) Vol.1, ASM, Metals Park Ohio.*

[124] Mc lean D(1957), Grain Boundaries in Metals, *Oxford V.P.London. Chs,3,4,5.*

[125] Miles J.W(1962), J.Fluid Mech., *Vol.13, pp.433-448.*

[126] Miyazawa K and J Szekely(1981), "A Mathematical model of the splat cool-
ing process using the twin-roll technique"., Metal.Trans.A. *Vol.12A, p.349-358.*

[127] Miyazawa K and J.Szekely(1981) Met.Trans.A., *Vol.12 A, p.1047.*

*[128] Monma K(1960)*Nippon Kinzoku Gakkaishi, *Vol.24, p.374,377.*

[129] Morita Z and T.Iida(1981), First Sino-Japanese symposium Iron and steel making. *p.125.*

[130] Murr L.E , G.I.Wong and R.J.Horylev(1973), Acta Met., *Vol.21, p.595.*

[131] Murr L.E, R.J Horylev and W.N Lin(1970), Phil.Mag, Vol.22, p.515.

[132] Murr L.E(1974), Appl.Phys.Lett. *Vol.24, p.533.*

[133] Murr L.E(1975), Met. Trans., *Vol.6A, p.505.*

[134] Murr L.E(1975), "Interfacial Phenomena in Metals and Alloys", *p.126. Ed.L.E Murr. Addison-Wesley Publishing Comp.*

[135] Murr L.E, G.I.Wong and R.J.Harylev(1973), Acta Met., *Vol.21, p.595.*

[136] Narasimhan M.C(1979), U.S Patent No: *4.142 571.*

[137] Nauman J.D and D.B Love(1987), "Controlling the shape of cast stainless steel strip" *in Int.Sym. on Near-Net Shape Casting of Strip*

[138] Nayfeh and Saric(1971), J.Fluid Mech., *Vol.46, pp.209-231.*

[139] Nicholas M.E, P.A.Joyer, B.M.Tessem and M.D.Olsen (1961), J.Phys.Chem, *Vol.65, p.1373.*

[140] Nogi K, K.Ogino, A.Mc Lean and W.A.Miller(1986), Met.Trans B. *Vol.17B, p.163.*

[141] Ohno R(1972), Liquid Metals Chemistry and Physics, *Ch.2, p.72. Ed.Sylvan. Z.Beer, Publ.Marcel Dekker.inc. New york.*

[142] Oriani R.A(1950), J.Chem Phys., *Vol.18, p.575.*

[143] Patankar S.V(1980), Numerical Heat Transfer and Fluid Flow, *Hemisphere Publishing Co. Washington D.C.*

[144] Perry R.H and C.H.Chilton(1973), Chemical Engineer's Handbook 5th Ed, *McGraw-Hill, New York, NY, pp10-11.*

[145] Plateau M(1873), Statique des Liquides *(University of Paris).*

[146] Polich R.F and M.C Flemings(1965), "Mechanical Properties of Unidirectional Steel Castings ",Trans. American Foundryman's Soc, *Vol.73, p.28-33.*

*[147] Ruhl R.C(1967),*Mat.Science Engineering, *Vol.1. p.313-320.*

[148] Ruschak K.J(1976), Chem.Eng.Sci *Vol.31, pp.1057-1060.*

[149] Rouse H(1946), Elementary Mechanics of Fluids, *(Wiley, New York).*

[150] Schlichting H(1968), Boundary Layer Theory, *Mc Graw Hill, New York. Ed. H. Schlichting.*

[151] Schwabe D, R.Lamprecht and A.Scharmann(1989), Physicochemical Hydrodynamics *p.291.Ed. R.F..Probstein, Publ. Butterworths.*

[152] Schwabe D, A.Scharmann, F.Prisser and R.Oeder (1978), J.Crystal Growth *Vol.43, p.305-312.*

*[153] Schlichting H(1979),*Boundary Layer Theory, *7 th edition(Mc Graw-Hill), p.116-122. Ed. H.Schlichting.*

[154] Skapski A.S(1956), Acta Met., *Vol.4, p.576.*

[155] Sugiyama M, T.Umeda and J.Matsuyama(1974), "On Microsegregation and microstructure in 18 Cr-8 Ni and 25 Cr-10Ni Austenitic stainless steels" Tetsu-to-Hagone., *Vol.60, pp.1094-1113.*

[156] Sun R.C(1970), AFS Cast Met.Res J. *Vol.6, p.105.*

[157] Suzuki A, T.Suzuki, Y.Nagaoka and Y.Iwata (1968),"On secondary dendrite arm spacing in commercial carbon steels with different carbon content; J.Japan inst of metals. *Vol.32, p.1301-1305.*

[158] Suzuki A and Y.Nagoka(1969), "Dendrite morphology and arm spacing of steels", J.Japan inst of met., *Vol.33, p.658-663.*

[159] Smugeresky J.E(1982), Met.Trans.*A p.1534 "Characterization of rapidly solidified iron based superalloys".*

[160] Taha M.A,M and K.Schwerdtfeger(1982), Met.Trans *"Dendrite morphology of several steady state unidirectionally solidified iron-based alloys", Vol.13A, p.2131-2141.*

[161] Taha M.A(1986),"Influence of solidification parameters on dendrite arm spacings in low carbon steels".Journal of Materials Science Letters. *Vol.5, pp.307-310.*

[162] Takeshita K and P.H.Shingu(1986), Trans.Jpn.Inst.Met. *Vol.27, No:6, pp.454.*

*[163] Tallmadge J.A and C.Gutfinger(1967),*Ind.Eng.Chem *Vol.59.pp.18-34.*

[164] Taylor C.R and J.Chipman(1943), AIME, Vol.154, p.228.

[165] Thomas B.G, I.V.Samarasekera and J.K Brimacombe(1987), Met.Trans B, *Vol.18B, p.119.*

[166] Timsit R.S(1982) Appl.Phys.Lett. *Vol.40, p.379.*

[167] Tozawa H, S.Moriwaki, N.Yasukawa, T.Fujii, T.koshikawa and T.Kimura(1990), "Development of Thin Slab Caster", *Kawasaki Steel Technical Report No.22.*

[168] Tszin-tan V, R.A.Karasev and A.M.Samarin(1960), Russ.Met and Fuels *(English Transl).Vol.1, p.21, Vol.2, p.49.*

[169] Turkdogan C(1980), Phy.Chem.of High Temperature Technology, *Academic Press, New York.*

[170] Velarde M.G and C.Normand(1980), Scient *.Am. July 79*

*[171] Vincent J.H, J.G.Herbertson and H.A Davies(1982),*Rapidly Quenched Metals IV. *Japan Inst Metals. Sendai, Vol.1, p.77.*

[172] Vishkarev.F and V.I.Yavoiskii(1962),Izv.Vysch.Uch,Zav.Chern. Met.Vol.5(3),p.60,Brutcher.Technical Translation No:5600.

*[173] Walen T.J,S.M Kaufman and M.Humenik(1962),*Trans.ASM, *Vol.55, p.778.*

[174] Warrington D.H,H.A Davies and N.Shahaji(1982), Rapidly Quenched Metals IV., *Japan Inst.Metals, Sendai., Vol.1.p.69.*

[175] Wasson R.A(1978), "Primary Dendrite Arm Spacing and the Cell-Dendrite Transition", *Ph.d Thesis, Department of Materials Science and Engineerings, Massachusetts Institute of Technology, Cambridge, Massachusetts. June 1978.*

*[176] Weast R.C(1977),*Handbook of Chemistry and Physics, *CRC Press, Cleveland.*

[177] Whelan M.J and P.B Hirsch(1957), Phil.Mag,*p.1303.*

[178] Wolf M(1986),"Strand Surface Quality of Austenitic Stainless Steels. Part2, Microscopic solidification structure,"Ironmaking Steel Making., *V.13, p.258-262.*

[179] Yavari A.R and P.Desre(1981), Scripta Metall, *Vol.15, p.503.*

[180] Yoshio Abe, Ken-Ichi Miyazawa and Masakazu Nakamura(1988), Materials Science and Engineering, *Vol.98, p.351-355.*

[181] Yu H(1987) Metal.Trans A. *Vol.18(A), p.557-563.*

[182] Zehr R, M.Mchen and J.Mazumder(1988), Modelling of casting and welding Process IV, *p.435.*

Appendix

.1 The theory of surface tension measurements by modified oscillation droplet technique

This technique based on the frequency measurements of the oscillations of molten droplet levitated by magnetic field. When the frequency of the oscillations assumed as an average frequency w it is possible to calculate the surface tension between liquid and vapour phases. The theory relating surface tension to the frequency of oscillation of a spherical droplet has been proposed by Rayleigh(1879). This theory provides the following equation.

$$\sigma_{LV} = \frac{3}{8}\pi m w_R^2 \qquad (.1)$$

where σ is the surface tension, m is the mass of the droplet and w_R is the Rayleigh frequency of oscillation for a perfect sphere. The assumptions involved in obtaining this equation are as follows;

1) The amplitude of deviation from the spherical mode is very small.

2) The liquid viscosity is low so that damping of the natural oscillations may be ignored.

3) The sphere consists of an incompressible fluid.

The influences, however, of a levitating magnetic field disturb both the sphericity and the oscillation frequency. A detailed mathematical description by Cummings and Blackburn(to be published) describing an aspherical droplet distorted by the supporting electro-magnetic field, has shown a splitting of the expected single frequency of the fundamental mode of oscillation w_R, into either three or five bands. A model proposed for the magnetic field by Cummings and Blackburn(1988) shows that the translational frequencies provide a useful measure of the gradient of the magnetic field strength. A correction factor of $2\overline{w_t^2}$ is obtained where $\overline{w_t^2}$ is the mean of the sum of squares of the transitional frequency in the x, y and z direction, so that the Rayleigh frequency is related to the five fundamental frequencies, w_i, by the equation:

$$w_R^2 = \frac{1}{5}\sum_{i=1}^{5}\left(w_i^2 - 2\overline{w_t^2}\right) \qquad (.2)$$

Generally, the five modes would have different frequencies, but in the case of cylindrical symmetry(with no rotation) only three bans are predicted. When this happens two pairs in the five bands have identical frequencies, that is, two bands are doubly degenerate and equation(.2) becomes:

$$w_R^2 = \frac{1}{5}\left(w_\Sigma^2 + 2w_\Pi + 2w_\Delta^2\right) - 2\overline{w_i^2} \qquad (.3)$$

The frequency spectra can also be denoted as follows, the peak at minimum frequency Σ, middle frequency Π and maximum frequency Δ. Cummings and Blackburn(1988) proposed that any of the three bands can in principle be the non-degenerate band. It is possible only to provide upper and lower limits for the surface energy, according to whether the non- degenerate band is either the highest, w_{max} or the lowest w_{min} of the three observed bands then w_R. The mathematical model for the frequency spectra consisted of five characteristic peaks (in Figure 6.4) can be written as

$$w_R^2 = \frac{1}{10}\left(3w_{max}^2 + 3w_{min}^2 + 4w_{middle}^2\right) - \frac{1}{3}\left(2w_{xy}^2 + w_z^2\right) \qquad (.4)$$

An amplitude spectrum for a molten 304 stainless steel ball at 1620°C is given in Figure 6.4. The Rayleigh frequency w_R of oscillating molten droplets at different temperatures were calculated by substituting the peak frequencies from the spectrum into equation(.4).

Exp No=21

Alloy composition(wt%):
Ni=10.3 Cr=17.8 Si=0.276 Mn=0.989 Al=0.003 Cu=0.144 P=0.052

O=0.0259 S=0.0272 N=0.0005 C=0.026 Bal Fe

Cr-equivalent =11.627 Ni-equivalent=18.432

Charge materials(g) :
304 stainless=2580 FeSi(Grade70%)=3.5

Al (100%)=- FeS(Grade25%)=1.3 FeMn(Grade86%)=-

Strip weight(g)=890

Slag composition(wt%):
SiO_2=75.0/Al_2 O_3=12.0/CaO=1.0/Na_2O=3.7/K_2O=2.5/TiO_2=0.3/Fe_2O_3=0.3

Casting temp(°C)=1700 Liquidus(°C)=1457 Solidus(°C)=1287

Surface tension(σ)at casting temp(Nm^{-1})=1.670

Temperature coefficient ($d\sigma/dT$)($N.m^{-1}K^{-1}$)=0.00064

Wheel speed ($m.s^{-1}$)=2.73

Stream velocity-V_{liq}($cm.s^{-1}$)=3.423 Flow rate-Q($cm^3.s^{-1}$)=14.251

Stream velocity-min V_j($cm.s^{-1}$)=2.096

ΔV(cm/s)=1.327 Rj(mm)=19.5 Lj(mm)=9.1

Marangoni number-Ma=127447 Capillary number Ca=0.00841

Thickness(mm)=0.209 Width (mm)=26

Liquid metal heigth(mm)	start=19.5	mid=19.5	end=18.2
Melt pool length(mm)	start=23.4	mid=24.1	end=19.5

Edge characteristics observed:
Wide uniform strip, narrow strip very small serrations at both side

Exp No=23

Alloy composition(wt%):
Ni=10.2 Cr=17.8 Si=0.279 Mn=0.847 Al=0.05 Cu=0.152 P=0.04

O=0.0166 S=0.0122 N=0.0001 C=0.027 Bal Fe

Cr-equivalent =11.48 Ni-equivalent=18.44

Charge materials(g) :
304 stainless=2527.38 FeSi(Grade70%)=1.5

Al = - FeS(Grade25%)=0.46 FeMn(Grade86%)=-

Strip weight(g)=712

Slag composition(wt%):
SiO_2=75.0/Al_2 O_3=12.0/CaO=1.0/Na_2O=3.7/K_2O=2.5/TiO_2=0.3/Fe_2O_3=0.3

Casting temp(°C)=1750 Liquidus(°C)=1458 Solidus(°C)=1293

Surface tension(σ)at casting temp(Nm^{-1})=2.09

Temperature coefficient ($d\sigma/dT$)($N.m^{-1}K^{-1}$)=0.001

Wheel speed ($m.s^{-1}$)=2.73

Stream velocity-V_{liq}($cm.s^{-1}$)=3.065 Flow rate-Q($cm^3.s^{-1}$)=16.783

Stream velocity-min V_j($cm.s^{-1}$)=3.057

ΔV(cm/s)=0.008 Rj(mm)=23.4 Lj(mm)=15.6

Marangoni number-Ma=239974 Capillary number Ca=0.0068

Thickness(mm)=0.220 Width (mm)=27.1

Liquid metal heigth (mm) start=22.1 mid=23.4 end=22.75

Melt pool length (mm) start=26 mid=27 end=26

Edge characteristics observed:
Uniform strip with some serrations at one side

Exp No=24

Alloy composition(wt%):

Ni=10.2 Cr=17.5 Si=0.293 Mn=0.793 Al=0.04 Cu=0.134 P=0.052

O=0.0571 S=0.0736 N=0.0015 C=0.0212 Bal Fe

Cr-equivalent =11.31 Ni-equivalent=18.16

Charge materials(g) :

304 stainless= 2594 FeSi(Grade70%)=3.6

Al =- FeS(Grade25%)=0.58 FeMn(Grade86%)=-

Strip weight(g)=860

Slag composition(wt%):

SiO_2=75.0/Al_2 O_3=12.0/CaO=1.0/Na_2O=3.7/K_2O=2.5/TiO_2=0.3/Fe_2O_3=0.3

Casting temp(°C)=1600 Liquidus(°C)=1458 Solidus(°C)=1282

Surface tension(σ)at casting temp(Nm^{-1})=1.43

Temperature coefficient ($d\sigma/dT$)($N.m^{-1}K^{-1}$)=0.00078

Wheel speed ($m.s^{-1}$)=2.73

Stream velocity-V_{liq}($cm.s^{-1}$)=3.85 Flow rate-Q($cm^3.s^{-1}$)=13.39

Stream velocity-min V_j($cm.s^{-1}$)=4.74

ΔV($cm.s^{-1}$)=-0.886 Rj(mm)=15 Lj(mm)=13.69

Marangoni number-Ma= Capillary number Ca=0.0091

Thickness(mm)=0.217 Width (mm)=27

Liquid metal heigth (mm)	start=17.5	mid=15	end=9.62
Melt pool length (mm)	start=23	mid=19	end=10.36

Edge characteristics observed: Oxidation on the surface, serrations at one side

Exp No=25

Alloy composition(wt%):
Ni=10.7 Cr=18.0 Si=0.35 Mn=1.38 Al=0.005 Cu=0.128 P=0.03

O=0.0334 S=0.0195 N=0.0007 C=0.031 Bal Fe

Cr-equivalent =12.376 Ni-equivalent=18.740

Charge materials(g) :
304 stainless= FeSi(Grade70%)=4

Al = - FeS(Grade25%)=1 FeMn(Grade86%)= -

Strip weight(g)=1083

Slag composition(wt%):
SiO_2=75.0/Al_2 O_3=12.0/CaO=1.0/Na_2O=3.7/K_2O=2.5/TiO_2=0.3/Fe_2O_3=0.3

Casting temp(°C)=1630 Liquidus(°C)=1453 Solidus(°C)=1285

Surface tension(σ)at casting temp(Nm^{-1})=1.970

Temperature coefficient ($d\sigma/dT$)($N.m^{-1}K^{-1}$)=0.00148

Wheel speed ($m.s^{-1}$)=2.73

Stream velocity-V_{liq}($cm.s^{-1}$)=5.038 Flow rate-Q($cm^3.s^{-1}$)=12.16

Stream velocity-min V_j($cm.s^{-1}$)=5.098

ΔV($cm.s^{-1}$)= -0.06 Rj(mm)=12.25 Lj(mm)=10.25

Marangoni number-Ma=194556 Capillary number Ca=0.0079

Thickness(mm)=0.166 Width (mm)=23

Liquid metal heigth(mm) start=10.5 mid=12.25 end=11.90

Melt pool length(mm) start=17.10 mid=17.15 end=15.75

Edge characteristics observed:
Some voids and edge serrations, generally uniform width

Exp No=27

Alloy composition(wt%):
Ni=10.2 Cr=17.6 Si=0.313 Mn=0.939 Al=0.01 Cu=0.116 P=0.054

O=0.0176 S=0.018 N=0.0003 C=0.026 Bal Fe

Cr-equivalent =11.465 Ni-equivalent=18.342

Charge materials(g) :
304 stainless=2516.6 FeSi(Grade70%)= -

Al =- FeS(Grade25%)=0.53 FeMn(Grade86%)=-

Strip weight(g)=1146

Slag composition(wt%):
SiO_2=75.0/Al_2 O_3=12.0/CaO=1.0/Na_2O=3.7/K_2O=2.5/TiO_2=0.3/Fe_2O_3=0.3

Casting temp(°C)=1690 Liquidus(°C)=1458 Solidus(°C)=1289

Surface tension(σ)at casting temp(Nm^{-1})=1.98

Temperature coefficient ($d\sigma/dT$)($N.m^{-1}K^{-1}$)=0.00136

Wheel speed ($m.s^{-1}$)=2.73

Stream velocity-V_{liq}($cm.s^{-1}$)=4.460 Flow rate-Q($cm^3.s^{-1}$)=5.297

Stream velocity-min V_j($cm.s^{-1}$)=5.114

ΔV($cm.s^{-1}$)=-0.684 Rj(mm)=12.34 Lj(mm)=10.33

Marangoni number-Ma=247096 Capillary number Ca=0.0074

Thickness(mm)=0.177 Width (mm)=11.72

Liquid metal heigth (mm) start=16.69 mid=12.34 end=9.07

Melt pool length (mm) start=25.05 mid=17.42 end=12.34

Edge characteristics observed:
High serration notch hight

Exp No=29

Alloy composition(wt%):
Ni=9.52 Cr=17.8 Si=0.279 Mn=1.40 Al=0.0017 Cu=0.1 P=0.048

O=0.0158 S=0.015 N=0.0004 C=0.0312 Bal Fe

Cr-equivalent =11.196 Ni-equivalent=18.395

Charge materials(g) :
304 stainless=2624.12 FeSi(Grade70%)=-

Al =- FeS(Grade25%)=2.057 FeMn(Grade86%)=43.23

Strip weight(g)=463

Slag composition(wt%):
SiO_2=75.0/Al_2 O_3=12.0/CaO=1.0/Na_2O=3.7/K_2O=2.5/TiO_2=0.3/Fe_2O_3=0.3

Casting temp(°C)=1740 Liquidus(°C)=1457.88 Solidus(°C)=1289.518

Surface tension(σ)at casting temp(Nm^{-1})=2.05

Temperature coefficient ($d\sigma/dT$) ($N.m^{-1}K^{-1}$)=0.00097

Wheel speed ($m.s^{-1}$)=2.739

Stream velocity-V_{liq}($cm.s^{-1}$)=4.595 Flow rate-Q($cm^3.s^{-1}$)=9.896

Stream velocity-min V_j($cm.s^{-1}$)= 2.605

ΔV($cm.s^{-1}$)=1.99 Rj(mm)=13.43 Lj(mm)=5.81

Marangoni number-Ma=215182 Capillary number-Ca=0.0072

Thickness(mm)=0.222 Width (mm)=19.53

Liquid metal heigth (mm) start=13.06 mid=13.43 end=11.97

Melt pool length (mm) start=15.97 mid=13.78 end=13.90

Edge characteristics observed:
uniform width, low serration notch height

Exp No=30

Alloy composition(wt%):
Ni=9.14 Cr=18.2 Si=0.355 Mn=1.61 Al=0.02 Cu=0.09 P=0.048

O=0.0092 S=0.0232 N=0.0005 C=0.0338 Bal Fe

Cr-equivalent =10.999 Ni-equivalent=19.020

Charge materials(g) :
304 stainless=2509.83 FeSi(Grade70%)=-

Al = - FeS(Grade25%)=1.55 FeMn(Grade86%)=37.33

Strip weight(g)=363

Slag composition(wt%):
SiO_2=75.0/Al_2 O_3=12.0/CaO=1.0/Na_2O=3.7/K_2O=2.5/TiO_2=0.3/Fe_2O_3=0.3

Casting temp(°C)=1580 Liquidus(°C)=1456.58 Solidus(°C)=1286.20

Surface tension(σ)at casting temp(Nm^{-1})=1.987

Temperature coefficient ($d\sigma/dT$) ($N.m^{-1}K^{-1}$)=0.00153

Wheel speed ($m.s^{-1}$)=2.73

Stream velocity-V_{liq}($cm.s^{-1}$)= 3.599 Flow rate-Q($cm^3.s^{-1}$)=21.885

Stream velocity-min V_j($cm.s^{-1}$)=3.090

ΔV($cm.s^{-1}$)=0.509 Rj(mm)=21.78 Lj(mm)=14.52

Marangoni number-Ma=142540 Capillary number Ca=0.0077

Thickness(mm)=0.244/0.185 Width (mm)=34/10

Liquid metal heigth (mm) start=9.075 mid=10.16 end=21.78

Melt pool length (mm) start=11.253 mid=10.16 end=30.85

Edge characteristics observed:
widest and best strip very small serration notch

Densitometer results of melt poolsl(red light wavelength range(620-700 nm))

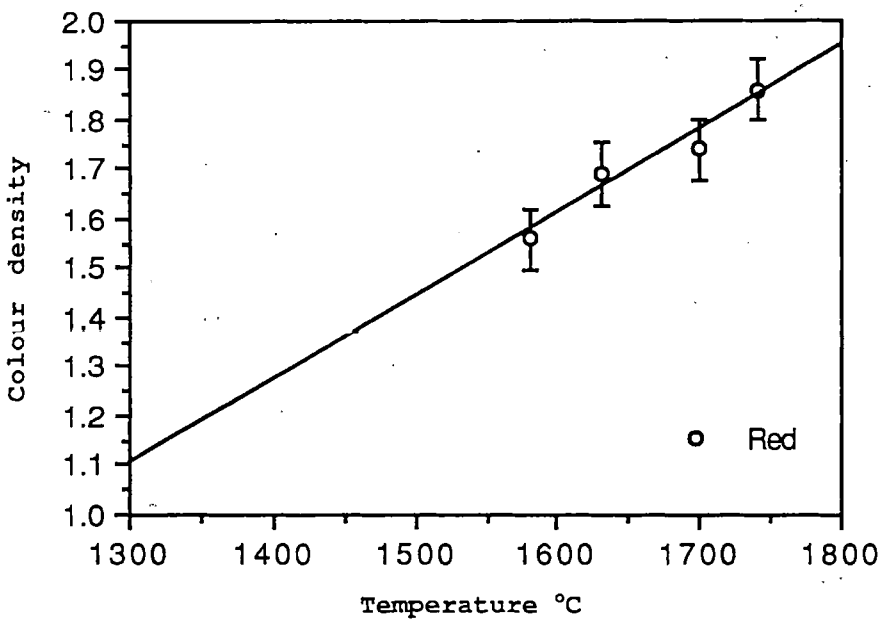

Exp no	Vc cm/sec	Vj cm/sec	Q cc/sec	μ N.sec/m^2	Ca	Ma
21	3.423	2.096	14.251	0.0052	0.0084	127447
23	3.065	3.057	16.783	0.0051	0.0068	239974
24	3.852	4.738	13.389	0.0048	0.0091	97877
25	5.038	5.098	12.161	0.0057	0.0079	194556
27	4.460	5.144	5.297	0.0054	0.0074	247096
28	4.121	2.044	9.860	0.0066	0.0097	57844
29	4.595	2.605	9.896	0.0054	0.0072	215182
30	3.599	3.090	21.885	0.0056	0.0077	142540